Technische Universität München
TUM School of Engineering and Design

Orbit determination for independent LEO mega-constellations

Xingchi He

Vollständiger Abdruck der von der TUM School of Engineering and Design der Technischen Universität München zur Erlangung eines

Doktors der Ingenieurwissenschaften (Dr.-Ing.)

genehmigten Dissertation.

Vorsitz: Prof. Dr.-Ing. Liqiu Meng

Prüfer*innen der Dissertation:

1. Prof. Dr. phil. nat. Urs Hugentobler
2. Hon.-Prof. Maorong Ge

Die Dissertation wurde am 25.09.2023 bei der Technischen Universität München eingereicht und durch die TUM School of Engineering and Design am 06.02.2024 angenommen.

Acknowledgments

Time is a magical thing. Sometimes we complain about it moving too slowly, and other times, without realizing it, years have passed. I have been studying at TUM for many years now, and during this time, the world has undergone significant changes. Unexpected events have unfolded, including wars, pandemics, and explosive advancements in the field of AI and other technologies. Throughout my doctoral studies, I have experienced moments of exploration, hesitation, and setbacks, leading me to the present state of clarity. In this journey, many people have extended their help to me, and I would like to express my gratitude to them.

First and foremost, I would like to express my heartfelt gratitude to my supervisor, Professor Urs Hugentobler, whose guidance has been invaluable throughout my doctoral journey. Prof. Hugentobler has always been patient and kind, granting me ample research freedom. I deeply admire his profound knowledge, attention to detail, and unique insights. Every discussion and presentation with him has been immensely beneficial. Whenever I faced confusion, Prof. Hugentobler made time to discuss and clarify my doubts. His dedication to research and positive mindset serve as an exemplary model for lifelong learning.

Additionally, I would like to express my gratitude to my mentor, Dr. Anja Schlicht. Whenever I encountered research bottlenecks or found myself in a stalemate, Dr. Schlicht promptly identified the issues and offered assistance. Through our communication, I was able to clarify my thoughts and overcome the obstacles. Her guidance and advice in my research have been immensely helpful. Her cheerful smile always managed to uplift my spirits and instill a positive mindset within me.

Furthermore, I would like to extend my gratitude to Dr. Bingbing Duan. As a senior colleague and fellow Chinese, he has not only provided me with patient guidance and assistance in academics but has also become a reliable friend in my life. He has shown genuine interest in my research progress and generously offered his help whenever I encountered difficulties. As someone who has already obtained a doctoral degree, he has provided me with valuable advice during times of setbacks. I wish him and his newborn son a healthy and prosperous future.

I would like to extend special thanks to the Federal Ministry for Economic Affairs and Climate Action for its support in partially funding my doctoral studies through the ADAM & EVA 2 project (project number 50NA1706). I would also like to express my gratitude to the colleagues from TUM Physics Department and OHB Company for their collaboration on this project. It has been an honor to be part of such an exciting and innovative endeavor.

I would also like to express my gratitude to my colleagues at FESG and IAPG. Their kindness has provided me with a comfortable and supportive research and office environment. Whenever I sought their help, they always offered their support. I am grateful to my Chinese colleagues and friends in Munich as well. Despite having adapted to life in a foreign land over the years, your presence undeniably adds joy and warmth to my life. There are numerous individuals whom I would like to thank for their contributions to both my research and personal

life throughout these years. Unfortunately, it is not possible to name them all here, but I want to express my heartfelt appreciation to each and every one of them.

I would like to express my gratitude to my parents, relatives, and friends back in China. The sudden outbreak of the pandemic has undoubtedly disrupted our already limited physical contact. Fortunately, modern technology has bridged the distance, making communication more accessible. Your comfort, encouragement, and assistance have provided me with immense support. I look forward to the day when we can reunite and spend time together.

At the end, I would like to express special gratitude to Dr. Yufeng Nie. His presence has undoubtedly been the highlight of these past few years, and I can't imagine how different my life would be without him. In terms of research, his arrival in Munich coincided with the most challenging period I faced in my research journey. Dr. Nie recognized my situation and voluntarily offered his assistance. With patience and meticulousness, he filled in many fundamental yet crucial gaps in my knowledge and provided crucial help in paving the way for my research. In terms of personal life, he is a cheerful and witty individual. I am delighted to have been roommates with him during his two years in Munich, which happened to be the period of the strictest lockdown due to the pandemic. Through spending 24 hours a day together, our bond naturally grew stronger. I feel fortunate to have him by my side and I hope this luck will continue to accompany me.

Abstract

In recent years, with the development of the internet and the emergence of new space companies such as SpaceX and OneWeb, low Earth orbit (LEO) satellites have experienced explosive growth. Thousands of LEO satellites are already in orbit, providing people with communication and internet services. Scientists have begun to explore how to apply these new LEO satellites to other areas of research and applications. LEO-PNT (Positioning, Navigation and Timing) is currently one of the most popular topics. Orbit determination is the basis of these applications. On the one hand, most of the current LEO satellites rely on satellite-borne Global Navigation Satellite System (GNSS) receivers for orbit determination. On the other hand, research on LEO satellite positioning mainly focuses on the field of LEO satellite-assisted GNSS positioning. With the establishment of mega-constellations composed of thousands of LEO satellites, there is little research on how to use these large numbers of satellites for independent orbit determination. This work focuses on this field. Starting from the basic constellation design, this study progressively examines various factors influencing orbit determination results, evaluates the accuracy of orbit determination for an independent LEO satellite constellation in a real-world environment, and contrasts it with the conventional GNSS-assisted orbit determination.

In order for the LEO satellite constellation to function as both a communication service and a GNSS, it must be designed accordingly. This work selects the Walker Delta type for constellation design. A multi-layer constellation is proposed in order to achieve a more uniform distribution of the visibility around the world. The enumeration search algorithm is utilized to select constellation parameters. Performance is evaluated by measuring the influence of several factors such as the number of visible satellites, dilution of precision (DOP) and cost. Based on these evaluations, it is concluded that a two-layer constellation with an orbital height of 900 km using Walker Delta 73°: 189/9/1 and an orbital height of 700 km using Walker Delta 38°: 189/7/1 would be suitable for further study. This constellation ensures a minimum of 6 visible satellites worldwide, with a position DOP (PDOP) below 3 in non-polar regions.

Based on this constellation, this study investigates various factors that can affect the accuracy of satellite orbits. The author has developed dedicated software for this work, implementing core functions based on an open-source library. Several experiments are conducted to test and discuss these factors, including the size and distribution of the ground station network, different types of inter-satellite link (ISL) links (intra- and inter-orbital links, inter-layer ISL), different weighting algorithms, and empirical parameters.

For geopolitical and geographical reasons, ground station networks may not be well distributed. This work examines the impact of different ground networks (global networks with different numbers of stations and regional networks in different areas and latitudes) on the determination of LEO satellite orbits with/without ISLs. The results show that high latitude networks have poorer geometry than middle/low latitude networks, even when more satellite observations are available. This leads to a worse determined orbit for high latitude networks. Adding more stations to a 16-station regional network has little improvement on orbit accuracy.

However, using ISL observations can significantly improve orbit accuracy, particularly when a small regional network is employed. Furthermore, accurate calibration of satellite biases is not necessary since it can be very well estimated and have almost no impact on satellite orbits.

A further study of the impact of different ISL types on the orbit determination of the LEO satellite constellation shows that when the number of links is limited, the inter-orbital links are more favorable than the intra-orbital links for orbit determination. Inter-layer inter-satellite links (ILISL) play a crucial role for the multi-layer constellation. This work studies 3 classical ILISL topologies and 2 variants for orbit determination. While the "connect till break" strategy provides consistent orbit errors regardless of changes in the weight factor, the "instant break" strategy is more advantageous as it results in smaller orbit errors across all scenarios.

Data weighting is critical for accurate orbit determination when multiple measurement types are involved. Incorrect weighting can degrade the orbit accuracy. This work proposes a simplified variance component estimation (VCE) algorithm to reduce the computation time for the constellation with many satellites. This simplified algorithm can be 124 times faster than the rigorous algorithm for a case with only 30 satellites, while maintaining the same accuracy of determined orbits. This ratio increases as the function of the third power of the number of satellites.

Empirical accelerations are often used to improve orbit modeling and increase orbit accuracy. This work discusses about the influence of different empirical parameter settings and constraints on the orbit determination of a LEO satellite constellation. The results show that different directions perform better with different estimation intervals. Too long intervals are not ideal for orbit determination. Very short intervals with absolute constraints can achieve optimal orbit accuracy. However, overly tight constraints can result in larger orbit errors.

An analysis examines how the formal error changes with different measurement type combinations and noise level ratios. GNSS can provide much more data, resulting in better orbit determination compared to ground station-only cases. However, when the noise level ratio of ground/GNSS measurements to ISL measurements exceeds 2.5:1, which is true for most cases, combining ground and ISL measurements can result in smaller formal errors with fewer observations compared to the GNSS-only case. By incorporating ISL measurements, the growth of formal errors due to higher noise levels of ground/GNSS can be prevented.

This study confirms the effectiveness of an independent LEO mega-system through a highly realistic simulation. By utilizing ground range observations from just six global stations and ISL observations, the proposed system can determine the orbit of a LEO satellite constellation with an error margin of only a few centimeters. Additionally, when compared to results obtained from a GNSS-assisted system, the independent LEO satellite system proves to be superior in terms of orbit determination accuracy - improving it by 59% over GNSS-only observations.

Keywords: low Earth orbit satellite; orbit determination; inter-satellite link; ground station network; variance component estimation; empirical acceleration; GNSS-assisted system

Zusammenfassung

In den letzten Jahren hat sich mit der Entwicklung des Internets und dem Aufkommen neuer Raumfahrtunternehmen wie SpaceX und OneWeb der niedrige Erdorbit (LEO) Satellitenmarkt explosionsartig entwickelt. Tausende von LEO-Satelliten sind bereits im Orbit und bieten den Menschen Kommunikations- und Internetdienste. Wissenschaftler haben begonnen, zu erforschen, wie man diese neuen LEO-Satelliten auch in anderen Bereichen nutzen kann. Die Positionierung, Navigation und Zeitbestimmung (PNT) im LEO ist derzeit eines der beliebtesten Themen. Die Bahnberechnung bildet die Grundlage für diese Anwendungen. Einerseits verlassen sich die meisten aktuellen LEO-Satelliten auf GNSS-Empfänger an Bord der Satelliten zur Bahnberechnung. Andererseits konzentriert sich die Forschung zur Positionierung von LEO-Satelliten hauptsächlich auf das Gebiet der GNSS-unterstützten Positionierung von LEO-Satelliten. Mit dem Aufbau von Mega-Konstellationen aus Tausenden von LEO-Satelliten gibt es jedoch nur wenig Forschung darüber, wie man diese große Anzahl an Satelliten für unabhängige Bahnberechnungen nutzen kann. Diese Arbeit konzentriert sich genau auf dieses Gebiet. Ausgehend vom grundlegenden Konstruktionsdesign einer solchen Konstellation werden in dieser Studie schrittweise verschiedene Faktoren untersucht, die Einfluss auf die Ergebnisse der Bahnberechnung haben können. Dabei wird die Genauigkeit einer unabhängigen Bahnberechnung für eine reale Umgebung bewertet und mit der konventionellen GNSS-unterstützten Bahnberechnung verglichen.

Um sicherzustellen, dass die LEO-Satellitenkonstellation sowohl als Kommunikationsdienst als auch als GNSS funktioniert, muss sie entsprechend konzipiert werden. Diese Arbeit wählt den Walker-Delta-Typ für das Konstellationsdesign aus. Es wird eine mehrschichtige Konstellation vorgeschlagen, um eine gleichmäßigere Verteilung der Sichtbarkeit weltweit zu erreichen. Der Enumerations-Suchalgorithmus wird verwendet, um Konstellationsparameter auszuwählen. Die Leistung wird durch Messung des Einflusses mehrerer Faktoren wie der Anzahl sichtbarer Satelliten, der Dilution of Precision (DOP) und der Kosten bewertet. Basierend auf diesen Bewertungen wird festgestellt, dass eine zweischichtige Konstellation mit einer Umlaufbahn von 900 km unter Verwendung von Walker Delta 73°: 189/9/1 und einer Umlaufbahn von 700 km unter Verwendung von Walker Delta 38°: 189/7/1 für weitere Untersuchungen geeignet wäre. Diese Konstellation gewährleistet weltweit mindestens 6 sichtbare Satelliten mit einem Position DOP (PDOP) unterhalb von 3 in nicht-polaren Regionen.

Basierend auf dieser Konstellation untersucht diese Studie verschiedene Faktoren, die die Genauigkeit von Satellitenbahnen beeinflussen können. Der Autor hat spezielle Software für diese Arbeit entwickelt, die Kernfunktionen auf Basis einer Open-Source-Bibliothek implementiert. Es werden mehrere Experimente durchgeführt, um diese Faktoren zu testen und zu diskutieren, darunter die Größe und Verteilung des Bodenstationsnetzwerks, verschiedene Arten von Inter-Satelliten-Verbindungen (ISL) (innerorbitale und interorbitale Verbindungen, interlayer ISL), unterschiedliche Gewichtungsalgorithmen und empirische Parameter.

Aus geopolitischen und geografischen Gründen sind Bodenstationennetzwerke möglicherweise nicht gut verteilt. Diese Arbeit untersucht die Auswirkungen verschiedener Bodennetzwerke (globale Netzwerke mit unterschiedlicher Anzahl von Stationen und regionale Netzwerke in verschiedenen Gebieten und Breitengraden) auf die Bestimmung von LEO-Satellitenbahnen mit/ohne ISLs. Die Ergebnisse zeigen, dass Netzwerke in hohen geographischen Breiten eine schlechtere Geometrie aufweisen als Netzwerke in mittleren/niedrigen Breiten, selbst wenn mehr Satellitenbeobachtungen zur Verfügung stehen. Dies führt zu einer schlechter bestimmten Bahn für Netze in hohen Breiten. Das Hinzufügen weiterer Stationen zu einem regionalen Netz mit 16 Stationen verbessert die Bahngenauigkeit nur geringfügig. Die Verwendung von ISL-Beobachtungen kann jedoch die Bahngenauigkeit erheblich verbessern, insbesondere bei Verwendung eines kleinen regionalen Netzwerks. Darüber hinaus ist eine genaue Kalibrierung der Satellitenverzerrungen nicht erforderlich, da sie sehr gut geschätzt werden können und kaum Einfluss auf Satellitenbahnen haben.

Eine weitere Studie über den Einfluss verschiedener ISL-Typen auf die Bahnbestimmung der LEO-Satellitenkonstellation zeigt, dass bei begrenzter Anzahl von Verbindungen die inter-orbitalen Verbindungen für die Bahnbestimmung günstiger sind als die intra-orbitalen Verbindungen. Die Inter-Layer-Inter-Satellite-Verbindungen (ILISL) spielen eine entscheidende Rolle für die Mehrschicht-Konstellation. Diese Arbeit untersucht 3 klassische ILISL-Topologien und 2 Varianten zur Bahnbestimmung. Während die Strategie "verbinden bis zum Bruch" unabhängig von Änderungen des Gewichtsfaktors konsistente Bahndifferenzfehler liefert, ist die Strategie "sofortiger Bruch" vorteilhafter, da sie zu kleineren Bahndifferenzfehlern in allen Szenarien führt.

Die Gewichtung der Daten ist entscheidend für eine genaue Bahnberechnung, wenn mehrere Messarten involviert sind. Eine falsche Gewichtung kann die Genauigkeit der Bahn beeinträchtigen. Diese Arbeit schlägt einen vereinfachten Algorithmus zur Schätzung der Varianzkomponenten (VCE) vor, um die Rechenzeit für das Satellitennetzwerk mit vielen Satelliten zu reduzieren. Dieser vereinfachte Algorithmus kann in einem Fall mit nur 30 Satelliten 124-mal schneller sein als der rigorose Algorithmus und dabei dieselbe Genauigkeit bei den berechneten Bahnen beibehalten. Dieses Verhältnis steigt exponentiell mit dem dritten Potenzwert der Anzahl an Satelliten.

Empirische Beschleunigungen werden oft verwendet, um die Orbitmodellierung zu verbessern und die Genauigkeit der Bahn zu erhöhen. Diese Arbeit diskutiert den Einfluss verschiedener empirischer Parameter-Einstellungen und Zwangsbedingungen auf die Bahnbestimmung einer LEO-Satellitenkonstellation. Die Ergebnisse zeigen, dass verschiedene Richtungen mit unterschiedlichen Schätzungsinervallen besser abschneiden. Zu lange Intervalle sind für die Bahnbestimmung nicht ideal. Sehr kurze Intervalle mit absoluten Zwangsbedingungen können eine optimale Bahnpräzision erreichen. Allerdings können übermäßig strenge Zwangsbedingungen zu größeren Bahnfehlern führen.

Eine Analyse untersucht, wie sich der formale Fehler bei verschiedenen Kombinationen von Messungstypen und Rauschpegelverhältnissen ändert. GNSS kann wesentlich mehr Daten liefern, was zu einer besseren Bahnberechnung im Vergleich zu Szenarien mit ausschliesslich Bodenstationen führt. Wenn jedoch das Rauschpegelverhältnis von Boden-/GNSS-Messungen

zu ISL-Messungen 2,5:1 überschreitet - was für die meisten Fälle zutrifft - können durch die Kombination von Boden- und ISL-Messungen kleinere formale Fehler mit weniger Beobachtungen im Vergleich zum reinen GNSS-Fall erzielt werden. Durch die Einbeziehung von ISL-Messungen kann das Wachstum der formalen Fehler aufgrund höherer Rauschpegel von Bodenmessungen und GNSS verhindert werden.

Diese Studie bestätigt die Wirksamkeit eines unabhängigen LEO-Mega-Systems durch eine hochrealistische Simulation. Durch die Nutzung von Bodenbeobachtungen aus nur sechs globalen Stationen und ISL-Beobachtungen kann das vorgeschlagene System die Umlaufbahn einer LEO-Satellitenkonstellation mit einem Fehler von nur wenigen Zentimetern bestimmen. Darüber hinaus erweist sich das unabhängige LEO-Satellitensystem im Vergleich zu Ergebnissen eines GNSS-unterstützten Systems als überlegen in Bezug auf die Genauigkeit der berechneten Bahn - sie verbessert diese um 59% gegenüber reinen GNSS-Beobachtungen.

Schlüsselwörter: Satellit in niedriger Erdumlaufbahn; Bahnbestimmung; Inter-Satelliten-Verbindung; Bodenstationnetzwerk; Schätzung der Varianzkomponente; empirische Beschleunigung; GNSS-unterstütztes System

Contents

List of figures

List of tables

Acronyms and abbreviations

ATM	Automated Teller Machine
BDS	BeiDou Navigation Satellite System
BPO	Best Possible Orbit
CHAMP	Challenging Minisatellite Payload
CMS	China Manned Space
CNES	Centre National d'Études Spatiales
CODE	Center for Orbit Determination in Europe
CPR	Cycle Per Revolution
DCB	Differential Code Bias
DLR	Deutsches Zentrum für Luft- und Raumfahrt
DOP	Dilution Of Precision
DTM	Drag Temperature Model
EIGEN	European Improved Gravity model of the Earth by New techniques
ESA	European Space Agency
EU	European Union
FAA	Federal Aviation Administration
FCC	Federal Communications Commission
FOC	Full Operational Capability
GDOP	Geometry Dilution Of Precision
GEO	Geostationary Orbit
GLONASS	Global'naya Navigatsionnaya Sputnikovaya Sistema
GMF	Global Mapping Function
GNSS	Global Navigation Satellite System
GOCE	Gravity field and steady-state Ocean Circulation Explorer
GPS	Global Positioning System
GRACE	Gravity Recovery and Climate Experiment
GRACE-FO	GRACE Follow-On
GUI	Graphical User Interface
HRD	Highly Reduced Dynamic
IADC	Inter-Agency Space Debris Coordination Committee
IERS	International Earth Rotation Service
IGS	International GNSS Service
IGSO	Inclined Geosynchronous Orbit
ILISL	Inter-Layer Inter-Satellite Link
IoT	Internet of Things
IPP	Ionospheric Pierce Point
ISL	Inter-Satellite Link
ISS	International Space Station
LBS	Location-Based Service

LeGNSS	LEO Enhanced Global Navigation Satellite System
LEO	Low Earth Orbit
MEO	Medium Earth Orbit
MIT	Massachusetts Institute of Technology
MOGA	Multi Objective Genetic Algorithm
MTT	MIT Thermospheric Mapping Function
NASA	National Aeronautics and Space Administration
NGL	Nevada Geodetic Laboratory
NOAA	National Oceanic and Atmospheric Administration
NRL	U.S. Naval Research Laboratory
PDOP	Position Dilution Of Precision
PECE	Prediction-Evaluation-Correction-Evaluation
PNT	Positioning, Navigation and Timing
POD	Precise Orbit Determination
PPP	Precise Point Positioning
RAM	Random-Access Memory
RMS	Root Mean Square
RMSE	Root-Mean-Square Error
SA	Selective Availability
SISRE	Signal-in-Space Range Error
SLR	Satellite Laser Ranging
SOC	Streets of Coverage
SRP	Solar Radiation Pressure
SSC	Swedish Space Corporation
STD	Standard Deviation
STL	Satellite Time and Location
TEC	Total Electron Content
TECU	TEC Units
UAV	Unmanned Aerial Vehicle
UPD	Uncalibrated Phase Delay
URE	User Range Error
USNO	U.S. Naval Observatory
VCE	Variance Component Estimation
VMF1	Vienna Mapping Function 1
VTEC	Vertical TEC

1 Introduction

1.1 Background

1.1.1 Fast growth in LEO satellites

Despite the uncertainties around the world, technology continues to evolve. Communication plays a crucial role in human social activities, not only in personal life but also in business and academics. Since the launch of the first artificial satellite Sputnik 1 in 1957, the concept of communication satellite has become one of the main purposes of human space exploration. In addition to the most commonly used geostationary Earth orbit (GEO) satellites, low Earth orbit (LEO) satellites have become increasingly popular in recent years.

A LEO satellite is generally defined as a satellite that orbits close to the Earth's surface. While there are varying definitions of the exact altitude range for low Earth orbit (Montenbruck & Gill, 2000, p. 2; IADC, 2007; Jäggi, 2007; Yang & de Groh, 2010; FAA, 2022), most references agree on an altitude below 1500 km. Above this altitude, the satellite is affected by the radiation from the inner Van Allen Belt (Reid et al., 2020). Due to their proximity to Earth's surface, LEO satellites have been used in various applications since the beginning of human's space exploration. The first artificial satellite, Sputnik 1, is a LEO satellite (NASA, 2022c). Space stations such as the International Space Station (ISS) and the Chinese Tiangong Space Station, as well as the Hubble Space Telescope are all located in LEO (CMS, 2022; ESA, 2022b; NASA, 2022a). LEO satellites are also widely used in Earth observation missions such as NOAA-20 and MetOp for meteorological research (eoPortal, 2017; ESA, 2022c), GOCE and GRACE for gravity field studies (ESA, 2022a; NASA, 2022b), Swarm for the magnetic field (ESA, 2022d), among others. These projects typically involve only one or a few satellites. Meanwhile, for the purpose of communication, a satellite constellation is proposed and implemented by many companies.

In the 1990s, companies such as Iridium, Globalstar and Teledesic aimed to build a LEO satellite constellation for mobile phone services. Despite successfully launching dozens of LEO satellites, these companies went bankrupt in the early 2000s due to high costs and insufficient market demand at that time (Chan, 2002; Feder, 2003). After almost a decade of technological advancements, the companies behind Iridium and Globalstar were restructured and resumed launching new LEO satellites into space. To date, 80 and 25 LEO satellites have been launched for the next generation of Iridium and Globalstar, respectively (Krebs, 2023b, 2023a). More detailed information on these constellations is provided in Table 1-1.

Since the 2010s, many companies have recognized the potential to offer affordable global communication and broadband internet services through satellites. By far, Starlink, which is proposed by SpaceX, is one of the most famous and widely used services of this kind. In 2016,

SpaceX announced that it would launch 4425 satellites into space, which are more than the total number of all existing man-made operational objects in space up to that point (SpaceX, 2016). A few months later, SpaceX filed another application to place 7518 additional satellites in a very low Earth orbit (SpaceX, 2017). Since the successful launch of two test satellites in 2018 and the first batch of 60 operational Starlink satellites in 2019, SpaceX has successfully launched 4217 satellites to date, of which 3868 are functioning (Graham, 2018; Clark, 2019; McDowell, 2023b). Since the public beta test in 2020, Starlink now provides service to more than 40 countries/regions worldwide (Mathewson, 2020; SpaceX, 2022).

In addition to SpaceX, many other companies, including OneWeb, Telesat, and Kepler, have already launched multiple satellites of their constellations into space. More companies such as Boeing, Amazon, and China Telecom Satellite Communications have also announced their similar plans to enter this emerging market. Table 1-1 provides a comprehensive overview of some well-known LEO satellite constellations.

Table 1-1 Some LEO satellite constellations

Constellation (company)	Orbit height (km)	Inclination	Number of planned satellites	Number of current satellites	Announced year / operational year	References
Globalstar-2 (Globalstar)	1410	52°	24	25	2006 / 2013	(Nichols, 2013; Globalstar, 2022; Krebs, 2023a)
Iridium-NEXT (Iridium)	780	86.4°	66	80	2007 / 2018	(Iridium, 2019; eoPortal, 2021; Krebs, 2023b)
OneWeb (OneWeb)	1200	87.4º	648	616	2015 / 2023	(Winkler, 2015; Clark, 2022; eoPortal, 2022; McDowell, 2023a)
Lightspeed (Telesat)	1015	98.98º	351	0	2016 / -	(Selding, 2016; Telesat, 2020)
	1325	50.88º	1320	0		
Starlink (SpaceX)	550	53º	1584	1465	2016 / 2020	(SpaceX, 2016, 2017; Mathewson, 2020; SpaceX, 2020; McDowell, 2023b)
	570	70º	720	300		
	560	97.6º	520	187		
	540	53.2º	1584	1569		
	345.6	53º	2547	327		
	340.8	48º	2478	20		
	335.9	42º	2493	0		

Table 1-1 (continued)

Constellation (company)	Orbit height (km)	Inclination	Number of planned satellites	Number of current satellites	Announced year / operational year	References
Kepler (Kepler)	550-650	89.5º	360	16	2018 / 2021	(Henry, 2018; Kepler, 2020, 2021; Krebs, 2023c)
Kuiper (Amazon)	630	51.9º	1156	0	2019 / -	(Amazon, 2019)
	610	42º	1296	0		
	590	33º	784	0		
GW (China Telecom Satellite Communications)	590	85º	480	0	2020 / -	(Press, 2020)
	600	50º	2000	0		
	508	55º	3600	0		
	1145	30º	1728	0		
	1145	40º	1728	0		
	1145	50º	1728	0		
	1145	60º	1728	0		
Boeing (Boeing)	1056		132	0	2021 / -	(FCC, 2021)

1.1.2 GNSS in daily life

As the LEO satellite market continues to expand, the Global Navigation Satellite System (GNSS) also becomes more and more important. Since the announcement of the free civilian use of the Global Positioning System (GPS) in 1983, the application of this technology has been rapidly integrated into people's lives (Pellerin, 2006). However, the early use was mainly limited to the transportation field, namely navigation for vehicles, such as aircrafts, cars, and ships. With the Full Operational Capability (FOC) achieved in 1995 and Selective Availability (SA) turned off in 2000, the accuracy for civilian use of GPS was greatly improved (NOAA, 2005; USNO, 2011). Since the early 2010s, GNSS has become an essential part of almost everyone's life due to the rapid growth of internet and smartphones. People now rely on their smartphones to check maps and guide their routes in real-time; book taxis or shared cars nearby; find ATMs, restaurants or supermarkets; chat or meet others based on location; play games like Pokémon Go outside - all thanks to GNSS which is one of the backbones behind these location-based services (LBS). In fact, by 2021 LBS market reached a value of $27.28 billion U.S. Dollars and is expected to grow up to $96.85 billion U.S. Dollars by 2027 (ResearchAndMarkets, 2022).

Currently there are four GNSSs in operation: the U.S.'s GPS, Russia's Global'naya Navigatsionnaya Sputnikovaya Sistema (GLONASS), China's BeiDou Navigation Satellite System (BDS) and European Union (EU)'s Galileo. Table 1-2 provides a summary of these

systems.

Table 1-2 Summary of current GNSSs (Hegarty & Chatre, 2008; Navipedia, 2014, 2018; Howell, 2020; Navipedia, 2021; Arianespace, 2022)

	GPS	GLONASS	BDS	Galileo
Owner	U.S.	Russia	China	EU
Orbit height (km)	20200	19100	21500 / 35786 / 35786	23200
Inclination	55º	65º	55º / 55º / 0	56º
Number of satellites	24	24	27 / 3 / 5	30
Initial launch year	1978	1982	2000	2005
FOC year	1995	1995	2020	2025

1.1.3 Potential of LEO in positioning

As people become more accustomed to the benefits of GNSS, they are also becoming aware of its drawbacks. Most GNSS satellites are in medium Earth orbit (MEO), which is much higher than LEO satellites. This results in weak signals that can be easily jammed or spoofed. GNSS signals are also difficult to receive indoors. Additionally, obtaining an ambiguity-fixed solution for precise point positioning (PPP) may take a long time without a dense regional reference network (Reid et al., 2018; Ma et al., 2020).

In contrast, LEO satellites do not suffer from these issues. Studies have already shown that in an indoor environment, GPS receivers can only track 1-2 satellites at most. However, by using the Satellite Time and Location (STL) service, which is powered by the Iridium constellation, receivers can always get strong signals and more visible satellites (Reid et al., 2020). Compared to MEO satellites, one of the main disadvantages of LEO satellites is their coverage. Because LEO satellites are much closer to the Earth's surface, their footprints are smaller. This means that it takes many more LEO satellites than MEO satellites to achieve global coverage. However, as Table 1-1 shows, many of the proposed LEO satellite constellations have hundreds or even thousands of satellites. With such a large number of LEO satellites, global coverage should be achievable. Naturally, researchers began to explore the possibilities and limitations of using such constellations for positioning and beyond.

1.2 State of the art

Reid et al. (2018) conducted a study on the feasibility of using LEO satellite constellations for navigation, examining factors such as geometry, hardware, user range error (URE), and radiation environment. Their findings indicate that LEO satellite constellations can offer three

times better geometry than current GNSS systems, resulting in comparable position accuracy to GPS even with less accurate onboard clocks. In subsequent studies by Reid et al. (2020) and Kassas (2020), detailed analyses were performed on the technique details of navigation from LEO satellites including theoretical background, development history, measurement models and error sources. Simulation results demonstrate that thanks to the strong signal from LEO satellites, when the unmanned aerial vehicle (UAV) only has access to the GPS signals for the first 100 s, the LEO-assisted system can improve the position root-mean-square error (RMSE) from 52.6 m to 10.5 m compared to relying solely on the inertial navigation system.

Li et al. (2019a) and Ge et al. (2021) looked at the opportunities from a different perspective. They proposed enhancing the current GNSS with a future LEO mega-constellation, which they called the LEO Enhanced Global Navigation Satellite System (LeGNSS). They reviewed the progress of LEO satellite constellation development and discussed the advantages and challenges of this new system in orbit and clock determination, PPP, global ionosphere monitoring, and Earth reference frame determination. The authors concluded that additional LEO satellites can significantly improve orbit and clock products of GNSS as well as reduce convergence time for PPP. Li et al. (2019a) and Ge et al. (2020b) provided further details on LeGNSS by adding 66 LEO Iridium-like satellites to the BDS and GPS systems, demonstrating greatly improved geometry dilution of precision (GDOP) in polar areas and achieving centimeter-level signal-in-space range error (SISRE). With 240 LEO satellites located at different inclinations, the convergence time for PPP can be reduced to one minute.

Li et al. (2018) also mentioned a similar idea called LEO augmented multi-GNSS. The simulation shows that in the mid-latitude area, the multi-GNSS PPP convergence time can be reduced from 9.6 min to 7.0 min with 60 additional LEO satellites, and increasing the number of LEO satellites to 288 can further shorten it to only 1.3 min. In contrast, a GPS-only PPP takes about 25 min while an LEO-only PPP with a constellation of 192 satellites takes only about 6.5 min. Later, Li et al. (2021b) analyzed this augmented system in harsh environments. Under signal shielding conditions, augmenting the system with a constellation of 96 LEO satellites can shorten the PPP convergence time for multi-GNSS by up to 75.3%, and decrease cycle slip fixing time from 3.3 min to just 0.8 min. However, when significant multipath effects are present, using an LEO satellite may result in noisier PPP solutions due to their short continuous observation time compared with other GNSS systems available today.

In addition to positioning and navigation, the LEO satellite constellation has potential in other geodetic fields. Ren et al. (2020) and Ren et al. (2021) investigated how LEO satellites can augment global ionospheric models, with simulation results showing that observations from these satellites can expand coverage and increase the density of ionospheric pierce points (IPP). This density of IPP goes even higher with more available LEO satellites. Combining data from both LEO and GNSS sources reduced the root mean square (RMS) error of ionospheric models by over 20% compared to using GNSS data alone. Li et al. (2021c) analyzed real data from several LEO satellites to estimate differential code bias (DCB), achieving a stability with standard deviation (STD) of 0.051 ns that is even better than products from Deutsches Zentrum für Luft- und Raumfahrt (DLR). Similar research by Yuan et al. (2021) confirmed the benefits of LEO satellites. The GPS satellite DCB solutions based on multi-LEO observations are close to the product from Center for Orbit Determination in Europe (CODE). Xiong et al. (2021)

investigated the LEO constellation augmented system for 3D water vapor tomography. By adding 288 LEO satellites, the observation time of 30 min ray distribution effect of GNSS can be shortened by 66.7%. At the horizontal resolution of 13 × 14 grid, compared with GPS, the empty-voxel ratio of this augmented system is reduced by about 23%. Using onboard receiver from 9 LEO satellites, Li et al. (2022b) estimated uncalibrated phase delay (UPD). By applying LEO-based UPD with observations from nine LEO satellites, the average convergence time for PPP ambiguity resolution can be reduced by 24% compared to float solutions. Although the current results are slightly inferior to ground-based UPD, it is expected that the performance will continue to improve with numerous LEO satellites in the future.

1.3 Motivation and overview

As mentioned earlier, with such a great potential of GNSS and thousands of LEO satellites soon to be in space, some researchers have already begun to explore the possibility of combining these two domains. In theory, GNSS is nothing more than a passive autonomous positioning system based on the measurement of signal propagation time. If these LEO satellites could carry some essential payload to broadcast the necessary information for navigation, they could form an effective global navigation satellite system. In this way, the value of these massive LEO satellite constellations can be maximized, as they could not only provide telecommunications and internet services, but also serve as a high-quality navigation system. Considering the number of these LEO satellites and constellations, they could become strong supporters for traditional GNSS and create opportunities for regular companies to enter the market that has long been monopolized by governments and militaries.

To fulfill this purpose, it is necessary to ask and answer certain technical questions, as well as thoroughly investigate various aspects. To begin with, how to build a constellation that can be used for both communication and positioning? Traditional navigation satellites are mostly located in MEO, which has different priorities than LEO. Additionally, current LEO satellite constellations prioritize communication and broadband internet services. As a result, certain conditions and parameters for a LEO positioning constellation need to be reevaluated. To design such a multi-functional constellation, several factors need to be considered:

1. What are the requirements and criteria for selecting such a constellation?
2. Which type of constellation is most desirable?
3. How should the constellation parameters be chosen effectively?
4. How well does the designed constellation perform?

Precise orbit determination is essential for various applications mentioned above. Typically, observations from GNSS satellites are used to determine the orbit of LEO satellites. However, as the number of LEO satellites increases, a system that utilizes observations from both ground stations and inter-satellite links (ISL) could be advantageous. This approach eliminates errors associated with the GNSS technique such as orbit modeling errors in GNSS satellite products and ensures independence. Therefore, it is necessary to investigate the

technical details and feasibility of an independent system that uses both ground stations and ISLs for precise orbit determination. To achieve this goal, it is necessary to thoroughly examine various specific configurations and details.

1. How to choose or develop software that meets the requirements of this work?
2. Empirical accelerations are essential for precise orbit determination, particularly in complex and dynamic systems. The challenge lies in selecting a set of empirical parameters that strike the right balance between orbit accuracy and computational efficiency.
3. Observations from ground stations are crucial for determining the orbit of an independent satellite constellation. However, the distribution and number of ground stations may not always be optimal due to various factors. How large can a ground station network affect the orbit accuracy? Specifically, what is the influence of network size and distribution on satellite orbits? Can additional observations from ISL help to mitigate these errors?
4. ISL has been proven effective in improving orbit accuracy. The accuracy of determined orbits can be influenced by different link topologies. What is the impact of different links on orbit determination? Especially for constellations with satellites at different orbital heights, the high-low type of linking is crucial for enhancing system integrity. However, there is a lack of research on this topic. How to find an effective scheme for this type of link? This work aims to address these questions and explore effective schemes of ISL for orbit determination.
5. By introducing new technologies like ISL, new types of observations are made available. These different observation types have varying levels of accuracy. When combining these diverse observation types for orbit determination, the challenge lies in determining the appropriate weights for each type to enhance orbit accuracy. This becomes particularly complex when dealing with thousands of satellites and millions of observations. Additionally, it is important to consider how different modeling errors may impact data weighting.
6. How does the independent LEO system perform in a realistic simulation, considering all these effects and techniques?
7. Currently, GNSS observations from onboard receivers are commonly used for determining the orbit of LEO satellites. How does this independent system compare to the traditional GNSS-assisted system? Moreover, since simulations cannot fully replicate the complex real-world environment and measurement accuracy can be enhanced through technological advancements, how would these results change when different noise levels are taken into account?

These questions and problems are crucial for studying and developing the LEO mega-constellation, particularly as an independent system for navigation. This work aims to investigate and provide answers to these questions.

This work is structured as follows.

Chapter 2 provides a detailed explanation of the theoretical background for orbit determination that will be used in this work. It covers the fundamentals of orbit propagation and estimation, as well as typical force models, with a focus on non-gravitational perturbations that are typically challenging for modelling for LEO satellites. Additionally, special techniques utilized in this work - including variance component estimation (VCE), parameter pre-elimination, empirical accelerations, and parameter constraining - are discussed in this chapter.

Chapter 3 delves into the design of satellite constellations, introducing various constellation types and design methods. The selection of an appropriate constellation type and design method for this work is based on global observability considerations. This chapter carefully selects relevant parameters to create a constellation that can function as both a communication tool and positioning system. Selection criteria include factors such as the number of visible satellites, DOP, and cost. Ultimately, a suitable candidate for further study is chosen.

Chapter 4 presents and discusses the detailed configurations and techniques used in orbit determination for this work. A new software was developed specifically for simulating and determining LEO satellite mega-constellations. Empirical accelerations are often used in the orbit determination process to improve modeling. This chapter compares different empirical parameter settings and proposes the option that best fits the application of this work. The impact of ground station network distribution and number of stations on orbit accuracy is addressed, as well as the potential benefits of additional ISL observations. Since there are different types of ISL, especially for systems with satellites at varying altitudes, it is necessary to discuss their effect on orbit determination and to select an appropriate strategy. While equipping ISL seems attractive due to its potential, introducing measurements with varying accuracies raises questions about how to determine their weights. Therefore, data weighting algorithms and their impact will be investigated. Finally, this chapter integrates all the previously mentioned techniques and conducts simulations that consider various effects to closely reflect reality. The results demonstrate the feasibility of the independent system with the aid of the introduced techniques in this work.

Chapter 5 compares the independent LEO satellite system with the traditional GNSS-assisted system. The analysis begins by examining the impact of varying measurement accuracies on orbit determination. This approach expands upon the conclusions presented in this work, moving beyond simulation in this work and into practical application. Ultimately, a comparison between the two systems reveals that the independent system outperforms its GNSS-assisted counterpart, as evidenced by lower orbit error results.

Chapter 6 provides a summary of the methods and conclusions presented in this work. Additionally, potential avenues for future research are discussed.

2 Fundamentals of orbit determination

2.1 Introduction

Satellite orbit determination refers to the process of determining the motion such as position and velocity of a satellite with respect to the center of the Earth in a given coordinate frame (Tapley et al., 2004, p. 1). Precise orbit determination (POD) is an important requirement for many space applications, especially in the field of geodesy. In general, POD is achieved by using observations to get the best estimate of a satellite's state. The observations are usually collected by onboard equipment and ground stations, such as range, range-rate, phase, elevation, azimuth and so on. These observations usually have a nonlinear relationship with the state variables such as position and velocity. The state is a set of parameters that characterize the motion of the satellite. The position and velocity or Keplerian elements at the initial epoch are often used as this set of parameters. Due to the complex representation of the force models and the lack of detailed knowledge of the physical environment, errors in the observations and the mathematical model are inevitable. In addition, there are also errors during the estimation process, such as numerical integration, computational truncation, and roundoffs. Because of these errors, the estimated orbits cannot exactly match with the true orbits. One can only iterate the process to get the best estimate of the true orbits (Tapley et al., 2004, pp. 1-2; Vetter, 2007).

The orbit determination problem typically involves two steps: initial orbit determination and orbit improvement. The initialization step is crucial for the entire process. Poor approximation during initialization can cause divergence in later iterations. Or, if multiple solutions are found at the initialization, the iterative process could switch from one to the other. This would lead to an uncertainty about the correct solution (Beutler, 2005b, p. 361). Initial orbit determination relies heavily on intuition, imagination, and opinions of individuals. Gauss and Laplace were pioneers in this field with their approaches called first orbit determination as a boundary value problem and first orbit determination as an initial value problem, respectively. Laplace's approach calculates position and velocity at the epoch in the middle of observation interval but may not be suitable for long tracking arcs where velocity needs to be calculated by interpolating position measurements. Gauss' method was designed to solve orbital elements from three sets of widely distributed direction measurements. For satellites, it may also be useful to solve the orbit from two position vectors (Montenbruck & Gill, 2000, p. 39; Beutler, 2005b, pp. 366-396). In satellite geodesy, the importance of initial orbit determination is somewhat diminished. On the one hand, the initial orbits are usually provided with a rough but sufficient accuracy to proceed directly to the second step and compute the precise orbits. On the other hand, in many scientific applications, orbit determination is a part of a more general parameter estimation problem. In addition to the orbital elements, other parameters such as dynamical and measurement model parameters are also estimated during the process to improve the accuracy. As a result, for a satellite, the significance of initial orbit determination may be attenuated (Beutler, 2005b, pp. 361-362).

There are three traditional methods for orbit modeling of LEO satellites: kinematic, dynamic, and reduced dynamic. The kinematic method estimates the epoch-wise kinematic coordinates and provides a table of satellite positions with an interval defined by the measurement rate. This method can be applied to many scenarios because there are no constraints on receiver motion. However, kinematic positioning is sensitive to bad measurements and data interruptions. The dynamic method uses physical models of satellite motion to determine the best orbital trajectory to fit the measurements. It estimates not only the initial osculating elements, but also the dynamical and measurement model parameters. Compared to the kinematic method, it requires knowledge of an a priori trajectory but can greatly reduce the estimated parameters and is more robust against bad measurements. The reduced dynamic method was introduced by Yunck et al. (1990) and Wu et al. (1991) as an improvement over the orbit solution provided by the kinematic method while being less complex than the dynamic one. It allows additional stochastic parameters such as pseudo-stochastic pulses or systematic noise into the equations of motion for better complementation of satellite models (Beutler, 2005b, pp. 426-427; Jäggi, 2007, pp. 42-47). Fig. 2-1 provides a qualitative representation of the relationship between these methods. It is worth noting that if only a few pseudo-stochastic parameters are introduced or if the constraints are too strict, it will still result in a dynamic orbit. However, when the number of unconstrained pseudo-stochastic parameters reaches a maximum, namely epoch by epoch, it is possible to achieve a kinematic orbit (Jäggi, 2007, pp. 47-48).

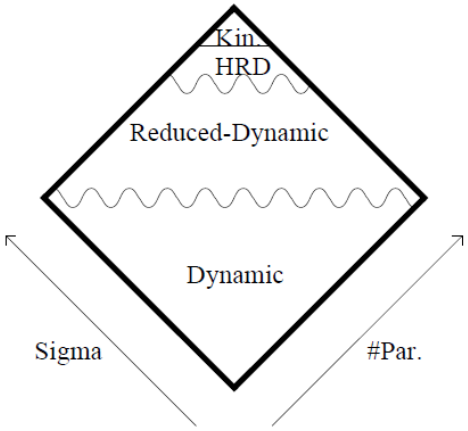

Fig. 2-1 Relationship of orbit modeling methods. HRD refers to highly reduced dynamic; Kin. refers to kinematic. Orbit determination as a function of the number (#Par.) and a priori standard deviation (Sigma) of the pseudo-stochastic parameters (Jäggi, 2007, p. 47)

There are two commonly used methods for estimating orbits: the least-squares method and the Kalman filter. The least-squares method was first proposed by Gauss in the late 18th century to determine planetary orbits, and a century later applied by Helmert in geodesy. This method involves finding parameter estimates that best fit an orbital trajectory to observations in a least-squares residual sense. Namely, the estimate should minimize the sum of the squares of the difference between the modeled observations and the actual observations. In 1960, Kalman

introduced a mathematically rigorous approach for processing the observations of a linear dynamic system sequentially (Kalman, 1960). Based on his work and many subsequent publications, this method, known as the Kalman filter, has become popular due to its many applications. Unlike the classical least-squares method, which estimates the parameters by processing the complete set of observations together in each iteration, the Kalman filter processes the observations as soon as they are received. In other words, the idea of the Kalman filter is to use the state and covariance from the previous epoch and the observation from the current epoch to improve the state vector of that epoch. A comparison of these two methods is shown in Fig. 2-2; both have unique characteristics suited for different applications. As mentioned before, a major difference is that the classical least-squares method estimates parameters using the full set of observations, while the Kalman filter processes measurements sequentially. This also leads to different requirements for computer memory size since the least-squares method needs all measurements and the Kalman filter does not need measurements from previous steps. However, the least-squares method is more robust than the Kalman filter as it considers all observations and can easily identify bad data with large residuals compared to averaged values. In contrast, the Kalman filter requires careful balancing of a priori covariance, measurement weights, and process noise. Therefore, the Kalman filter is more suitable for real-time state estimation applications such as on-board navigation for manned or unmanned spacecraft like the Apollo program or interplanetary orbit determination and navigation. On the other hand, offline orbit determination of Earth-related satellites and geodetic parameter estimation prefer using least-squares methods due to their preference in recognizing outliers in data sets and low computational burden. As a result, many operational and scientific orbit determination programs use this technique (Montenbruck & Gill, 2000, pp. 258-260, 276-282, 286-288; Tapley et al., 2004, pp. 13, 173-174, 199-201). This work will adopt the least-squares method which will be explained further in chapter 2.3.

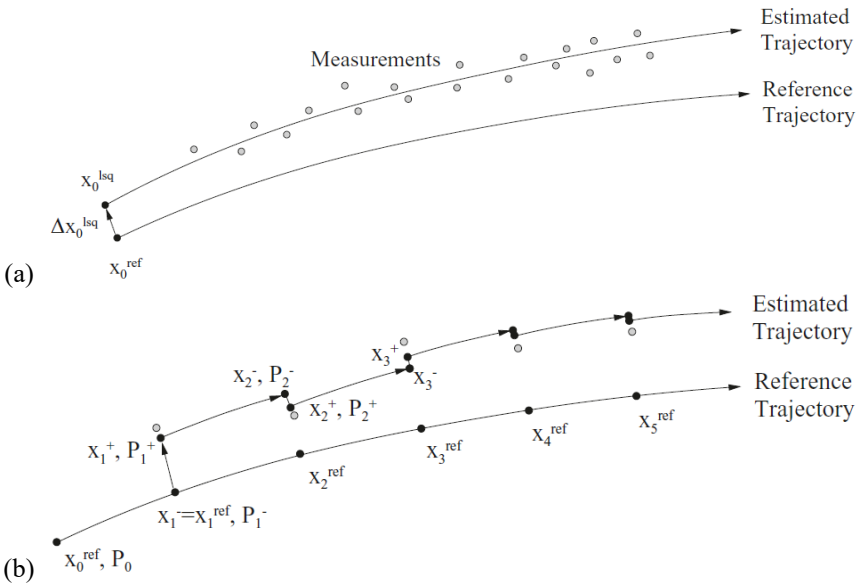

Fig. 2-2 Orbit determination by: (a) least-squares method and (b) Kalman filter (Montenbruck & Gill, 2000, pp. 260, 281)

This chapter 2 provides the essential theoretical framework for orbit determination utilized in this study.

2.2 Numerical integration

To determine and predict the orbit state of a satellite at a specific time, an orbit propagator is required to calculate its state based on its initial state. In earlier times, analytical computation methods such as Hamiltonian normalization were used for this purpose. However, with the significant advancements in computational power and the ability to provide high accuracy using various force models, numerical integration has become the preferred method. Numerous techniques have been developed for numerical integration of ordinary differential equations (Montenbruck & Gill, 2000, p. 117; Berry & Healy, 2020). There are two types of numerical integration: single-step and multi-step methods. Single-step methods use only one previous point and its derivative to determine the current value, making each integration step independent of the others. This method is easy to implement and suitable for differential equations with rapid changes in the function to be integrated. Examples include Runge-Kutta and extrapolation methods. In contrast, the multi-step method improves efficiency by using information from previous steps to reduce the total number of function evaluations required. It is much more efficient when dealing with differential equations that involve a lot of arithmetic operations. Adams-Bashforth, Stoermer-Cowell, and Gauss-Jackson methods are all examples of the multi-step method (Bashforth & Adams, 1883; Cowell & Crommelin, 1909; Jackson, 1924; Montenbruck & Gill, 2000, pp. 117, 132).

Additionally, from another perspective, numerical integration can be approached through fixed-step size or adaptive step size methods. The former employs a constant step size for each integration, while the latter adjusts the step size based on specific criteria such as truncation error. The main reason for using this type of step size control is to achieve predetermined accuracy with minimal computational effort. For example, when simulating satellite movement close to Earth and dealing with complex dynamics, small step sizes are taken; whereas larger steps are used when the satellite is far from Earth to improve efficiency (Raptis & Cash, 1985; Press & Teukolsky, 1992). However, in simulation scenarios using an adaptive step size method may result in unexpected outcomes. Even if perfect measurements without any noise and exact reference models identical to true models are employed, slight variations in computed step sizes between two runs may lead to very small orbit errors. Although this computation error is negligible in practice, adopting a fixed-step method ensures repeatability and consistency of simulations.

In this chapter, the theoretical background of the multi-step fixed-step integrator that is used in this work is discussed in detail. For more information on each type of integration method, please refer to Hairer et al. (1993) and Montenbruck and Gill (2000). The contents presented in this chapter are primarily summarized from Montenbruck and Gill (2000, pp. 117-156). Unless otherwise indicated, this reference will not be cited repeatedly in this chapter.

For the initial state vector $\boldsymbol{y}$ of a satellite, which contains its position $\boldsymbol{r}$ and velocity $\dot{\boldsymbol{r}}$, an ordinary differential equation can be written as

$$\dot{\boldsymbol{y}} = \frac{d\boldsymbol{y}}{dt} = \boldsymbol{f}(t, \boldsymbol{y}) \tag{2-1}$$

where

$$\boldsymbol{y} = \begin{pmatrix} \boldsymbol{r} \\ \dot{\boldsymbol{r}} \end{pmatrix} \tag{2-2}$$

With an initial value $\boldsymbol{y}_0 = \boldsymbol{y}(t_0)$, one can get an approximate value of $\boldsymbol{y}$ at a later time $t_0 + h$ from a first-order Taylor expansion with

$$\boldsymbol{y}(t_0 + h) \approx \boldsymbol{y}_0 + h \cdot \boldsymbol{\Phi} = \boldsymbol{\eta}(t_0 + h) \tag{2-3}$$

where h denotes the step size, $\boldsymbol{\Phi}$ denotes the increment function, and $\boldsymbol{\eta}$ denotes the approximate value of $\boldsymbol{y}$.

At the end of 19th century, Carl Runge and Wilhelm Kutta developed the renowned Runge-Kutta method. This method utilizes slopes at various points in one integration steps. To generalize the classical 4th-order Runge-Kutta method, the increment function $\boldsymbol{\Phi}$ of the explicit Runge-Kutta method can be written as

$$\boldsymbol{\Phi} = \sum_{i=1}^{s} b_i \boldsymbol{k}_i \tag{2-4}$$

with integer s indicates the number of stages, and coefficients

$$\begin{aligned} \boldsymbol{k}_1 &= \boldsymbol{f}(t_0 + c_1 h, \boldsymbol{y}_0) \\ \boldsymbol{k}_i &= \boldsymbol{f}\left(t_0 + c_i h, \boldsymbol{y}_0 + h \sum_{j=1}^{i-1} a_{ij} \boldsymbol{k}_j\right) \quad i = 2 \dots s \end{aligned} \tag{2-5}$$

These coefficients are selected to maximize the order of the local truncation error. A commonly used criterion for selecting these coefficients is

$$\sum_{i=1}^{s} b_i = 1, \qquad c_1 = 0, \qquad c_i = \sum_{j=1}^{i-1} a_{ij} \quad i = 2 \dots s \tag{2-6}$$

Butcher's research demonstrated that there are order barriers for explicit *s*-stage Runge-Kutta methods, indicating that the method's order *p* cannot exceed *s*. Specifically, it must hold true that $s \geq p$ (Butcher, 2016, pp. 200-204). Table 2-1 provides a summary of the relationship between *s* and *p*. However, orders greater than 8 are less desirable due to their unknown minimal stage requirements.

Table 2-1 Required minimal stages of explicit Runge-Kutta method for different orders (Butcher, 2016, pp. 185-210)

Order *p*	1	2	3	4	5	6	7	8
Min stage *s*	1	2	3	4	6	7	9	11

The previously mentioned Runge-Kutta method is a single-step approach. However, in 1883, Bashforth and Adams introduced the concept of utilizing multiple previous steps to estimate the solution at a given point. This technique became known as the Adams-Bashforth method. Further research by Moulton led to the development of the Adams-Moulton method (Butcher, 2016, p. 111). In the following, these two methods will be briefly discussed.

By integrating equation (2-1) with respect to *t* from t_i to t_{i+1}, one gets

$$\boldsymbol{y}(t_{i+1}) = \boldsymbol{y}(t_i) + \int_{t_i}^{t_i+h} \boldsymbol{f}\big(t, \boldsymbol{y}(t)\big)\, dt \tag{2-7}$$

Here, $\boldsymbol{f}\big(t, \boldsymbol{y}(t)\big)$ can be replaced by a polynomial, since the integral depends on $\boldsymbol{y}(t)$, which is unknown, and cannot be evaluated. Thus, equation (2-7) can be rewritten as

$$\boldsymbol{\eta}_{i+1} = \boldsymbol{\eta}_i + \int_{t_i}^{t_i+h} \boldsymbol{p}(t)\, dt \tag{2-8}$$

where $\boldsymbol{\eta}$ denotes the approximate value of $\boldsymbol{y}$, $\boldsymbol{p}(t)$ is the polynomial function. Like equation (2-3), the increment function of a multi-step method can be deduced

$$\boldsymbol{\Phi} = \frac{1}{h}\int_{t_i}^{t_i+h} \boldsymbol{p}(t)\, dt \tag{2-9}$$

Assuming that the value $\boldsymbol{y}$ or its approximate value $\boldsymbol{\eta}$ for the previous *m* points $(t_{i-m+1}, \dots, t_i)$ are already known, one may get the increment function of *m*-th order Adams-Bashforth method can be written as

$$\boldsymbol{\Phi}_{ABm} = \frac{1}{h}\int_{t_i}^{t_i+h} \boldsymbol{p}_m^i(t)\, dt = \sum_{j=0}^{m-1} \gamma_j \nabla^j \boldsymbol{f}_i \tag{2-10}$$

where the coefficient can be calculated from a recurrence relation

$$\gamma_j = 1 - \sum_{k=0}^{j-1} \frac{1}{j+1-k}\gamma_k \tag{2-11}$$

and the backward differences of $\boldsymbol{f}_i$

$$\begin{gathered} \nabla^0 \boldsymbol{f}_i = \boldsymbol{f}_i \\ \nabla \boldsymbol{f}_i = \boldsymbol{f}_i - \boldsymbol{f}_{i-1} \\ \nabla^n \boldsymbol{f}_i = \nabla^{n-1} \boldsymbol{f}_i - \nabla^{n-1} \boldsymbol{f}_{i-1} \end{gathered} \tag{2-12}$$

The Adams-Moulton method is a multi-step approach that differs from the Adams-Bashforth method in its use of values. While the latter utilizes *m* points ranging from t_{i-m+1} to t_i, the former employs values between t_{i-m+2} and t_{i+1}. The increment function for an *m*-th order Adams-Moulton method can be expressed as follows

$$\boldsymbol{\Phi}_{AMm} = \frac{1}{h}\int_{t_i}^{t_i+h} \boldsymbol{p}_m^{i+1}(t)\,dt = \sum_{j=0}^{m-1} \gamma_j^* \nabla^j \boldsymbol{f}_i \tag{2-13}$$

where

$$\gamma_j^* = -\sum_{k=0}^{j-1} \frac{1}{j+1-k}\gamma_k^* \tag{2-14}$$

Both the Adams-Bashforth and Adams-Moulton methods have the same order, *m*. However, the Adams-Bashforth method is less stable and accurate than the Adams-Moulton method. However, since the Adams-Moulton method depends on the value at the t_{i+1} point, it is not possible to compute an approximate solution $\boldsymbol{\eta}_{i+1}$ directly. It is therefore an implicit method and requires an iterative procedure to solve.

In practice, researchers often use the Prediction-Evaluation-Correction-Evaluation (PECE) method, which combines the Adams-Bashforth method and the Adams-Moulton method. The PECE method involves four steps:

1. Prediction: Calculate the initial solution $\boldsymbol{\eta}_{i+1}^p$ at t_{i+1} using the Adams-Bashforth method.
2. Evaluation: Find the corresponding function value $\boldsymbol{f}_{i+1}^p$ using the solution from prediction $\boldsymbol{\eta}_{i+1}^p$.
3. Correction: Apply the Adams-Moulton method with $\boldsymbol{f}_{i+1}^p$ to obtain a corrected estimate $\boldsymbol{\eta}_{i+1}$.
4. Evaluation: Use the corrected solution $\boldsymbol{\eta}_{i+1}$ to get an updated function value $\boldsymbol{f}_{i+1}$. This value can then be used for starting the next integration step.

The last two steps theoretically require iteration to find an exact solution, but since this is time-consuming and one single correction is usually accurate enough, a simple correction with PECE method is often sufficient.

In this study, orbit propagation is achieved using a multi-step fixed-step size integrator. Specifically, an 8th order fixed-step size Runge-Kutta method is initially employed to calculate the initial steps for the multi-step integration process. The coefficients used in this method can be found in Hairer et al. (1993, pp. 181-185). Subsequently, an 8th order fixed-step size PECE method is utilized for further propagation of the orbit.

2.3 Least-squares adjustment

Chapter 2.1 highlights that the least-squares adjustment is a commonly used method for orbit determination. The main concept of this approach is explained in detail within this chapter, with subsequent content being summarized and referenced from Montenbruck and Gill (2000, pp. 258-262), Tapley et al. (2004, pp. 160-178), and Jäggi (2007, pp. 36-38). Unless otherwise

stated, these references will not be repeatedly cited throughout the chapter.

In the general orbit determination problem, the dynamics and measurements involve nonlinear relationships with the state

$$\begin{aligned} \dot{\boldsymbol{x}} &= \boldsymbol{f}(t, \boldsymbol{x}) \\ \boldsymbol{x}_0 &= \boldsymbol{x}(t_0) \\ z_i(t_i) = g_i\big(t_i, \boldsymbol{x}(t_i)\big) + \epsilon_i &= h_i(t_i, \boldsymbol{x}_0) + \epsilon_i \end{aligned} \tag{2-15}$$

where $\boldsymbol{x}$ is the unknown *m*-dimensional state vector. Usually, this vector may consist of

$$\boldsymbol{x}(t) = \begin{pmatrix} \boldsymbol{r}(t) \\ \boldsymbol{v}(t) \\ \boldsymbol{p} \\ \boldsymbol{q} \end{pmatrix} \tag{2-16}$$

Here, $\boldsymbol{r}$ and $\boldsymbol{v}$ indicate the satellite's position and velocity, $\boldsymbol{p}$ and $\boldsymbol{q}$ represent the parameters that affect the force and measurement model, respectively. $\boldsymbol{x}_0$ in equation (2-15) is the initial value at epoch t_0. z_i is the measurement, which is used to determine $\boldsymbol{x}$, at epoch t_i, with $i = 1, \dots, n$. g_i denotes the model value of the *i*-th observation as a function of time t_i and the state $\boldsymbol{x}$ at this epoch; while h_i denotes the same value as a function of the initial state $\boldsymbol{x}_0$. ϵ_i is the errors in the observations, which are assumed to be randomly distributed with zero mean value.

The least-squares method is to find the state $\boldsymbol{x}_0^{lsq}$ that minimizes the loss function *J*

$$J(x_0) = \boldsymbol{\varepsilon}^T \boldsymbol{P} \boldsymbol{\varepsilon} = \big(\boldsymbol{z} - \boldsymbol{h}(\boldsymbol{x}_0)\big)^T \boldsymbol{P} \big(\boldsymbol{z} - \boldsymbol{h}(\boldsymbol{x}_0)\big) \tag{2-17}$$

where $\boldsymbol{\varepsilon}$ is the observation residual; $\boldsymbol{P}$ is the weight matrix of the observations, more specifically

$$\boldsymbol{P} = \boldsymbol{Q}_{yy}^{-1} = \sigma_0^2 \boldsymbol{C}_{yy}^{-1} \tag{2-18}$$

where $\boldsymbol{Q}_{yy}$ is the cofactor matrix of the observations; σ_0 is the a priori standard deviation of the unit weight; $\boldsymbol{C}_{yy}$ is the covariance matrix of the observations. If the observations are uncorrelated, the weight matrix $\boldsymbol{P}$ becomes a diagonal matrix, with the diagonal elements $P_{kk} = \frac{\sigma_0^2}{\sigma_k^2}$, where σ_k^2 is the variance component of the corresponding observation *k*.

Due to the non-linear function, it is difficult to locate the minimal value of the loss function without additional information. Usually, the equation (2-15) can be linearized by expanding it into a Taylor series around a reference state $\boldsymbol{x}_0^{ref}$, which is given by known a priori initial value $\boldsymbol{x}_0^{apr}$. Namely, the observation residual can be written as

$$\boldsymbol{\varepsilon} = \boldsymbol{z} - \boldsymbol{h}(\boldsymbol{x}_0) \approx \boldsymbol{y} - \boldsymbol{A} \Delta \boldsymbol{x}_0 \tag{2-19}$$

where $\boldsymbol{y} = \Delta \boldsymbol{z} = \boldsymbol{z} - \boldsymbol{h}\big(\boldsymbol{x}_0^{ref}\big)$ is the difference between actual observations and predicted

observations from reference trajectory. $\boldsymbol{A} = \frac{\partial \boldsymbol{h}(\boldsymbol{x}_0)}{\partial \boldsymbol{x}_0}|_{\boldsymbol{x}_0=\boldsymbol{x}_0^{ref}}$ is a Jacobian matrix that gives the partial derivatives of the modeled observations with respect to the stat vector at the reference epoch. It is also called design matrix. $\Delta\boldsymbol{x}_0 = \boldsymbol{x}_0 - \boldsymbol{x}_0^{ref}$ is the difference between $\boldsymbol{x}_0$ and the reference state, or the correction with respect to the reference state.

According to equation (2-17) and equation (2-19), the general solution of the least-squares problem can then be written as

$$\Delta\boldsymbol{x}_0^{lsq} = (\boldsymbol{A}^T\boldsymbol{P}\boldsymbol{A})^{-1}\boldsymbol{A}^T\boldsymbol{P}\boldsymbol{y} = \boldsymbol{N}^{-1}\boldsymbol{b} \tag{2-20}$$

where $\boldsymbol{N} = \boldsymbol{A}^T\boldsymbol{P}\boldsymbol{A}$ is the normal equation matrix; $\boldsymbol{b} = \boldsymbol{A}^T\boldsymbol{P}\boldsymbol{y}$ is the right-hand-side vector.

Due to the linearization, the procedure usually has to be iterated until the correction of the parameters $\Delta\boldsymbol{x}_0$ falls below a defined threshold. The threshold can be defined differently according to different requirements, such as the formal error of the parameters, the corrected position increment, etc.

The least-squares method is typically viewed as a batch estimation technique, where all measurements are processed together in each iteration. This sets it apart from the Kalman filter, which processes measurements sequentially. As discussed in chapter 2.1, this characteristic makes the least-squares method more robust. However, when there are too many observations, the design matrix $\boldsymbol{A}$ becomes very large. This presents two issues: firstly, storing such a matrix requires significant computer memory; secondly, it increases the computation burden of the matrix operation of the normal equation matrix $\boldsymbol{N}$. Additionally, if new measurements are introduced during the batch least-squares estimation, re-computing the entire problem is inefficient. To address these challenges and assuming that observations are independent of one another, one may propose using sequential batch least-squares estimation instead of traditional batch processing to compute measurements individually rather than all at once during estimation.

Since measurements are assumed to be uncorrelated, for a total number of *n* measurements, the design matrix $\boldsymbol{A}$ can be considered as a group of design matrix $\boldsymbol{A}_i$ with dimension $1 \times m$, where *m* is the dimension of state vector $\boldsymbol{x}$. And similarly to $\boldsymbol{y}$

$$\boldsymbol{A} = \begin{bmatrix} \boldsymbol{A}_1 \\ \vdots \\ \boldsymbol{A}_i \\ \vdots \\ \boldsymbol{A}_n \end{bmatrix}, \qquad \boldsymbol{y} = \begin{bmatrix} \boldsymbol{y}_1 \\ \vdots \\ \boldsymbol{y}_i \\ \vdots \\ \boldsymbol{y}_n \end{bmatrix}, \qquad i = 1, \dots, n \tag{2-21}$$

The normal equation matrix $\boldsymbol{N}$ and right-hand-side vector $\boldsymbol{b}$ can then be separated into the sum of several sub-normal equation matrices $\boldsymbol{N}_i$ and sub-right-hand-side vectors $\boldsymbol{b}_i$

$$\begin{aligned} \boldsymbol{N} &= \boldsymbol{A}^T\boldsymbol{P}\boldsymbol{A} = \sum_{i=1}^{n} \boldsymbol{A}_i^T\boldsymbol{P}_i\boldsymbol{A}_i = \sum_{i=1}^{n} \boldsymbol{N}_i \\ \boldsymbol{b} &= \boldsymbol{A}^T\boldsymbol{P}\boldsymbol{y} = \sum_{i=1}^{n} \boldsymbol{A}_i^T\boldsymbol{P}_i\boldsymbol{y}_i = \sum_{i=1}^{n} \boldsymbol{b}_i \end{aligned} \tag{2-22}$$

By doing so, it is not necessary to save the entire design matrix data every time. Instead, only a portion of it needs to be saved while maintaining the same level of precision as before. It should be noted that this chapter provides a general overview of the least-squares method. For further information on multi-type observations with varying weights, please refer to chapter 2.5.

2.4 Parameter pre-elimination

When there are numerous model parameters involved in orbit determination, such as epoch-wise clock offsets, parameter pre-elimination is an effective technique (Jäggi, 2007, p. 38).

Assume that the unknown parameter vector $\boldsymbol{x}$ consists of global parameters $\boldsymbol{x}_1$ and epoch-wise parameters $\boldsymbol{x}_2$

$$\boldsymbol{x} = \begin{pmatrix} \boldsymbol{x}_1 \\ \boldsymbol{x}_2 \end{pmatrix} \tag{2-23}$$

The system of normal equation can thus be written as

$$\begin{bmatrix} \boldsymbol{N}_{11} & \boldsymbol{N}_{12} \\ \boldsymbol{N}_{21} & \boldsymbol{N}_{22} \end{bmatrix} \begin{bmatrix} \boldsymbol{x}_1 \\ \boldsymbol{x}_2 \end{bmatrix} = \begin{bmatrix} \boldsymbol{b}_1 \\ \boldsymbol{b}_2 \end{bmatrix} \tag{2-24}$$

Assume that the actual values of the solution sub-vector $\boldsymbol{x}_2$ is not interested and $\boldsymbol{N}_{22}^{-1}$ exists, one can substitute $\boldsymbol{x}_2$ in the equation (2-24) with

$$\boldsymbol{x}_2 = \boldsymbol{N}_{22}^{-1}(\boldsymbol{b}_2 - \boldsymbol{N}_{21}\boldsymbol{x}_1) \tag{2-25}$$

and get

$$\boldsymbol{N}_{11}^{*}\boldsymbol{x}_1 = \boldsymbol{b}_1^{*} \tag{2-26}$$

with

$$\begin{aligned} \boldsymbol{N}_{11}^{*} &= \boldsymbol{N}_{11} - \boldsymbol{N}_{12}\boldsymbol{N}_{22}^{-1}\boldsymbol{N}_{21} \\ \boldsymbol{b}_1^{*} &= \boldsymbol{b}_1 - \boldsymbol{N}_{12}\boldsymbol{N}_{22}^{-1}\boldsymbol{b}_2 \end{aligned} \tag{2-27}$$

In this way, although the estimates of pre-eliminated parameters $\boldsymbol{x}_2$ are no longer available, they are still accurately considered in the new normal equation system. If one is interested in obtaining values for $\boldsymbol{x}_2$ and has only used the pre-elimination step to reduce the size of the normal equation system, a back-substitution step can be taken after solving equation (2-26). This will allow for solving $\boldsymbol{x}_2$ according to equation (2-25) (Jäggi, 2007, pp. 38-39; Weinbach, 2013, pp. 55-57).

It is important to note that the parameter pre-elimination step cannot be executed at any random time. It can only be performed when further observations no longer have a direct impact on the elements associated with parameters $\boldsymbol{x}_2$. This condition must be met before executing the pre-elimination step (Jäggi, 2007, p. 39).

2.5 Variance component estimation

With the emergence of new technologies like ISL, satellite orbit determination will involve multiple types of observations. However, combining these data for satellite orbit determination requires careful attention due to their varying characteristics and accuracies. Incorrect weighting of each type can negatively impact the accuracy of determined orbits. To determine appropriate weights for combined data, variance component estimation (VCE) is commonly used (Koch & Kusche, 2002). Unlike weight determination based on minimizing measurement residuals, VCE efficiently weighs different observation types based on their contribution (Feng et al., 2020).

Chapter 2.3 has already discussed the least-squares technique. For a problem with *n* observation types, equation (2-19) is re-written here as

$$\begin{gathered} \boldsymbol{y}_i = \boldsymbol{A}_i \Delta \boldsymbol{x}_0 + \boldsymbol{\varepsilon}_i \\ E(\boldsymbol{\varepsilon}_i) = 0, \;\; \boldsymbol{C}(\boldsymbol{\varepsilon}_i) = \sigma_i^2 \boldsymbol{P}_i^{-1} \end{gathered} \tag{2-28}$$

with E and $\boldsymbol{C}$ denote the expectation and covariance matrix of the error, respectively. $\boldsymbol{P}$ is the weight matrix of the observations. The subscript *i* denotes the *i*-th observation type. Other notations are the same as in chapter 2.3. For multi types of observations, the correction to the unknown parameters can still be written as

$$\Delta \boldsymbol{x}_0^{lsq} = \boldsymbol{N}^{-1} \boldsymbol{b} \tag{2-29}$$

here with

$$\begin{aligned} \boldsymbol{N} &= \boldsymbol{A}^T \boldsymbol{C}^{-1} \boldsymbol{A} = \sum_{i=1}^{k} \boldsymbol{A}_i^T \boldsymbol{C}_i^{-1} \boldsymbol{A}_i = \sum_{i=1}^{k} \frac{1}{\sigma_i^2} \boldsymbol{A}_i^T \boldsymbol{P}_i \boldsymbol{A}_i \\ \boldsymbol{b} &= \boldsymbol{A}^T \boldsymbol{C}^{-1} \boldsymbol{y} = \sum_{i=1}^{k} \boldsymbol{A}_i^T \boldsymbol{C}_i^{-1} \boldsymbol{y}_i = \sum_{i=1}^{k} \frac{1}{\sigma_i^2} \boldsymbol{A}_i^T \boldsymbol{P}_i \boldsymbol{y}_i \end{aligned} \tag{2-30}$$

where *k* is the number of different observation types.

The Helmert method is used to iteratively estimate the unknown variance components. Koch and Kusche (2002) proposed a widely recognized approximate estimator, which can be expressed as

$$\hat{\sigma}_i^2 = \frac{\hat{\boldsymbol{\varepsilon}}_i^T \boldsymbol{P}_i \hat{\boldsymbol{\varepsilon}}_i}{r_i} \tag{2-31}$$

with

$$\begin{aligned} \hat{\boldsymbol{\varepsilon}}_i &= \boldsymbol{y}_i - \boldsymbol{A}_i \Delta \boldsymbol{x}_0^{lsq} \\ r_i &= n_i - tr(\boldsymbol{N}_i \boldsymbol{N}^{-1}) \end{aligned} \tag{2-32}$$

where $\hat{\boldsymbol{\varepsilon}}_i$ denotes the vectors of residuals. r_i is the contribution of the *i*-th observation type to the overall degree of freedom of the model. n_i is the number of *i*-th type of observations. The $tr()$ function represents the trace of the matrix.

If the number of observations is significantly greater than the number of unknown parameters, which is usually the case in most applications, it may be feasible to omit the trace part for r_i in equation (2-32) due to computational burden. This results in a simplified VCE as (Yang et al., 2005; Feng et al., 2020)

$$\hat{\sigma}_i^2 = \frac{\hat{\boldsymbol{\varepsilon}}_i^T \boldsymbol{P}_i \hat{\boldsymbol{\varepsilon}}_i}{n_i} \tag{2-33}$$

2.6 Observation models

To determine the orbit of a satellite, measurements related to its position and velocity are required. These measurements are collected by a system that measures electromagnetic wave propagation between the transmitter and receiver. In the late 1950s, Minitrack was installed as a ground-based tracking system for Vanguard satellites. This radio interferometry-based system provided only one set of angle observations but helped investigate Earth's pear-shape and orbit evolution over several years (Montenbruck & Gill, 2000, p. 193; Tapley et al., 2004, pp. 93-94). Nowadays, various types of observations such as range, range rate, azimuth and elevation angles, laser ranging and GNSS measurements support orbit determination in different applications. In the following, the observation models used in this work, namely the ground range (or pseudorange) and the ISL range, are presented in detail.

2.6.1 Ground range model

Range measurement is a frequently used type in orbit determination that calculates the distance between an Earth-based instrument and a satellite (Tapley et al., 2004, p. 94). Assume that satellite *s* transmits the signal at time T^s in the time system of the satellite clock. The receiver *r* records the signal at time T_r in the time system of the receiver clock. The measurement is defined as

$$P_r^s = c(T_r - T^s) \tag{2-34}$$

where *c* is the speed of light. The time difference $T_r - T^s$ corresponds to the signal travel time from the satellite to receiver. However, due to the lack of synchronization between the receiver and transmitter clocks, there are clock errors. Thus, P_r^s is called pseudorange instead of range. Besides, equation (2-34) is only a simplified model that does not consider many other effects such as atmospheric delays, biases and measurement errors. An improved model can be written

as

$$P_r^s = \rho_r^s + c\delta t_r - c\delta t^s + \delta\rho_{r,trp}^s + \delta\rho_{r,ion}^s + b_r + b^s + \varepsilon_r^s \tag{2-35}$$

where ρ_r^s denotes the distance between the satellite and the receiver. δt_r and δt^s denote the clock corrections of receiver and satellite with respect to a common time frame, respectively. $\delta\rho_{r,trp}^s$ and $\delta\rho_{r,ion}^s$ denote the signal delay due to troposphere and ionosphere, respectively. b_r and b^s denote the receiver bias and satellite bias, respectively. ε_r^s is the measurement error including multipath and other systematic errors (Jäggi, 2007, pp. 30-31).

The above observation model pertains to one-way measurements. However, in certain scenarios, a two-way range may be established. One significant benefit of this type of measurement is the elimination of clock offsets. A two-way measurement involves both an uplink and a downlink. The measurement model for these links can be expressed as follows

$$\begin{aligned} P_r^s &= \rho_r^s + c\delta t_r - c\delta t^s + \delta\rho_{r,trp}^s + \delta\rho_{r,ion}^s + b_r + b^s + \varepsilon_r^s \\ P_s^r &= \rho_s^r + c\delta t^s - c\delta t_r + \delta\rho_{s,trp}^r + \delta\rho_{s,ion}^r + b^s + b_r + \varepsilon_s^r \end{aligned} \tag{2-36}$$

where P_r^s denotes the link from satellite to receiver, while P_s^r denotes the link from receiver to satellite. Other notations can be deduced similar like this. These two links are formed almost at the same time but still with small differences. In order to form the two-way link model, both links need to transform to a common epoch. The observation model can then be written as

$$\tilde{P}_r^s = \frac{\rho_r^s + \rho_s^r}{2} + \frac{\delta\rho_{r,trp}^s + \delta\rho_{s,trp}^r}{2} + \frac{\delta\rho_{r,ion}^s + \delta\rho_{s,ion}^r}{2} + b_r + b^s + \tilde{\varepsilon}_r^s \tag{2-37}$$

where $\tilde{P}_r^s$ denotes the two-way observation model and $\tilde{\varepsilon}_r^s$ denotes its measurement error (Tapley et al., 2004, pp. 103-107; Li et al., 2019b).

Most of the LEO satellites in communication constellations are capable of transferring data through both uplink and downlink. Additionally, BDS-3 has a dual one-way link to a ground anchor station in practice. Xie et al. (2020) explains that an anchor station functions as a virtual satellite on the ground and transmits signals similar to those transmitted by actual satellites. As such, it is possible to establish a two-way link between the anchor station and the satellite, much like a two-way ISL. This work will adopt this concept and utilize two-way links between ground stations and satellites.

2.6.2 ISL range model

The ISL range observation model follows the same principle as other range observations, with the only difference being that both transmitter and receiver are located on satellites. The observation equation can be expressed as

$$P^{AB} = \rho^{AB} + c\delta t^B - c\delta t^A + b^A + b^B + \varepsilon^{AB} \tag{2-38}$$

where P^{AB} is the range measured from transmitter satellite *A* to the receiver satellite *B*. ρ^{AB} denotes the signal propagation distance. δt^A and δt^B are the clock offsets of the satellite *A* and *B*, respectively. b^A and b^B represent their biases. ε^{AB} is the measurement error including ionospheric effects.

In most research studies, ISL typically functions as a two-way or dual one-way link (Tang et al., 2018; Li et al., 2019b; Schlicht et al., 2020; Marz et al., 2021; Michalak et al., 2021; Zhang et al., 2021). This means that each satellite serves both as a transmitter and receiver. Similar to the two-way ground range measurement, the two-way ISL can also eliminate clock offsets by transforming observation equations of uplink and downlink to a common epoch

$$\tilde{P}^{AB} = \frac{\rho^{AB} + \rho^{BA}}{2} + b^A + b^B + \tilde{\varepsilon}^{AB} \tag{2-39}$$

where $\tilde{P}^{AB}$ is the two-way ISL observation model. ρ^{AB} and ρ^{BA} represent the propagation distance that the signal travels from satellite A to B and from B to A, respectively. $\tilde{\varepsilon}^{AB}$ s the measurement error. This work will utilize the two-way ISL range model, similar to the ground range model and other related studies.

2.6.3 Measurement errors

Signals transmitted to or from ground stations require transmission through Earth's atmosphere. However, the interaction between electromagnetic radiation and atmospheric atoms, ions, electrons, and molecules can cause various effects on the signals such as refractive bending and changes in velocity. In particular, the troposphere and ionosphere are the most affected layers (Montenbruck & Gill, 2000, p. 219; Tapley et al., 2004, p. 110).

The troposphere contains neutral gas that causes a delay in signals, known as tropospheric delay. This delay has two components: a dry part and a wet part

$$\delta\rho_{trp} = \delta\rho_{dry} + \delta\rho_{wet} \tag{2-40}$$

where $\delta\rho_{trp}$ denotes the tropospheric delay. $\delta\rho_{dry}$ and $\delta\rho_{wet}$ denote the dry part and wet part of the tropospheric delay, respectively. The dry part accounts for approximately 90% of the total delay and assumes that the atmosphere behaves in accordance with the ideal gas law and hydrostatic equilibrium. This component can be easily modeled using surface pressure measurements. In contrast, the wet part contributes a maximum of 40 cm to the total delay and is challenging to model due to rapid fluctuations in water vapor and atmospheric water content (Tapley et al., 2004, pp. 111-112).

There are various techniques available for modeling the tropospheric delay, which is determined by the length of the satellite's propagation path through the atmosphere and therefore varies with its zenith angle z. One commonly used formula for calculating this delay is

$$\delta\rho_{trp}(z) = m_{dry}(z) \cdot \delta\rho^0_{dry} + m_{wet}(z) \cdot \delta\rho^0_{wet} \tag{2-41}$$

where $m_{dry}(z)$ and $m_{wet}(z)$ denote the mapping function with zenith angle dependency for dry part and wet part, respectively. $\delta\rho^0_{dry}$ and $\delta\rho^0_{wet}$ represent the zenith delay of two parts. Several researchers have developed various mapping functions, which are typically computed using a continued fraction form. For example, the MIT Thermospheric mapping function (MTT)

$$m(z) = \frac{1 + \dfrac{a}{1 + \dfrac{b}{1 + c}}}{\cos z + \dfrac{a}{\cos z + \dfrac{b}{\cos z + c}}} \tag{2-42}$$

where the coefficients *a*, *b*, *c* differ for the dry and wet mapping functions. For a precise model, these coefficients vary based on the location and time (Herring, 1992; Tapley et al., 2004, pp. 112-114).

Boehm et al. (2006b) proposed the Vienna Mapping Function 1 (VMF1), which involves calculating coefficients through ray tracing in atmospheric layers of a weather model. These coefficients are regularly updated on the data server (re3data.org, 2021). A simplified version of VMF1 was developed by Boehm et al. (2006a) called the Global Mapping Function (GMF). Unlike VMF1, GMF is an empirical mapping function that does not require any weather model data.

The ionosphere is the upper part of the atmosphere that is characterized by the presence of ions and free electrons. While it does not affect optical signals, it can cause delays in radio signals depending on their frequency. The ionospheric delay can be written as

$$\delta\rho_{ion} = \alpha \frac{E}{f^2} \tag{2-43}$$

where *E* denotes the integrated total electron content (TEC)

$$E = \int_L N_e(s)\, ds \tag{2-44}$$

Here, N_e is the density of free electrons (per m^3). α in equation (2-43) is a constant $\alpha = 40.3 \times 10^{16}$ $ms^{-2}TECU^{-1}$. TECU is the TEC units that $1\ TECU = 10^{16}$ free electrons per m^2. f is the signal frequency. For range observations, ionosphere delays the signal and $\delta\rho_{ion}$ is positive. Whereas for phase observations, ionosphere shortens the distance and $\delta\rho_{ion}$ gets a negative value (Tapley et al., 2004, pp. 114-115).

The TEC can be obtained by an ionospheric mapping function and vertical TEC (VTEC)

$$E(z) = m_I(z) \cdot E_V \tag{2-45}$$

where $m_I(z)$ denotes the mapping function with zenith angle dependency. E_V denotes VTEC. Currently, there are complicated mapping functions in use that take the vertical electron distribution into account.

In GNSS analysis, the ionosphere-free linear combination is commonly utilized to eliminate ionospheric delays during data processing (Jäggi, 2007, pp. 34-35). This approach is also employed in this study.

It should be noted that biases in both the transmitter and receiver of the ground station and satellite can cause signal delays. For simplicity's sake, these biases are assumed to remain constant throughout this work.

2.7 Force models

Satellites experience various perturbations, which can be categorized as either gravitational forces (such as geopotential, Sun and Moon attractions, tides) or non-gravitational forces (like air drag, radiation pressure, albedo). These perturbations cause deviations from the Keplerian orbit. The equation of motion for a perturbed orbit can be expressed as follows

$$\ddot{\boldsymbol{r}} = \boldsymbol{f}_0 + \boldsymbol{f}_1(\boldsymbol{r}, \dot{\boldsymbol{r}}, t) = -GM\frac{\boldsymbol{r}}{r^3} + \boldsymbol{f}_1(\boldsymbol{r}, \dot{\boldsymbol{r}}, t) \tag{2-46}$$

where $\boldsymbol{r}$, $\dot{\boldsymbol{r}}$ and $\ddot{\boldsymbol{r}}$ denote the position, velocity and acceleration of a satellite in a non-rotating geocentric coordinate system at epoch *t*, respectively. $\boldsymbol{f}_0$ is the Keplerian term, namely the unperturbed motion. *G* is the gravitational constant and *M* is the mass of the central body, or Earth. $\boldsymbol{f}_1$ represents the perturbing accelerations.

Gravitational perturbations are typically well modeled and applied accurately in orbit determination. This chapter will not delve into the details of gravitational perturbations. For more information on this topic, please refer to Montenbruck and Gill (2000), Tapley et al. (2004) and Beutler (2005a).

Atmospheric force is the largest non-gravitational force that affects LEO satellites. The dominant atmospheric force at play is drag. There are also minor forces such as lift and binormal forces, but they can safely be disregarded in most cases. However, modeling air drag poses a significant challenge due to various factors. Firstly, it relies on the physical properties of the upper atmosphere, which are not well understood and change rapidly. Secondly, air drag also depends on the detailed knowledge of how neutral gas and charged particles interact with the satellite's surface, size, shape and orientation. The satellite acceleration caused by air drag can be expressed as

$$\ddot{\boldsymbol{r}} = -\frac{1}{2}C_D\frac{A}{M}\rho v_r^2\boldsymbol{e}_v \tag{2-47}$$

where C_D is the drag coefficient. It is a dimensionless quantity that describes the interaction of the atmosphere with the surface of the satellite. Typical range of the drag coefficient is around 1.5-3.0. A is the satellite's cross-sectional area and M is the mass of the satellite. ρ denotes the atmospheric density at the location of the satellite. v_r denotes the relative velocity of the satellite, while $\boldsymbol{e}_v = \frac{\boldsymbol{v}_r}{v_r}$ is its unit vector. The direction of the drag acceleration is thus always anti-parallel to the relative velocity vector (Montenbruck & Gill, 2000, pp. 83-86; Beutler, 2005a, pp. 175-176).

Air drag modeling primarily relies on the atmospheric density, which is a complex parameter to model. The upper atmosphere's density depends on various factors such as height, temperature, solar radiation, energetic particles, hydrogen density variations and pressure waves. Currently available atmosphere models range from simple solutions based on heat diffusion equations with solar heating under quasi-hydrostatic equilibrium assumptions (e.g., Harris-Priester model) to more advanced ones like the drag temperature model (DTM). DTM

uses accelerometer measurements from satellites such as Challenging Minisatellite Payload (CHAMP) and GRACE for improved accuracy in modeling atmospheric density (Montenbruck & Gill, 2000, pp. 86-102).

Solar radiation pressure (SRP), on the other hand, is significant for satellites positioned above 2000 km from the Earth's surface (Beutler, 2005a, p. 173). It encompasses all surface forces exerted on a satellite due to incident or emitted radiation. The force comprises absorbed and reflected parts of the incident radiation along with a small scattered portion. In case of an absorbing surface, this force can be expressed as

$$\boldsymbol{F}_{\alpha} = -\alpha \frac{S}{c} A \cos\theta \cdot \boldsymbol{s} \tag{2-48}$$

where α is the absorption coefficient. S is the solar radiation flux and c denotes the speed of light. θ is the incidence angle of the incoming radiation with respect to the unit normal vector $\boldsymbol{n}$ of the surface A. $\boldsymbol{s}$ denotes the unit vector to the Sun. Therefore, $\cos\theta = \boldsymbol{n} \cdot \boldsymbol{s}$. S Likewise, the force exerted by reflected photons can be obtained

$$\boldsymbol{F}_{\rho} = -\rho \frac{S}{c} 2A \cos^2\theta \cdot \boldsymbol{n} \tag{2-49}$$

and for the diffusely scattered photons

$$\boldsymbol{F}_{\delta} = -\delta \frac{S}{c} A \cos\theta \cdot \left(\boldsymbol{s} + \frac{2}{3}\boldsymbol{n}\right) \tag{2-50}$$

Where ρ and δ denote the reflection coefficient and scatter coefficient, respectively. Then, these coefficients should obey $\alpha + \rho + \delta = 1$ (Montenbruck & Gill, 2000, pp. 77-79).

The cannon-ball model is the simplest satellite model for radiation pressure. It is utilized when certain parameters of the satellite are unknown, such as optical surface properties, geometrical parameters or attitude. However, for high precision applications, a more intricate box-wing model is preferred. This advanced model breaks down the structure of a satellite into several surfaces with known geometrical and optical parameters along with orientation (Montenbruck & Gill, 2000, p. 79).

2.8 Empirical accelerations and constraints

2.8.1 Colombo model

In practice, force models cannot be as precise as reality due to the complexity of the nature, computational burden, and lack of precise knowledge about certain parameters. Additionally, unmodeled forces may also contribute to an imperfect model. In particular, the imperfect non-conservative force models have significant limitations in achieving high precision orbits. In addition to continuously improving force models, many researchers introduce empirical accelerations to compensate for these small force errors. One example is the Colombo model proposed by Colombo (1989). Since most of the mismodeling occurs at one-cycle-per-

revolution (1-CPR) frequency (Montenbruck & Gill, 2000, p. 112), the equation of the Colombo model can be written as (Rodriguez-Solano et al., 2012)

$$\begin{aligned} \boldsymbol{a}_R(u) &= \boldsymbol{a}_{R0} + \boldsymbol{a}_{RC}\cos u + \boldsymbol{a}_{RS}\sin u \\ \boldsymbol{a}_S(u) &= \boldsymbol{a}_{S0} + \boldsymbol{a}_{SC}\cos u + \boldsymbol{a}_{SS}\sin u \\ \boldsymbol{a}_W(u) &= \boldsymbol{a}_{W0} + \boldsymbol{a}_{WC}\cos u + \boldsymbol{a}_{WS}\sin u \end{aligned} \tag{2-51}$$

where R, S and W denote radial, along-track and cross-track of the satellite, respectively. u is the true anomaly of the satellite. $\boldsymbol{a}_{R0}$ denotes the constant acceleration term in radial direction, while $\boldsymbol{a}_{RC}$ and $\boldsymbol{a}_{RS}$ denotes the periodical coefficients in radial direction. Other parameters can be defined based on similarities with existing ones.

It is important to exercise caution when applying empirical parameters, as introducing additional ones can weaken the solution for non-empirical parameters and may significantly reduce orbit accuracy. Nevertheless, it may be necessary to solve for empirical parameters in order to address deficiencies in dynamic models. Empirical parameters have been effectively used to mitigate force model errors of GPS satellites (Montenbruck & Gill, 2000, p. 112; Jäggi, 2007, pp. 47-48).

2.8.2 Piece-wise constant accelerations

Piece-wise acceleration is another method used to address modeling deficiencies in satellite dynamics. This involves dividing empirical accelerations into smaller pieces. It is assumed that the empirical accelerations can be expressed as

$$\boldsymbol{a}(t) = \boldsymbol{a}_R(t) + \boldsymbol{a}_S(t) + \boldsymbol{a}_W(t) \tag{2-52}$$

Namely the sum of accelerations in each direction in the satellite body-fixed frame. The acceleration in each direction $\boldsymbol{a}_d$, where $d \in \{R, S, W\}$, can be represented by m constant pieces, which are activated only within predefined time intervals $[t_{i-1}, t_i]$

$$\boldsymbol{a}_d(t) = \boldsymbol{a}_{0,d}(t) + \sum_{i=1}^{m} \boldsymbol{a}_{i,d}(t) \cdot \xi(t, t_{i-1}, t_i) \tag{2-53}$$

where

$$\xi(t, t_{i-1}, t_i) = \begin{cases} 1, & t_{i-1} \le t \le t_i \\ 0, & \text{otherwise} \end{cases} \tag{2-54}$$

In total there are $3(m+1)$ parameters that need to be estimated together with other unknown parameters (Beutler et al., 2006; Jäggi, 2007, pp. 48-51).

2.8.3 Absolute constraining

When the observability of a parameter is weak, constraints are often used to stabilize the solution. For example, the parameter interval may be too small to allow a reliable estimation. Thus, it is often used with pseudo-stochastic orbit parameters such as piece-wise constant accelerations, in order to attenuate the risk of over-parameterization with small pieces. Typically,

the selected model parameters are constrained either to their a priori values (so-called absolute constraining) or to other parameters (so-called relative constraining) (Beutler et al., 2006; Jäggi, 2007, p. 39; Weinbach, 2013, p. 57). In the following, absolute constraining is introduced. Information about relative constraining can be found in Jäggi (2007).

Define a user-specified variance value σ_{abs}^2, one can virtually adding an observation

$$0 = \Delta x_i + \varepsilon \tag{2-55}$$

with

$$E(\varepsilon) = 0, \;\; C(\varepsilon) = \sigma_{abs}^2 \tag{2-56}$$

to the design matrix. And it can be deduced to simply adding the value $\frac{\sigma_0^2}{\sigma_{abs}^2}$ to the main diagonal element of the normal equation matrix referring to the parameter Δx_i

$$\widetilde{N}_{i,i} = N_{i,i} + \frac{\sigma_0^2}{\sigma_{abs}^2} \tag{2-57}$$

By applying absolute constraining, the degree of freedom of the system also increases by 1 (Jäggi, 2007, p. 39; Weinbach, 2013, p. 57).

3 Constellation design

3.1 Introduction

As mentioned in chapter 1.3, to utilize the LEO satellite constellation for navigation or geodetic applications, it must be configured to meet the minimum requirements for these purposes. Generally speaking, a satellite constellation is a group of satellites that work together to provide the same functionality. The purpose of building such a system instead of using one or two single satellites is to achieve global coverage. Researchers have been working on designing an optimal constellation since the 1960s with the aim of reducing the number of required satellites while still achieving specific goals.

Luders (1961), Ullock and Schoen (1963), Lueders and Ginsberg (1974) developed the Streets of Coverage (SOC) method to ensure uninterrupted coverage for latitudinally bounded areas of the world. This approach involves placing satellites at the same altitude, with each "street" or orbital plane having an equal distribution of satellites based on coverage needs, as shown in Fig. 3-1. The number of "streets" required can also be determined through calculation.

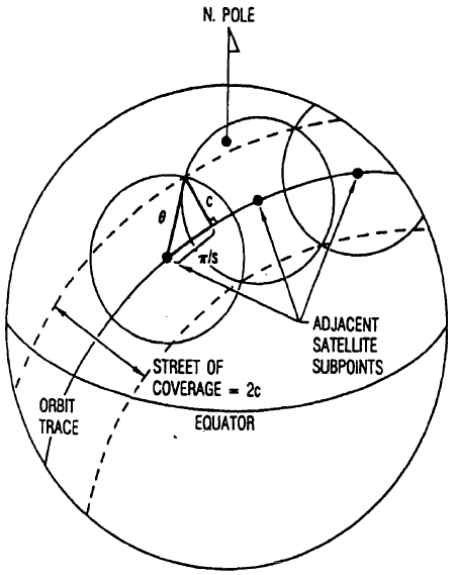

Fig. 3-1 One orbital plane in SOC constellation (Lang & Adams, 1998)

In the 1970s, Walker proposed two widely used methods for designing satellite constellations: the Walker Delta and the Walker Star (Walker, 1970, 1977, 1982). The main difference between these methods is how they distribute orbital planes. "*The star pattern is typified by multiple orbits, sharing a common pair of nodes in the reference plane, and with equal (or approximately equal) relative inclinations of adjacent co-rotating orbits; the delta*

pattern is typified by orbits of equal inclination to, and with nodes equally spaced around, the reference plane" (Walker, 1970). To put it simply, Walker Delta constellation's orbits are evenly distributed along a complete circle while those of Walker Star constellation are deployed along a semi-circle. For more intuitive understanding refer to Fig. 3-2 and Fig. 3-3.

A Walker constellation consists of satellites that are positioned at the same orbital height and inclination. The identification of a Walker constellation is based on its $t/p/f$ values, where t represents the total number of satellites, p denotes the number of evenly divided orbital planes, and f indicates the relative phasing of satellites in neighboring orbital planes. Satellites within each orbital plane are equally spaced apart. In a Walker Delta constellation, f can only be an integer from 0 to $p-1$; whereas in a Walker Star constellation, it can be any number less than p. The phasing angle between two satellites in the adjacent orbital planes can be calculated using $\frac{360°}{t} \times f$, where $\frac{360°}{t}$ is known as a pattern unit. Examples of these constellations include Iridium's 66/6/2 for Walker Star and Galileo's 24/3/1 for Walker Delta.

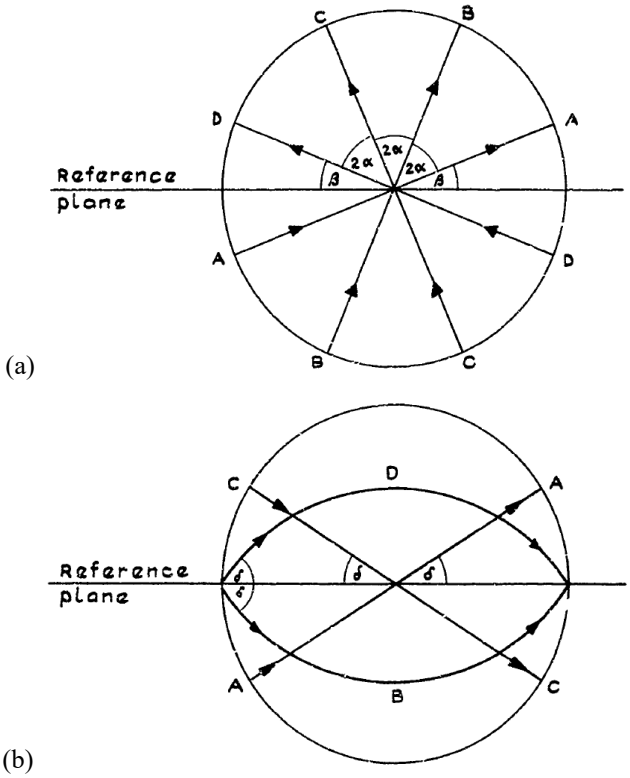

Fig. 3-2 Two types of Walker constellation with 4 orbital planes: (a) Walker Star, (b) Walker Delta (Walker, 1970)

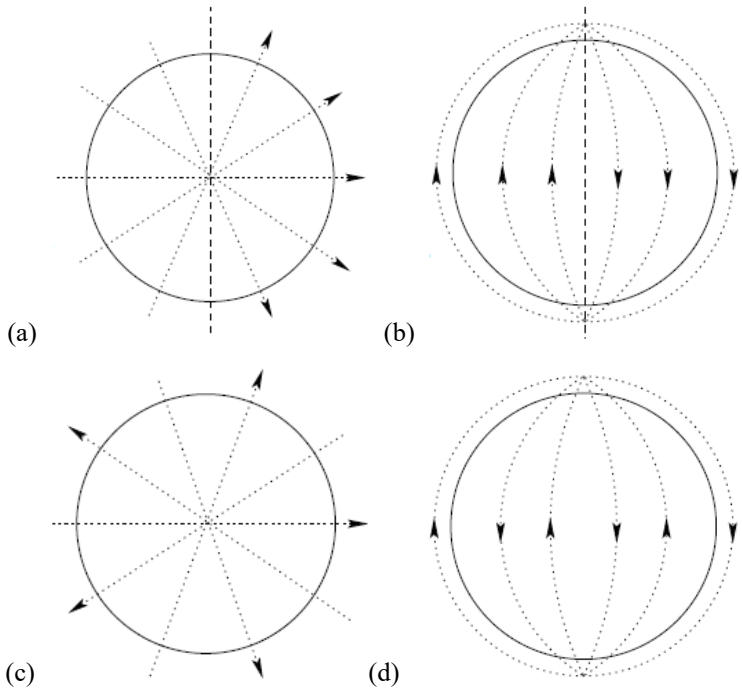

Fig. 3-3 Two types of Walker constellation: (a) Walker Star viewed from north pole, (b) Walker Star viewed from equator, (c) Walker Delta viewed from north pole, (d) Walker Delta viewed from equator (Ferreira et al., 2002)

In addition to the aforementioned types of constellations, there exist other less commonly used types. One such type is the Draim constellation, which employs eccentric orbits with a common period and inclination (Draim, 1985, 1991; Lang & Adams, 1998). Another type is the Flower constellation proposed by Mortari et al. (2004), where all satellites have the same repeating ground tracks. Building upon this concept, Avendaño et al. (2013) and Davis et al. (2013) created both two-dimensional and three-dimensional Lattice Flower constellations respectively. Additionally, Wu and Wu (2008) conducted research on designing an orthogonal circular orbit satellite constellation.

With these classic and new constellation types, the process of designing a constellation based on its intended applications can be simplified. However, selecting the appropriate type of constellation and determining its parameters still requires expertise. Further research is being conducted to explore optimal constellation designs for specific tasks.

Several publications have utilized the genetic algorithm. For instance, Multi Objective Genetic Algorithm (MOGA) has been used to design constellations for various purposes such as zonal coverage (Ely et al., 1999), global coverage with satellites in MEO or LEO (Asvial et al., 2002), continuous mutual regional coverage (Bekhti et al., 2016), and global communication (Liu et al., 2017). Hoskins et al. (2017) employed a stochastic programming approach to design a constellation of five satellites for forest fire monitoring, while Nag et al. (2016) designed a Walker constellation consisting of sixteen CubeSats that can continuously monitor the air traffic in Alaska. Additionally, Capez et al. (2022) discussed using both the Walker pattern and Flower pattern to design a sparse satellite constellation suitable for direct-

to-satellite Internet of Things (IoT) applications. The concept behind GPS and Galileo constellation design is also discussed by some researchers (Massatt & Zeitzew, 1998; Mozo-García et al., 2001; Píriz et al., 2005).

Due to the current rapid development of LEO satellites, design work on this type of constellation is also attracting attention. Kimura et al. (1995) discussed the structure and ISL design for a double-layered LEO satellite constellation for communication, providing basic perspectives on selecting satellite altitude and number. Lang (1996) designed a LEO Walker constellation to cover the mid-latitude areas continuously with 1/3 fewer satellites than needed for global coverage, as most people live in this range. Yang et al. (2016) proposed a hybrid LEO Walker constellation that could enhance navigation while also serving communication needs. They discussed about the criteria for selecting parameters such as altitude and inclination, and simulated a hybrid constellation to show the coverage status. Qu et al. (2017) designed an IoT-focused LEO satellite constellation with around 40 satellites and ISLs, while He and Hugentobler (2018) intended to use a combined LEO Walker constellation for positioning by determining proper satellite heights and inclinations based on the visibility. Zhang et al. (2018) investigated both Walker-type and Flower-type LEO constellations' potential to augment regional navigation, while many other researchers continue studying different methods of designing LEO satellite constellations to augment current GNSS capabilities (Ge et al., 2020b; Guan et al., 2020; Ma et al., 2020; Zhang et al., 2020; Deng et al., 2023).

Although the design of LEO satellite constellations has been extensively discussed in recent years, there are still some aspects that have not been given enough attention. Firstly, while the application for communication or IoT is well-established, navigation applications mostly focus on using LEO satellites as an augmented system to improve current GNSS performance. However, as mentioned in chapter 1.3, designing a LEO satellite constellation that can provide independent service is also appealing but has not received serious consideration yet.

Moreover, popular genetic algorithms require careful selection of decision variables, search ranges and cost functions with their coefficients. For example, Ma et al. (2020) used a fixed orbit height and a cost function focusing on the number of visible satellites and distribution evenness; Guan et al. (2020) also used a fixed orbit height but focused on GDOP and the number of satellites; Zardashti and Emami (2021) used another cost function emphasizing GDOP and the number of satellites as well. Therefore, selecting these parameters and coefficients is crucial since they can lead to different results.

This work aims to approach constellation design from a different perspective in order to optimize its performance for various applications beyond communication or IoT purposes.

3.2 Multi-layer constellation

To utilize LEO mega-constellations for positioning, the first step is to determine the essential requirements for the constellation. This involves defining a constellation that minimizes infrastructure costs while providing global positioning services. Satellite visibility is crucial not

only for positioning but also for communication and various activities. Some of the information presented in this chapter has been adapted from previously published work (He & Hugentobler, 2018). Fig. 3-4 illustrates how orbit height and elevation angle affect satellite visibility radius

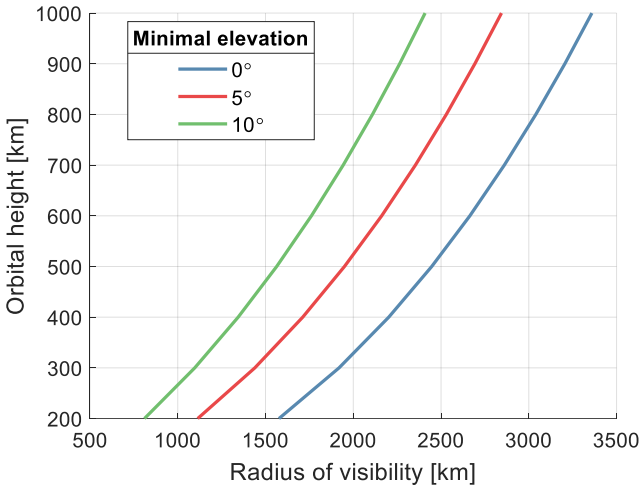

Fig. 3-4 Radius of visibility with respect to the orbital height and elevation angle

As expected, a smaller elevation angle results in a larger radius of visibility for the same orbit height. Additionally, increasing the orbit height also increases visibility. However, achieving an increased visibility radius requires either by decreasing the minimal elevation angle or increasing orbital height, which leads to fewer required satellites but higher launch costs per satellite mass.

According to the GNSS principle, a ground receiver needs signals from at least four satellites (or three if using a two-way link) to determine its position. To provide global service, this minimum number of visible satellites must be available everywhere on Earth. However, due to the convergence of satellite orbits towards northern and southern latitudes, the number of observable satellites varies by latitude. Therefore, constellation design must take this factor into account. Fig. 3-5 illustrates the percentage of the satellite visibility along different latitudes for one revolution and one satellite with varying inclinations. The ordinate represents the likelihood that this satellite will be visible at any time in a given latitude.

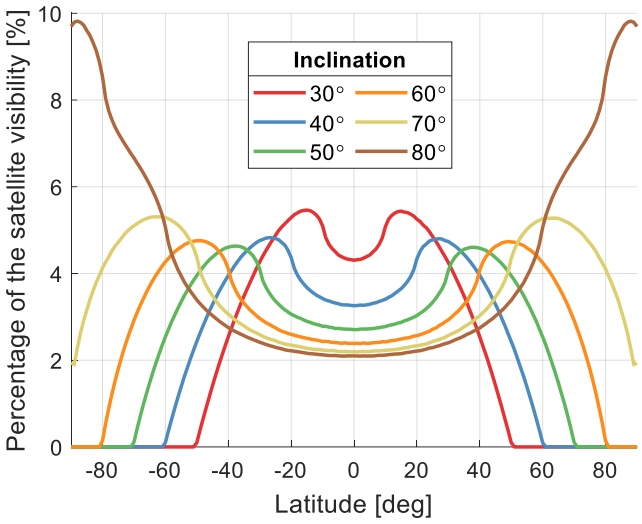

Fig. 3-5 Percentage of the satellite visibility along latitude for orbital height of 900 km, minimal elevation 10°

Fig. 3-5 illustrates that as the inclination increases for a specific orbital height and elevation angle, the satellite visibility decreases near the equator but increases near the latitude corresponding to the inclination. Typically, satellite visibility initially increases with latitude for a given inclination and reaches its maximum value between latitudes $i - \phi$ and i. In this context, i represents the inclination while ϕ refers to the coverage semi-angle - which is calculated as Earth's central angle from the sub-satellite point to the edge of coverage area. Namely

$$\begin{aligned} \phi &= \arcsin \frac{\cos\theta \cdot \left(\sqrt{r^2 - \cos^2\theta \cdot R_E^2} - R_E \cdot \sin\theta\right)}{r} \\ &= \arccos\left(\frac{R_E}{r}\cos\theta\right) - \theta \end{aligned} \tag{3-1}$$

Here, the Earth is assumed to be spherical, and its radius is R_E. $r = R_E + h$ denotes the radius of the satellite orbit, where h is the orbital height. θ is the minimal elevation angle. For a visual representation of the coverage semi-angle, refer to Fig. 3-6.

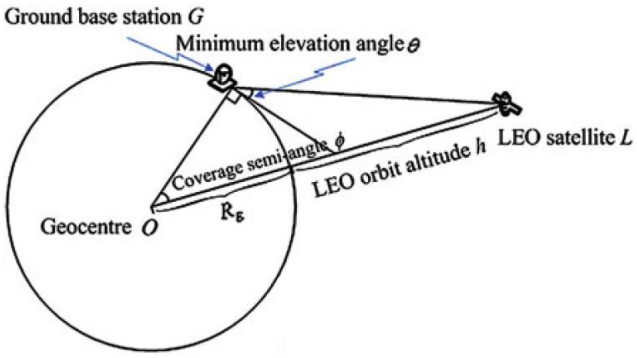

Fig. 3-6 Coverage semi-angle (Long, 2014)

The maximum latitude that the sub-satellite point can reach is the angle of inclination. This means when the satellite reaches the latitude of inclination, the lower edge of the coverage area will be at $i - \phi$ latitude. Meanwhile, the satellite tends to stay longer at higher latitudes, and the covered longitude is larger for the same coverage area due to smaller latitude circles at higher latitude. Therefore, the percentage of satellite visibility tends to be larger, except for inclinations near 80° where visibility continues to increase beyond the latitude of inclination. This is due to the fact that the upper boundary of the coverage area of the satellite $i + \phi$ exceeds 90°. As a result, when passing through polar regions, satellites can be observed almost all the time leading to an increase in visibility up to the poles.

Similarly, Fig. 3-7 illustrates the percentage of satellite visibility changes with the orbital height. As the height increases, so does the satellite visibility. This pattern is consistent with Fig. 3-5. When the orbital height is below 600 km, the satellite's coverage area does not encompass the entire polar region; its upper boundary angle is only at 88.8°. At a height of 700 km, however, this angle increases to 90.5° and as shown in Fig. 3-7, full coverage of the polar area can be achieved. As orbital height continues to increase beyond this point, so too does satellite coverage and duration of visibility in polar regions, resulting in an overall growth in visibility rather than a decrease.

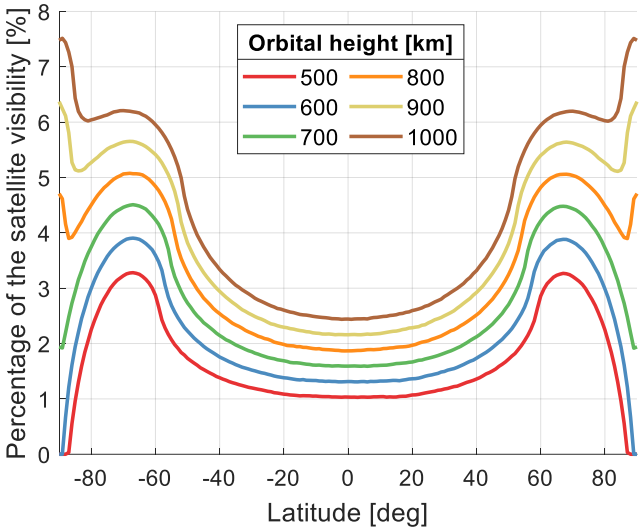

Fig. 3-7 Percentage of the satellite visibility along latitude for inclination of 73°, minimal elevation 10°

Fig. 3-8 presents an alternative perspective, showing the number of visible satellites in a Walker constellation 73°: 189/9/1 at an orbital height of 900 km and above 10° elevation for three ground stations: Kourou near the equator, Wettzell in middle Europe, and Kiruna in northern Europe. The variance in satellite visibility among these stations is evident; there is almost a three-fold difference in visible satellites between them. Notably, more satellites are visible near the polar region than near the equator. Consequently, the distribution of the number of visible satellites is highly inconsistent.

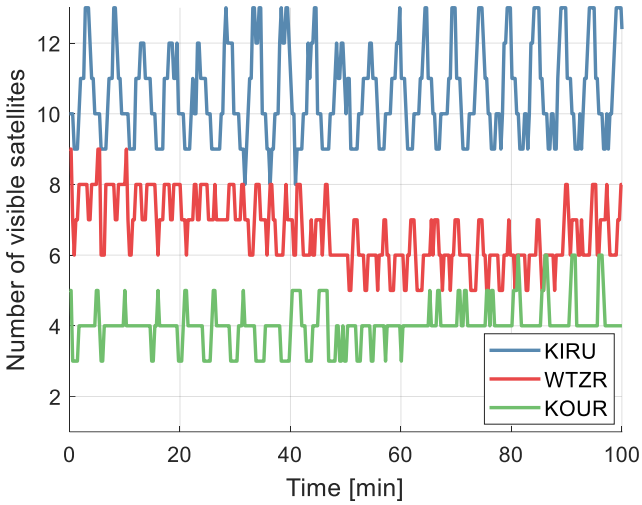

Fig. 3-8 Number of visible satellites as function of time for three stations: orbit height of 900 km, minimum elevation of 10°, Walker constellation of 73°:189/9/1

To achieve a more even distribution of visible satellites worldwide, it is advisable to combine constellations with different inclinations. This approach would enable the constellation with a higher inclination to cover polar regions while the one with lower

inclination could enhance visibility near the equator. An example of such a combination is illustrated in Fig. 3-9, which demonstrates that this multi-layer constellation provides better and more uniform coverage than a single constellation by maintaining visibility at both high and low latitudes simultaneously.

Fig. 3-10 shows the result of combining two constellations as depicted in Fig. 3-8 for comparison purposes. The number of satellites in both figures is almost identical; however, it is evident that combining two constellations with different inclinations significantly improves average visibility on Earth compared to using only one constellation. In general, the number of visible satellites at three stations becomes much closer when using a combined constellation rather than just one, resulting in much more uniform coverage overall.

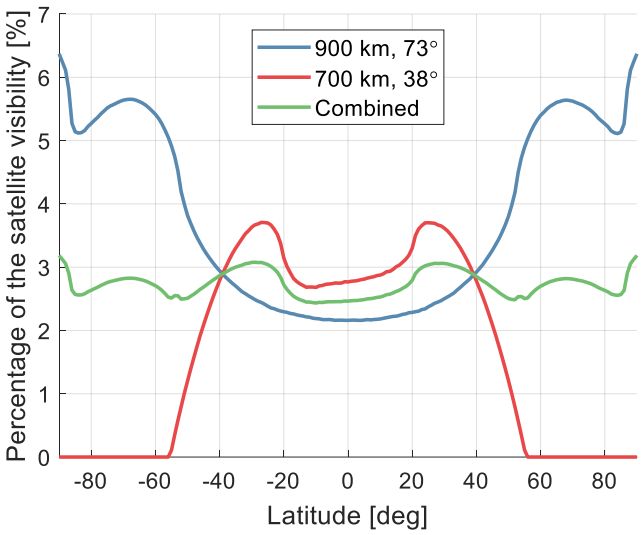

Fig. 3-9 Percentage of the satellite visibility along latitude for multi-layer constellation: orbital height of 900 km, minimum elevation of 10°, inclination of 73°; with orbital height of 700 km, minimum elevation of 10°, inclination of 38°

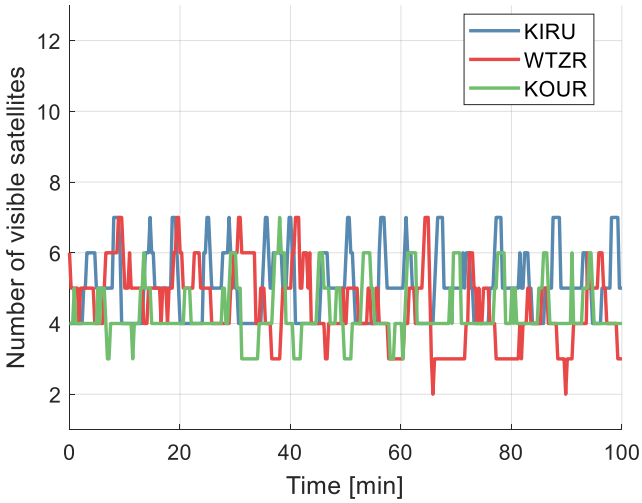

Fig. 3-10 Number of visible satellites as function of time at three stations for multi-layer constellation: orbit height of 900 km, minimum elevation of 10°, Walker constellation of 73°: 90/9/1 and orbit height of 700 km, minimum elevation of 10°, Walker constellation of 38°:91/7/1

Fig. 3-11 (a) displays the average number of visible satellites above 10° elevation for the Walker constellation 73°: 189/9/1 at an altitude of 900 km, as a function of geographic location over one revolution. The distribution is uneven and varies with latitude, ranging from approximately four visible satellites at low latitudes to more than ten at high latitudes.

In contrast, Fig. 3-11 (b) illustrates an example of a combined multi-layer constellation consisting of two Walker constellations that differ in inclination and orbit height. It can be observed that this combined constellation has a more uniform distribution compared to the single constellation solution where visibility mostly accumulates at higher latitudes.

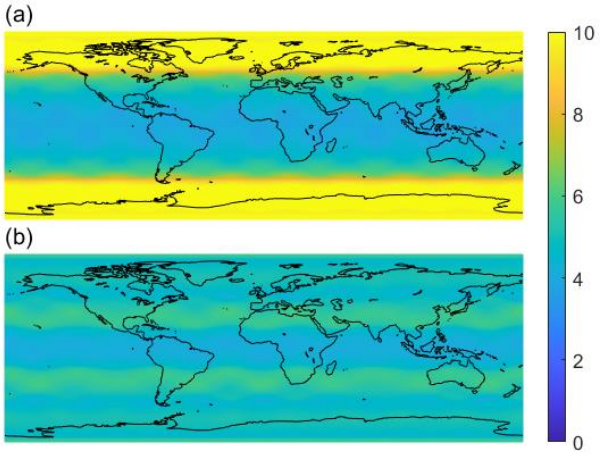

Fig. 3-11 Average number of visible satellites for: (a) orbit height of 900 km, Walker constellation of 73°: 189/9/1; (b) multi-layer constellation of orbit height of 900 km, Walker constellation of 73°: 90/9/1 and orbit height of 700 km, Walker constellation of 38°: 91/7/1. All cases have the minimum elevation of 10°

3.3 Orbit height and inclination

The previous results indicate that utilizing a multi-layer constellation is more efficient and cost-effective. Consequently, the primary objective of constellation design is to identify the most suitable combinations. However, this task can be complex due to the numerous parameters involved. For instance, in a single Walker constellation, variables such as orbit altitude, inclination, total number of satellites, number of orbital planes and spacing angle between neighboring planes must be determined. When combining two constellations, these variables double resulting in an even larger search space.

Fig. 3-12 (a) displays the selection process for the inclination of a combined constellation. The STD of the satellite visibility along latitude is used to determine a globally uniform solution. This figure presents two satellites at altitudes of 900 km and 700 km, respectively, both observed at a minimum elevation angle of 10° with inclinations varying from 0° to 90°. It is evident that combining higher (approximately 65° to 85°) and lower (approximately 30° to 60°)

inclinations results in minimal STD. To cover polar areas, the constellation with higher inclination should have an upper boundary of the coverage area for at least 90°. Thus, if the constellation at an altitude of 700 km has a higher inclination, it should be greater than 72.5°. The optimal combination is achieved with inclinations of 73° (at an altitude of 900 km) and 38° (at an altitude of 700 km).

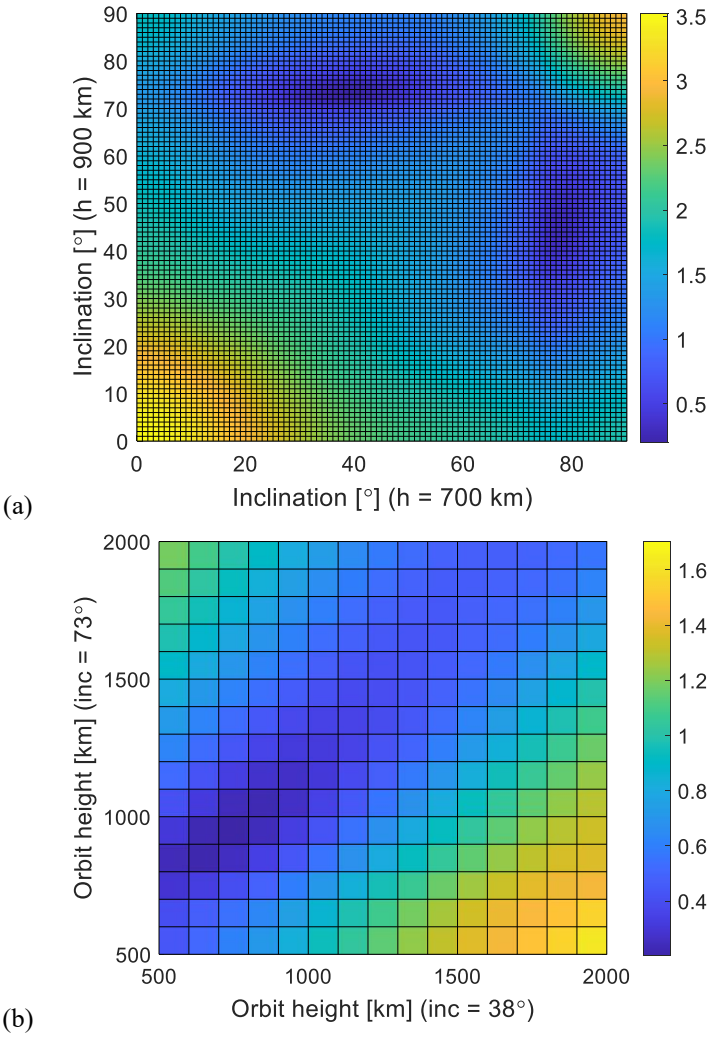

Fig. 3-12 STD of the percentage of satellite visibility along latitude for different combination of: (a) inclination; (b) orbit height

Similarly, Fig. 3-12 (b) illustrates the impact of orbit height on the visibility. Two satellites with inclinations of 73° and 38° are considered, and their orbit heights range from 500 km to 2000 km. The figure indicates that for smaller standard deviation, the constellations' orbit heights should be relatively close to each other. Specifically, the minimum STD was observed at an altitude combination of 900 km (73°) and 700 km (38°).

It is important to note that these initial results only pertain to the discussion of selecting one parameter, either inclination or orbital height. Since they may be correlated and both affect satellite visibility, their joint search process along with other parameters will be discussed in

the following paragraph.

Before the discussion about the selection of multiple parameters, this study also explores the possibility of combining three constellations, in addition to two. Table 3-1 presents some of the best cases with minimum STD. The inclinations are searched from 0° to 90°, with a step size of 1°. The results indicate that for selected orbit heights (700 km, 800 km, and 900 km) and elevation angle (10°), the optimal combination is 82° (at 700 km), 33° (at 800 km), and 63° (at 900 km). However, other factors such as computation burden and costs must also be considered when deciding on a constellation combination. Although combining three constellations yields better results compared to combining two constellations shown in Fig. 3-12 (STD = 0.2025%), with an STD of only 0.1348%, this work will adopt a combination of two constellations due to computational efficiency considerations.

Table 3-1 Best cases of the inclinations of 3 combined sub-constellations with minimum STD of the percentage of satellite visibility. Only part of the best cases with the minimum STD values are listed here

Inclination [°] (900 km)	Inclination [°] (800 km)	Inclination [°] (700 km)	STD [%]
63	33	82	0.1348
63	34	82	0.1349
62	33	82	0.1368
62	33	83	0.1373
62	34	83	0.1388
62	34	82	0.1389
60	80	31	0.1396

The current results do not represent the optimal scenario for all possible combinations due to certain parameters being assumed as fixed. Specifically, the assumption that each sub-constellation has an equal number of satellites can be varied. As a result, more variables can be introduced to determine a more general ideal combination. In the next step, five parameters are selected as variables: orbit heights and inclinations of both sub-constellations, as well as the ratio of the number of satellites in each sub-constellation. The inclinations range from 0° to 90° with a step size of 1°; orbit heights are chosen between 700 km to 900 km with a step size of 50 km; and the ratio of the number of satellites varies from 10:1 to 10:20. Both constellations have a minimum elevation angle of 10°. Table 3-2 shows the best cases where it is observed that having an equal number of satellites in each constellation at orbits heights and inclinations of respectively, (700 km + 38°) and (900 km + 73°), is optimal. These parameters will be considered fixed for further study in this work.

Table 3-2 Best cases of 2 combined sub-constellations with minimum STD of the percentage of satellite visibility. Only part of the best cases with the minimum STD values are listed here

Inclination [°] (1st)	Inclination [°] (2nd)	Orbit height [km] (1st)	Orbit height [km] (2nd)	Satellite number ratio	STD [%]
38	73	700	900	10:10	0.2025
39	73	700	900	10:10	0.2076
37	73	700	900	10:10	0.2093
39	73	700	900	10:9	0.2096
37	72	700	900	10:11	0.2101
38	73	700	900	10:9	0.2116
36	72	700	900	10:11	0.2132

3.4 Constellation type and parameters

As discussed in chapter 3.1, there are various types of satellite constellations. The Walker constellation is a commonly utilized type for designing circular satellite orbit constellations. Many GNSS and communication satellite constellations also use the Walker constellation or similar variants. Therefore, this work will employ the Walker constellation for further design purposes.

The Walker Star constellation has satellites distributed along a semi-circle, causing satellites in adjacent orbital planes to move in the same direction. However, at the end of the semi-circle, there is a seam where satellites in adjacent orbits move in opposite directions (as shown in Fig. 3-3). This presents a problem for communication satellites as connecting two oppositely moving satellites through ISL is either too expensive or impossible due to their high relative velocity. As a result, it is normally assumed that there is no connection over this seam and users may experience long delays at this area despite being geographically close. The Walker Star pattern also suffers from excessive polar coverage. In addition, since all satellites are moving in the same direction, the coverage areas of the Walker Star pattern are sensitive to obstacles such as trees and buildings, which can attenuate the signal quality (Ferreira et al., 2002). Therefore, for this work's purpose, the Walker Delta pattern is a better choice.

To form a Walker Delta constellation, three Walker coefficients $t/p/f$ must be determined. Firstly, the total number of satellites t and the number of orbital planes p for both sub-constellations are investigated using an enumeration method. The basic criterion is to have at least four satellites visible anywhere at any time to fulfill the purpose of communication and navigation while minimizing the total number of satellites used. Fig. 3-13 shows a simple workflow for this search process. The relative phasing coefficient f is assumed to be zero. Since the satellites in the Walker Delta constellation are evenly distributed in one orbital plane, and these planes are also equally distributed, p must be a divisor of t. In the first step, all potential candidates for p are calculated with a certain coefficient of t. Then, by selecting a value for p from these candidates, a Walker Delta constellation can be formed. It is important

to note that under previous assumptions, the total number of satellites t in each sub-constellation is the same while the number of orbital planes p may vary. In this way, if there are n divisors for t, then $U_n^2 = n^2$ combinations need to be checked. For each combination tested, if less than four satellites can be viewed from any point at one epoch, this combination is considered failed. If four or more satellites can be viewed from any point at any epoch, then this combination will be recorded and move on to check the next combination. After checking all combinations for t, the whole workflow goes back to the first step to find all divisors for $t + 1$, and the following steps are similar and can be deduced. The process can continue until one gets a certain number of candidates that satisfy the selection criteria.

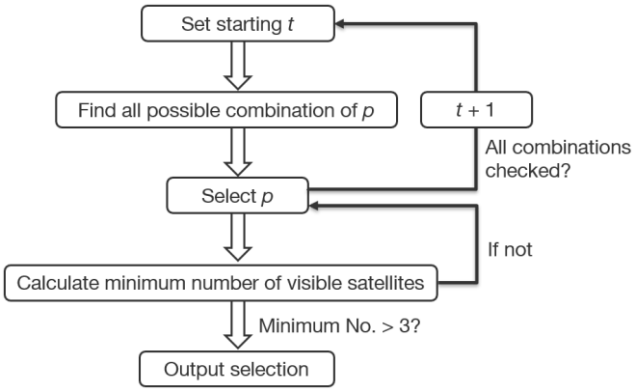

Fig. 3-13 Enumeration method workflow in search of Walker coefficients t and p for both constellations

Table 3-3 Results of enumeration method. The two constellations in search are orbital height of 900 km with Walker Delta 73°: $t/p_1/0$ and orbital height of 700 km with Walker Delta 38°: $t/p_2/0$. Note: t denotes the number of total satellites in each sub-constellation; p_1 denotes the number of orbital planes in higher constellation; p_2 denotes the number of orbital planes in lower constellation

t	p_1	p_2	Number of visible satellites globally
153	9	9	4-18
154	7	22	4-14
160	10	8	4-14
160	10	10	4-13
161	7	23	4-14
189	9	7	6-18
189	9	21	6-18
189	9	9	6-18
203	7	7	6-18
207	9	9	6-18

Table 3-3 provides a list of potential multi-layer constellations. The parameters, such as orbital heights and inclinations, have been predetermined based on previous analyses. Likewise,

the assumption has been made that each sub-constellation will contain an equal number of satellites. It is evident that to achieve at least 4-fold global coverage, a minimum of 306 satellites must be launched under this assumption. To ensure a more robust coverage, the combination of 189 satellites in each sub-constellations, 9 and 7 orbital planes for high and low sub-constellation, which gives more than 6 visible satellites, are selected for further study. However, it should be noted that while this combination is suitable for many scenarios, it may not always be the best choice. Nevertheless, other combinations can also be derived using similar methods.

The relative phasing coefficient f can affect the geometry of the constellation. Dilution of precision (DOP) is another crucial measure for assessing satellite geometry's influence on navigation. DOP is a geometric factor that indicates how measurement errors affect estimation accuracy. A smaller DOP implies more observed satellites and better distribution above the receiver. Table 3-4 displays mean, RMS, and maximum position dilution of precision (PDOP) values worldwide for one revolution by combining two constellations with different relative phasing coefficients. The table clearly demonstrates that changing the relative phasing alters satellite geometry and can affect positioning accuracy. For example, sub-constellation relative phasing with $f_1 = 8$ and $f_2 = 6$ results in much worse geometry than other cases. Although sub-constellation relative phasing with $f_1 = 1$ and $f_2 = 2$ yields ideal mean and RMS of PDOP values, its maximum value is much higher than other scenarios'. This means that certain areas at some epochs have significantly worse PDOP than others. Therefore, to ensure uniform distribution throughout further study, this work will use $f_1 = 1$ and $f_2 = 1$ as selected parameters.

Table 3-4 PDOP of multi-layer constellation with different relative phasing coefficient. The two constellations in search are orbital height of 900 km with Walker Delta 73°: 189/9/f_1 and orbital height of 700 km with Walker Delta 38°: 189/7/f_2. Note: f_1 denotes the relative phasing in higher constellation; f_2 denotes the relative phasing in lower constellation

f_1	f_2	Mean of global PDOP	RMS of global PDOP	Max value of global PDOP
1	0	2.78	3.74	39.07
1	1	2.76	3.73	34.39
1	2	2.77	3.74	436.75
1	4	2.76	3.73	200.13
2	3	2.65	3.39	72.70
3	5	2.66	3.41	69.55
5	2	2.62	3.37	670.4
8	6	6.15	41.98	2479.1

Fig. 3-14 displays the average number of visible satellites and PDOP worldwide for the final selected multi-layer constellation, consisting of an orbital height of 900 km with Walker Delta 73°: 189/9/1 and an orbital height of 700 km with Walker Delta 38°: 189/7/1. The figure indicates that this constellation is suitable for navigation purposes as it provides more than nine

visible satellites in most locations around the globe, with a PDOP below three, except in polar areas. In mid-latitude regions where most people reside, there are over twelve visible satellites available, and the PDOP can be less than two.

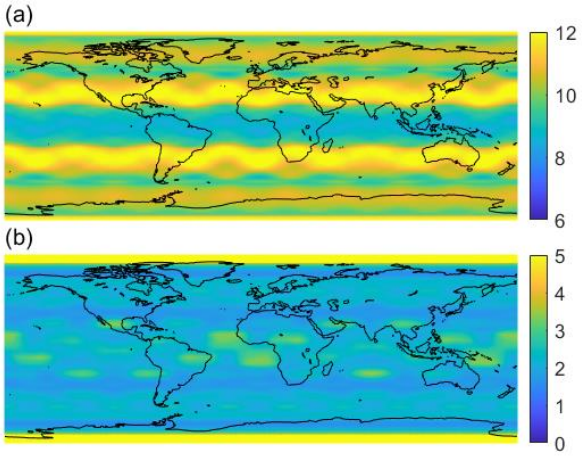

Fig. 3-14 Multi-layer constellation of orbital height of 900 km with Walker Delta 73°: 189/9/1 and orbital height of 700 km with Walker Delta 38°: 189/7/1: (a) average number of visible satellites; (b) average PDOP

The above discussion of DOP values pertains to one-way observation, which requires at least four satellites for navigation. However, as explained in chapter 2.6.1, LEO communication satellites must be able to communicate with ground receivers through both uplink and downlink channels. In this scenario, clock offsets can be eliminated and ideally only three satellites are needed for positioning. Fig. 3-15 compares the PDOP values for one-way and two-way links along different latitudes. The mean and standard deviation of PDOP were calculated from the average PDOP over one revolution. The results show that except for polar areas, the PDOP is relatively uniform and below 3 using one-way links. However, if two-way links are used instead of one-way links, the PDOP can be significantly reduced to around 1 in most areas, which is less than half of what it would be with a one-way link alone. This improvement is especially pronounced in polar regions where the PDOP drops to less than 2 compared to more than 5 (and even up to 13) with a single link. These findings demonstrate that two-way links not only facilitate communication but also enhance positioning accuracy - particularly in challenging environments like polar regions where traditional methods fall short.

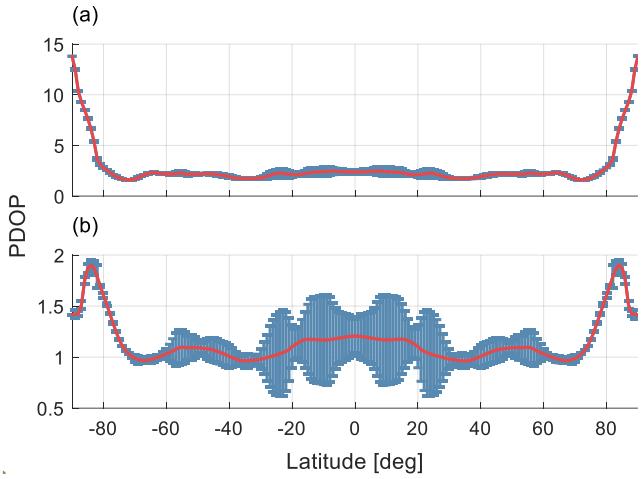

Fig. 3-15 PDOP with respect to the latitude: (a) one-way link; (b) two-way link. Red line is the mean value along latitude. Vertical blue line is the STD of the PDOP in a certain latitude

4 Orbit determination

4.1 Introduction

Orbit determination is a crucial aspect for various applications. Regardless of the purpose and orbit characteristics of satellites or constellations, POD is always a significant topic of discussion. Many researchers also investigate POD studies related to LEO satellites.

The GRACE satellites are utilized to determine the Earth's gravity field. Kang et al. (2003) estimated their orbits shortly after launch using observations from onboard GPS receivers, accelerometers, and attitude data. The dynamic orbit determination method was employed to achieve an accuracy of better than 5 cm. Subsequent research improved precision even further with only GPS observations and different models and methods, achieving a radial direction accuracy of 1 cm and along-track and cross-track direction accuracies of 2.5 cm (Kang et al., 2006). Jäggi et al. (2007) utilized undifferenced and double differenced GPS data to determine GRACE orbits through a reduced dynamic method. The accuracy of their studies, which was better than 2.5 cm, was confirmed by satellite laser ranging (SLR) observations. In 2018, the twin satellites of the continuation mission GRACE Follow-On (GRACE-FO) were launched. SLR residuals demonstrate that sub-centimeter accuracy can be achieved in both radial and cross-track directions, as well as 2 cm in 3D (Kang et al., 2020).

ESA operates the Swarm constellation to study Earth's magnetic field. Montenbruck et al. (2018) have achieved a 30% reduction in orbit errors using observations from an onboard GPS receiver with a macro-model and phase ambiguity fixing, employing the reduced dynamic method. Additionally, they have improved performance by 50% using the kinematic method with ambiguity fixing.

The Sentinel program, developed by ESA for next-generation Earth observation, consists of a series of missions. The Sentinel satellites are located in LEO and monitor various aspects such as Earth's land, ocean, and air quality. Montenbruck et al. (2017) improved the orbit accuracy of the Sentinel-3A satellite using ambiguity-fixed GPS carrier phase observations compared to float solutions, particularly for high-grade stations. Duan and Hugentobler (2019), one of the analysis centers involved in this program, used a zero-difference ambiguity resolution approach to determine the orbits of Sentinel satellites resulting in RMS values smaller than 1 cm across all components when compared to combined solutions from all analysis centers. Mao et al. (2021) also achieved less than 1 cm precision with dynamic orbit determination method for Sentinel-3 satellites.

In addition to the currently operational LEO satellites and constellations, research is being conducted on orbit determination for future LEO satellite constellations, particularly those that will enhance GNSS. Li et al. (2019b) simulated a LEO satellite constellation using only ISL observations and found that with a "4-connected" topology, a 60-LEO satellite constellation can

achieve 3D orbit errors of approximately 0.1 m. Michalak et al. (2021) conducted a full-scale simulation of the proposed Kepler GNSS system by DLR, which includes both MEO and LEO satellites. This high-low system allows for an improvement in MEO SISRE that is 160 times better than that of the Galileo system. Similarly, Li et al. (2021a) simulated observational errors for LEO augmented BDS that closely resemble real-world conditions. Without LEO satellites, orbit errors for BDS MEO satellites are around 1 m; however, with the augmentation of a LEO constellation consisting of 60 satellites, these errors decrease to just 0.69 m. Li et al. (2022a) proposed an ambiguity-fixed method for POD of future LEO constellations. They conducted experiments on four existing LEO satellites and found that this approach can greatly enhance the accuracy of orbits. Specifically, the method reduced the orbit errors of GRACE-FO satellites to less than 5 mm. Wang et al. (2022a) attempted to conduct a near-real-time batch least squares adjustment for LEO satellites. These satellites serve as an augmentation for GNSS, and the observations were obtained from onboard GNSS receivers. The study utilized real data from two LEO satellites to investigate the accuracy of this method. The results indicated that within a processing time of 10 min, orbit errors could reach a few centimeters.

Although there have been numerous studies on LEO POD, some aspects remain unexplored and the investigations lack systematic organization. Most research focuses either on POD for a few LEO satellites or the orbit accuracy of GNSS satellites, with LEO satellites only serving as enhancements. The determination of precise orbits for a fully operational LEO satellite constellation has not received much attention yet. Additionally, many works rely on observations from onboard GNSS receivers to estimate orbits, which is an efficient method but may not be independent enough in light of increasing numbers of LEO satellites in space (as discussed in chapter 1.3). This work systematically discusses the orbit determination of an independent LEO satellite constellation while analyzing various factors that can affect orbit accuracy - from physical structure such as ground station distribution and ISL topology to estimation processes like data weighting and empirical accelerations.

This chapter is structured as follows: section 4.2 describes the requirements and development of the software used in this work. Section 4.3 discusses the influence of empirical accelerations on orbit accuracy and explains how proper empirical parameter settings were selected for this work. Section 4.4 compares orbits determined using different ground station distributions and numbers. It also investigates the advantages of ISL for a small or regionally network of stations. Section 4.5 analyzes LEO satellite orbit determination using different link topologies, including links not only in the same orbital heights but also high-low link types. Section 4.6 focuses on the importance of data weighting for orbit determination with multiple observation types. An efficient weighting algorithm is proposed and examined thoroughly. Lastly, in section 4.7, all of these techniques are employed and a scenario that closely resembles reality is simulated, in order to validate the performance of the independent LEO satellite constellation.

4.2 Software development

To simulate and estimate a LEO mega-constellation, specialized software is necessary. This

software must be capable of simulating orbits and measurements while estimating orbits and other parameters. Additionally, it should account for various error sources, force models, simulation settings, and estimation settings. To meet these requirements, the author has developed the "LeoCon" software.

The software utilized in this project is based on Orekit, an open-source space dynamics library. This low-level Java library was released under Apache License v2.0 in 2008 and provides fundamental elements such as orbits, time, frames, forces, and various algorithms for conversion, propagation, and estimation. Several organizations and companies, including Airbus Defence and Space, Thales Alenia Space, U.S. Naval Research Laboratory (NRL), Swedish Space Corporation (SSC), Centre National d'Études Spatiales (CNES), and ESA, have adopted Orekit for scientific research purposes. These entities apply Orekit in various capacities, for example, Airbus Defence and Space integrates Orekit into their new generation flight dynamics software Quartz, while Thales Alenia Space employs it to enhance the flight dynamics software of its geostationary electric platform SpaceBus Neo (Orekit, 2021).

Orekit is a powerful and useful foundation tool. However, there are some limitations that prevent its direct use in this work. For example, the built-in integrators are either too simple (e.g., 4th order Runge-Kutta method), which reduces accuracy and efficiency, or too complicated (e.g., adaptive step size Dormand-Prince integrator), which results in inconsistent propagation outcomes across multiple runs. Additionally, the built-in least squares method lacks certain functions required for this work. As a batch least-squares method, it cannot handle measurements sequentially - an essential feature for this work due to the large set of measurements involved. It also cannot perform parameter pre-elimination or VCE analysis. Furthermore, Orekit does not implement some aspects that would be useful for applications in this work such as time-variable ISL and piece-wise empirical accelerations. From another perspective, Orekit considers many exceptions and rare occasions to make it more robust with any application; however, this causes the program to be less efficient since many scenarios will not occur in this application. Therefore, it is necessary to simplify some codes to reduce computational burden and save time since Orekit is a general dynamics library designed for various applications rather than specific ones. Lastly, because Orekit is a low-level library without any interface or direct run capability, one must write and compile code specifically tailored towards their tasks. In a simple metaphor, Orekit is like bricks and concrete, which saves time to start from scratch, but it also requires a lot of work to build a house. All in all, further studies require writing custom software tailored explicitly towards the specific needs.

"LeoCon" software utilizes Orekit as its fundamental mathematical and space dynamics library. It rewrites and enhances some of the original functions from Orekit while also implementing new features. In other words, Orekit works as a basic structure. Differential equations, force models, and propagation rely fully or partially on Orekit, whereas other core features like integration, measurements, and least-squares methods are completely or mainly implemented by the author. To improve user-friendliness, "LeoCon" is designed to run both graphically and server-side. Users can either click and type the settings through a graphical user interface (GUI) or write a single script file to execute commands through the command line. Fig. 4-1 displays screenshots of the GUI version of "LeoCon" software. The software can fulfil every aspect of the requirements in this work, from orbit and measurement generation, to

estimation. Specific settings can also be configured, such as the selection of force models, ground stations, ISL types, measurement modifiers, estimated parameters. All subsequent chapters in this work are based on this software.

(a)

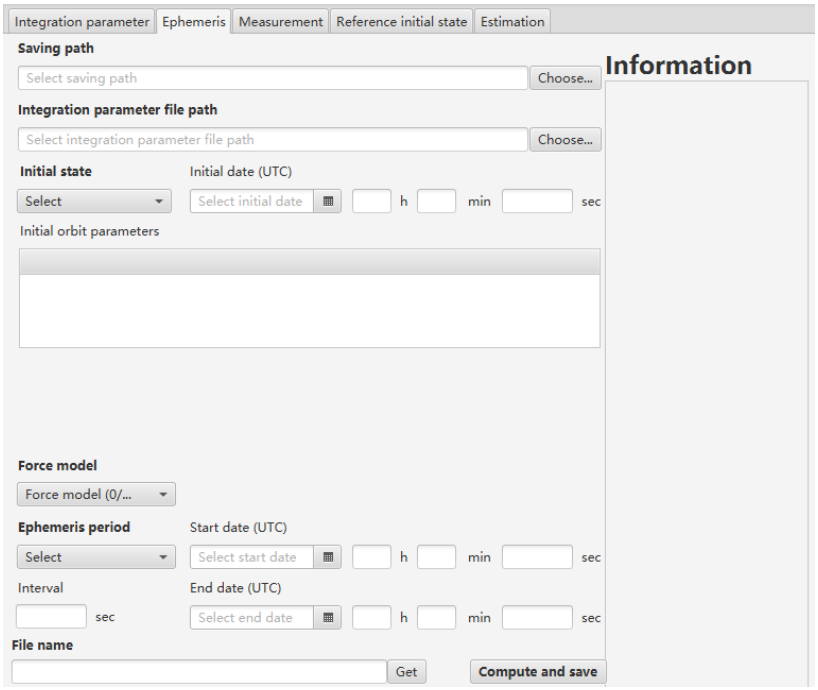

(b)

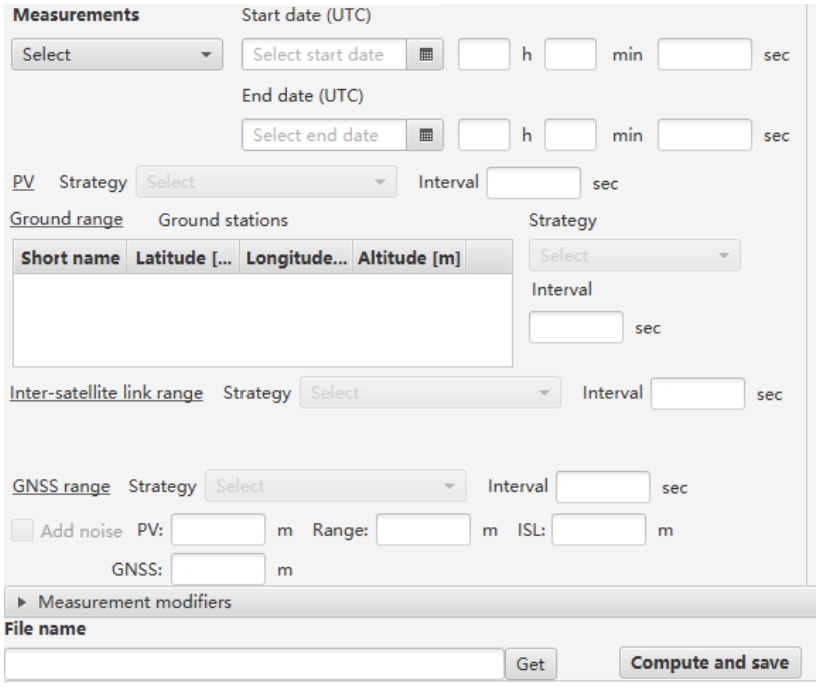

(c)

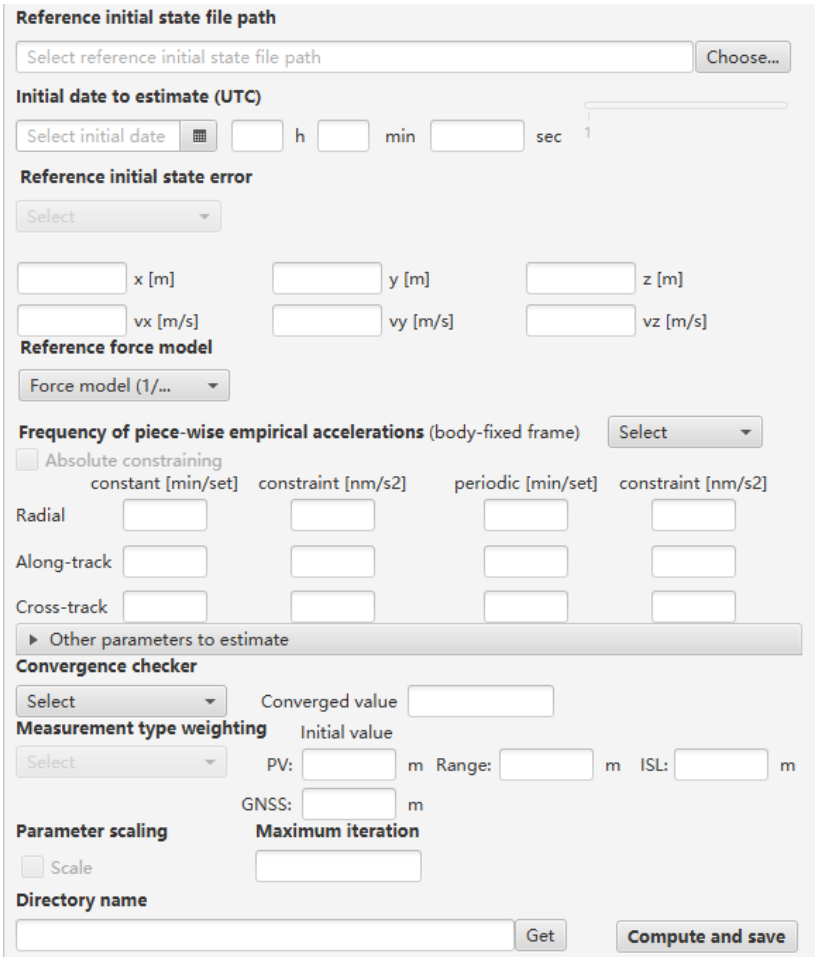

Fig. 4-1 Screenshots for GUI of the software "LeoCon": (a) part of orbit generation settings; (b) part of measurement generation settings; (c) part of estimation settings

4.3 Empirical accelerations

4.3.1 Introduction

Empirical parameters play a crucial role in orbit determination, especially when dealing with complex and dynamic systems. Estimating empirical parameters is a process of tuning the physical models used to describe the dynamics of a satellite in order to fit observed data. The process of obtaining empirical parameters involves a combination of theoretical modeling and data analysis techniques, which can be time-consuming and computationally intensive. However, the benefits of accurately determining these parameters are immense, as they enable the satellite's position and velocity to be accurately determined. Therefore, the estimation of empirical parameters is a critical aspect of orbit determination.

Many scientific studies on orbit determination utilize empirical parameters to enhance the accuracy of orbits, regardless of whether the satellites are in LEO (Kang et al., 2006; Li et al.,

2022a) or MEO (Marz et al., 2021; Duan et al., 2022), and whether the results are from simulations (Schlicht et al., 2020; Michalak et al., 2021) or actual data (Mao et al., 2021; Guo et al., 2022). For LEO satellites, researchers often estimate the empirical parameters per arc, per revolution, or piecewise. Table 4-1 shows a summary of some typical selections.

Table 4-1 Estimation settings of empirical parameters for LEO satellites in some papers

References	Estimation description	Intervals	Constraints
Kang et al. (2006)	1-CPR accelerations	Per revolution	10^{-4} mm/s^2
Bock et al. (2011)	Empirical constant accelerations in radial, along-track and cross-track directions	Per arc	-
Bock et al. (2011)	Piece-wise accelerations	6 min	20 nm/s^2
van den Ijssel et al. (2015)	Piece-wise constant accelerations	6 min	5 nm/s^2 in radial direction, 10 nm/s^2 in along-track and cross-track directions
Allende-Alba and Montenbruck (2016)	Empirical accelerations in radial, along-track and cross-track directions	10 min	The specific value was not mentioned.
Hackel et al. (2016)	Empirical accelerations	10 min	5 nm/s^2 in radial direction, 15 nm/s^2 in along-track and cross-track directions
Li et al. (2017)	Empirical accelerations	360 min	-
Montenbruck et al. (2017)	Piece-wise constant accelerations	10 min	5 nm/s^2 in radial direction, 10 nm/s^2 in along-track and cross-track directions
Guo et al. (2019), Ge et al. (2020a)	1-CPR accelerations in along-track and cross-track directions	Per revolution	-
Mao et al. (2019)	Empirical accelerations	10 min	10 nm/s^2 in radial direction, 40 nm/s^2 in along-track and 20 nm/s^2 cross-track directions
Mao et al. (2021)	Piece-wise constant accelerations	6 min	5 nm/s^2
Michalak et al. (2021)	Piece-wise linear empirical accelerations	30 min	0.1 nm/s^2

Table 4-1 indicates that there are no definitive selection criteria for empirical parameters. The configurations vary depending on the research team, LEO satellites used, and the precision of dynamic models used. Thus, it is crucial to determine the appropriate settings of empirical parameters for the purpose of this work.

This chapter focuses on a more practical simulation scenario aimed at selecting empirical parameters to reduce orbit errors in real-life situations. The chapter considers multiple force models. Moreover, since the constellation in this work has hundreds of LEO satellites, if the intervals for the piece-wise accelerations are very small, the number of estimated parameters will be too large, which is not only difficult for a regular server or computer to process, but also very time-consuming. Therefore, only one LEO satellite is used in this chapter. In order to provide enough observations for the estimation, 60 global ground stations are selected, as shown in Fig. 4-2. For more information on the full simulation and estimation settings, refer to Table 4-2.

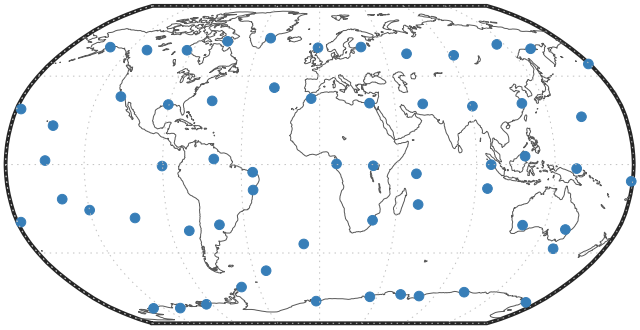

Fig. 4-2 Distribution of the global ground network with 60 stations

Table 4-2 Simulation and estimation settings

Orbit and data simulation		
Orbit	Orbit height 900 km, inclination 73°	
True force models	Earth gravity field	EIGEN 6S 60×60 (Förste et al., 2011)
	Third body attractions	Sun and Moon (Montenbruck & Gill, 2000, pp. 69-77)
	Solid tides	IERS Conventions 2010 (IERS, 2010)
	Ocean tides	IERS Conventions 2010 (IERS, 2010)
	Relativity	Post-Newtonian correction (Montenbruck & Gill, 2000, pp. 110-112)
	Air drag	DTM-2000 atmosphere model with drag coefficient 2.2 (Bruinsma et al., 2003)
	Solar radiation pressure and albedo	Box-wing model with absorption coefficient 0.79, reflection coefficient 0.21 (Knocke et al., 1988; Montenbruck & Gill, 2000, pp. 77-83)
Data time span	7 d (Oct 1 – Oct 7, 2021)	
Sampling interval	1 min	
Elevation cut-off	10°	

Table 4-2 (continued)

Orbit and data simulation		
Ground range	Noise level	White Gaussian noise of 5 mm (Michalak et al., 2021)
	Constant satellite bias	Random in the range ±5 mm (Marz et al., 2021; Michalak et al., 2021)
Estimation		
Arc length	1 d	
Initial state error	Random ±3 mm for position, ±3 μm/s for velocity	
Force models	Earth gravity field	EIGEN 6S 60×60 (Förste et al., 2011)
	Third body attractions	Sun and Moon (Montenbruck & Gill, 2000, pp. 69-77)
	Solid tides	IERS Conventions 2010 (IERS, 2010)
	Ocean tides	IERS Conventions 2010 (IERS, 2010)
	Relativity	Post-Newtonian correction (Montenbruck & Gill, 2000, pp. 110-112)
	Air drag	Modified Harris-Priester atmosphere model with drag coefficient 1.87 (Montenbruck & Gill, 2000, pp. 89-91)
	Solar radiation pressure and albedo	Box-wing model with absorption coefficient 0.88, reflection coefficient 0.12 (Knocke et al., 1988; Montenbruck & Gill, 2000, pp. 77-83)
Parameters	Initial state vector, empirical accelerations, and biases for each LEO satellite and station	

The ground stations are selected from two networks: the International GNSS Service (IGS) and Nevada Geodetic Laboratory (NGL) GPS network. The observations are simulated using white Gaussian noise, with constant satellite biases taken into account. A noise level of 5 mm for ground range measurements are chosen to simulate the typical noise level of microwave links of a few millimeters. However, since this simulation does not include other effects such as atmospheric delays or multipath effects, nor clocks and ambiguities (treated as range), a slightly larger value is selected.

This work uses a 1-day orbit arc length and obtains seven daily solutions. This approach helps to eliminate random anomalies and produce more reliable results. Additionally, some of the reference force models, which are different from the original models in the simulation, are used to introduce systematic errors. A more detailed set-up is presented in Table 4-2. Additionally, station biases (excluding the first one as fixed) and satellite biases are also estimated. A daily constant bias is calculated for each satellite and each station.

4.3.2 Empirical parameters with long intervals

This section focuses on estimating empirical parameters with intervals longer than 1 h, without considering constraints. First, the nine parameters in Colombo model - constant, sine and cosine

terms in each direction - are all estimated using intervals of 1 h, 1.5 h, 2 h, 3 h, 4 h, 6 h, 8 h, 12 h and 24 h, respectively. The case of "per arc" in Table 4-1 can be represented by the 24 h interval case while the case of "per revolution" is represented by the 1.5 h interval case. Fig. 4-3 displays the results of estimated orbit errors.

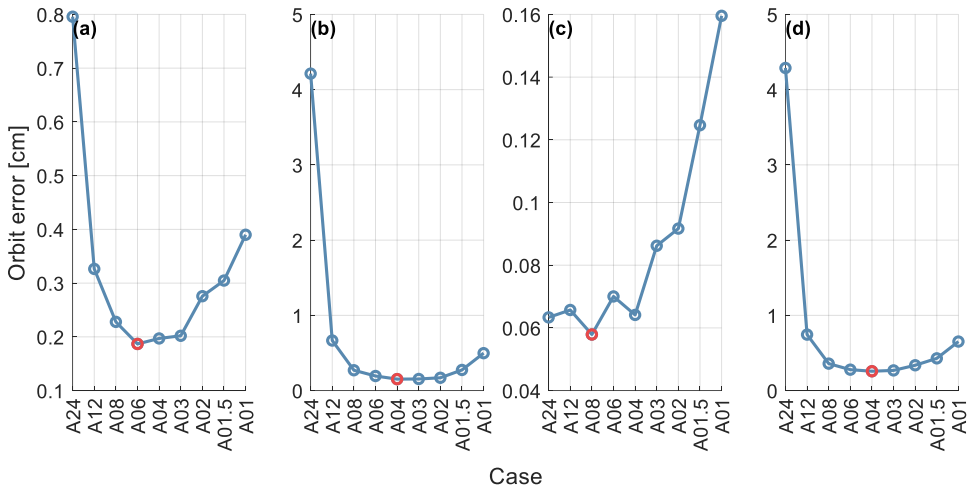

Fig. 4-3 Mean RMS of orbit errors for different empirical parameter cases in (a) radial, (b) along-track, (c) cross-track directions and (d) 3D position. The case notation "A*xx*" means to estimate empirical parameters with *xx* h interval in all three directions. Red circle denotes the case with minimal value. Notify the different scales

Fig. 4-3 uses "A*xx*" on the abscissa to represent cases with *xx* h intervals in all three directions. For instance, "A24" indicates that empirical parameters are estimated using 24 h intervals in radial, along-track, and cross-track directions. The figure shows that the "A04" case has the smallest 3D orbit errors overall. All cases except for "A24" can achieve 3D orbit errors below 1 cm, with differences among them within 0.5 cm. Specifically, "A03", "A04", and "A06" cases perform better in radial and along-track directions, while "A08" case is better in the cross-track direction. Orbit errors in radial and along-track directions exhibit a "U" pattern where orbit accuracy degrades when the intervals are too long or short. However, when estimating empirical parameters more frequently in the cross-track direction, orbit errors gradually increase.

To further investigate the influence of different intervals in different coordinate components, this study conducts additional simulations. The radial and along-track directions are tested with 3 h, 4 h, and 6 h intervals respectively based on the results from Fig. 4-3. Meanwhile, the cross-track direction is fixed at an interval of 8 h. The results are presented in Fig. 4-4.

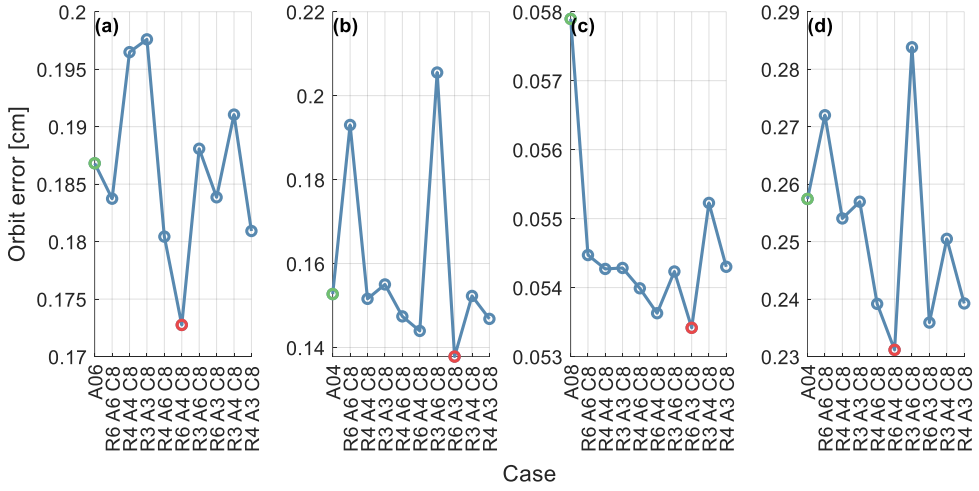

Fig. 4-4 Mean RMS of orbit errors for different empirical parameter cases in (a) radial, (b) along-track, (c) cross-track directions and (d) 3D position. The case notation "R*x* A*y* C*z*" means to estimate empirical parameters with *x* h interval in radial direction, *y* h interval in along-track direction, and *z* h interval in cross-track direction. Green circle denotes the best case from the previous figure, and red circle denotes the case with minimal value. Notify the different scales

Fig. 4-4 displays the orbit errors resulting from estimating empirical parameters with different intervals in three directions. The notation "R*x* A*y* C*z*" represents the case where *x*, *y*, and *z* are the intervals in the radial, along-track, and cross-track directions respectively. For example, "R6 A4 C8" indicates that empirical parameters are estimated using a 6 h interval in the radial direction, a 4 h interval in the along-track direction and an 8 h interval in the cross-track direction.

It is evident that the "R6 A4 C8" case provides the best fit to true orbit. Compared to the previous best case ("A04"), it further reduces orbit errors by approximately 10%. While some cases show worse performance than the previous best case (green circle) in radial and along-track directions, all cases exhibit improvement in the cross-track direction. However, these improvements are not significant as they are less than 0.02 cm for radial and along-track directions and less than 0.01 cm for the cross-track direction. Nevertheless, investigating these improvements is worthwhile because it can reduce computational burden by reducing the number of estimated empirical parameters. For instance,"R6 A4 C8" can reduce up to 33% and 50% of parameters required for estimation of empirical parameters in radial and cross- track directions respectively while still providing comparable or even slightly better results compared to "A04" case.

From another perspective, Fig. 4-5 displays the air drag force in various coordinate components. It is evident that the drag force in the radial direction is approximately two magnitudes smaller than in the other directions. As the largest non-gravitational perturbation acting on LEO satellites, this difference may indicate an overparameterization in the radial direction. This point finds support in some papers (Guo et al., 2019; Ge et al., 2020a), which only estimate empirical parameters for LEO satellites in along-track and cross-track directions. Therefore, the following part tries to reduce the number of estimated parameters in the radial direction. Fig. 4-6 shows the result.

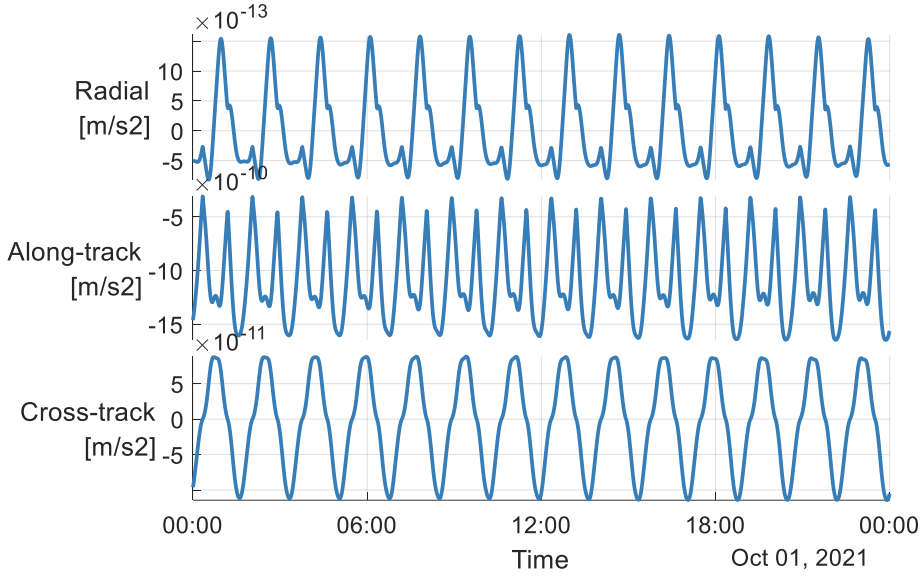

Fig. 4-5 Air drag force on a LEO satellite in each direction of the body frame. Based on the data from DTM-2000 atmospheric model on 01.10.2021. Notify the different scales

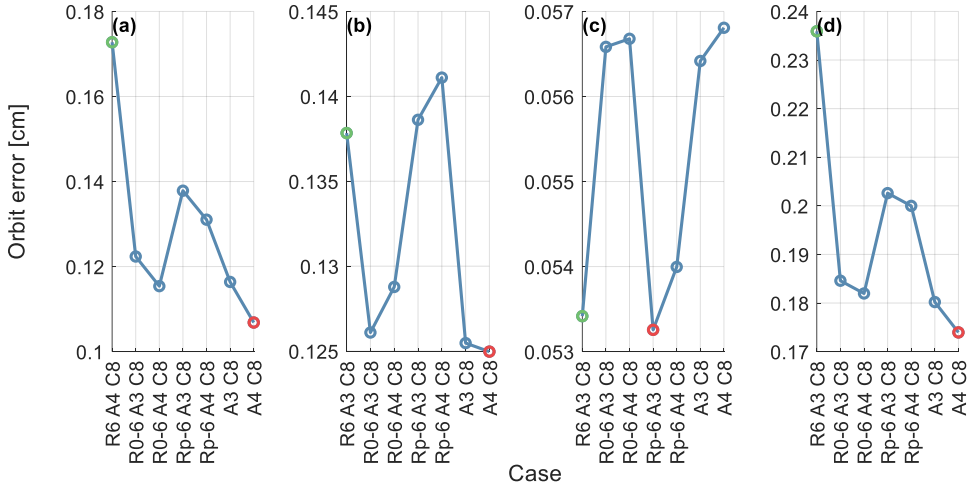

Fig. 4-6 Mean RMS of orbit errors for different empirical parameter cases in (a) radial, (b) along-track, (c) cross-track directions and (d) 3D position. The case notation "R0-*x* A*y* C*z*" or "Rp-*x* A*y* C*z*" means to estimate empirical parameters with *x* h interval in radial direction, *y* h interval in along-track direction, and *z* h interval in cross-track direction. "R0" indicates that in radial direction only the constant term is estimated, while "Rp" is to estimate only the periodic terms in radial direction. Green circle denotes the best case from the previous figure, and red circle denotes the case with minimal value. Notify the different scales

In this scenario, as shown in Fig. 4-6, the empirical parameters in the radial direction are reduced to either only the constant term ("R0-*x* A*y* C*z*" cases), or only the periodic term ("Rp-*x* A*y* C*z*" cases), or not estimated at all ("A*y* C*z*" cases). This approach leads to better estimation of orbit in the radial direction. The "A4 C8" case performs best and improves the orbit by 38%

in the radial direction compared to the previous best case "R6 A4 C8". For the along-track direction, orbit errors can be further reduced if only a constant term or no estimation is implemented in the radial direction. The best case "A4 C8" reduces orbit errors by 10% in this direction compared to the previous best case "R6 A3 C8". In cross-track direction, since it is already well-determined than other two directions, differences are insignificant - less than 0.005 cm. Overall, in the application of this work, the "A4 C8" case performs best. Compared to the "per arc" solution ("A24" case), the 3D orbit errors are reduced from centimeter level to only a few millimeters. Compared to the "per revolution" scenario ("A0.15" case), the 3D orbit accuracy improves by 59%.

4.3.3 Empirical parameters with short intervals

As Table 4-1 summarizes, many studies prefer using very short intervals, such as 10 or even 6 min, to estimate empirical parameters. Due to the short intervals used, constraints are often applied to stabilize the solution. This section aims to investigate the advantages of using these short intervals for determining the orbit of LEO satellites and discuss how changing interval lengths and constraint values can affect orbit accuracy. It is also important to determine an appropriate interval length and constraints for this study. The simulation and estimation settings are listed in Table 4-2. To briefly summarize, different reference models and true models were selected for air drag and SRP to introduce systematic errors.

To investigate the impact of interval variation, according to Table 4-1, six different short intervals are tested: 30 min, 20 min, 15 min, 10 min, 6 min and 5 min. The constraints are changed from 40 nm/s^2 to as low as 5 nm/s^2. Additionally, extreme cases with a constraint of only 0.1 nm/s^2 are also included in the study. The results for some typical cases from section 4.3.2 and those with a constraint of only 0.1 nm/s^2 are listed in Table 4-3 while orbit errors for other cases can be seen in Fig. 4-7. It is important to note that the notation "R*xx* A*yy* C*zz*" used here differs from the previous notation "R*x* A*y* C*z*" shown in Fig. 4-4 where it represents the estimation interval previously whereas here it represents the constraint value.

Table 4-3 Mean RMS of orbit errors in radial, along-track, cross-track directions and 3D position for different empirical parameter settings

Empirical parameter settings		Orbit errors [cm]			
Interval	Constraints	Radial	Along-track	Cross-track	3D
(R, A, C): 24 h	-	0.796	4.213	0.063	4.288
(R, A, C): 1.5 h		0.305	0.274	0.125	0.429
A:4 h, C: 8 h		0.107	0.125	0.057	0.174
5 min	(R, A, C): 0.1 nm/s^2	0.850	1.989	2.920	3.660
6 min		0.745	1.736	2.827	3.423
10 min		0.519	1.188	2.520	2.847
15 min		0.400	0.889	2.244	2.456
20 min		0.342	0.736	2.055	2.216
30 min		0.296	0.597	1.849	1.970

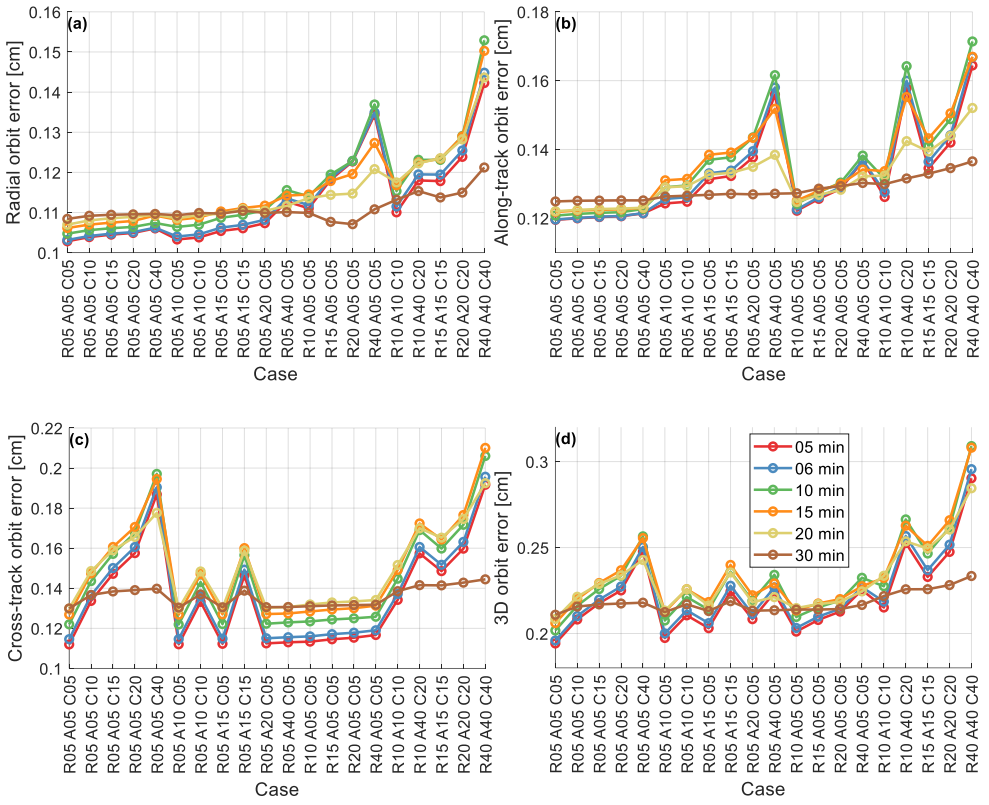

Fig. 4-7 Mean RMS of orbit errors in (a) radial, (b) along-track, (c) cross-track directions and (d) 3D position for empirical parameter settings with different intervals and constraints. The case notation "R*xx* A*yy* C*zz*" means to estimate empirical parameters with *xx* nm/s^2 constraints in radial direction, *yy* nm/s^2 constraints in along-track direction, and *zz* nm/s^2 constraints in cross-track direction. Different colors of lines indicate different estimation intervals. Notify the different scales

Fig. 4-7 demonstrates that orbit errors exhibit similar patterns and values when the interval is less than 20 min. However, for the cases with intervals of 30 min, the orbit errors do not change much, only about 0.02 cm difference. Generally, smaller intervals result in smaller orbit errors.

From a different perspective, when empirical parameters are constrained with a large value in one direction, that direction usually experiences larger errors, especially for cases with small intervals. Loose constraints and more parameters to estimate may result in unstable solutions and relatively large errors. For instance, for a case with a 5 min interval, if the radial constraints loosen from 5 nm/s^2 to 10 nm/s^2, 15 nm/s^2, 20 nm/s^2 and 40 nm/s^2, the orbit errors in this direction will increase by 8%, 15%, 19% and 31%, respectively.

On the other hand, highly constrained parameters cannot compensate well for modeling errors leading to large orbit errors too. Table 4-3 shows that if the constraints are set at only 0.1 nm/s^2, then orbit errors can increase from below 0.4 cm to over 1.9 cm. In the highly constrained cases, the more the estimated parameters are, the worse the orbit is. The 3D orbit errors gradually increase from 1.97 cm to 3.66 cm as the interval decreases from 30 min to 5 min.

Compared to the previous results with longer intervals, cases with shorter intervals

perform well in the radial and along-track directions but have relatively larger errors in the cross-track direction. Consequently, 3D orbit errors are generally better than those of "A01.5" (per revolution) case but less accurate than some of the cases shown in Fig. 4-4 and Fig. 4-6. The most optimal case with a short interval is the one where there is a 5 min interval with constraints of 5 nm/s^2 in all three directions resulting in approximately 0.194 cm for the 3D orbit errors.

4.3.4 Conclusions

Estimating empirical parameters helps to improve orbit modeling and increase orbit accuracy. This chapter focuses on the influence of different empirical parameter settings on orbit determination. Not only the estimation intervals in each direction are discussed, but also the constraints.

The first part of the study investigates various intervals for empirical parameters in each direction that are longer than 1 h. When all directions are estimated with the same interval, a "U" shaped change is observed in the 3D orbit errors as the intervals gradually decrease. This indicates that neither too long nor too short intervals are ideal for improving orbit accuracy. Different directions perform better with different estimation intervals. If the intervals are not appropriately given, it can negatively affect orbit accuracy, resulting in errors of over 4 cm. In the scenario of this work, it was found that the best case occurs when there is no estimation of empirical parameters in the radial direction and empirical parameters are estimated at a 4 h interval in the along-track direction and an 8 h interval in the cross-track direction. Under these conditions, 3D orbit errors can be reduced to as low as 0.17 cm.

The study also examines the estimation of short intervals less than 30 min with absolute constraints. The results indicate that orbits can be well-determined with an error of approximately 0.22 cm for cases with a 30 min interval, and different constraints do not have much impact on these cases. In general, orbit accuracy improves with shorter intervals, and relatively harder constraint values in a direction lead to decreased orbit errors in that direction. However, overly tight constraints result in much larger orbit errors (more than 1.9 cm). The optimal case is to estimate piece-wise constant empirical parameters using 5 min intervals and applying 5 nm/s^2 constraints in all directions, which yields an orbit accuracy of about 0.19 cm.

4.4 Ground station network and ISL

4.4.1 Introduction

Ground stations play a crucial role in determining the orbit of satellites. Ideally, there should be a uniform global distribution with as many stations as possible. However, achieving this is not always possible due to geopolitical factors (such as ground segments for BDS) and geographical reasons (such as fewer stations in the southern hemisphere due to large bodies of water). Several studies have been conducted on the influence of station distribution on GNSS. For example, Zhang et al. (2015) compared the orbit accuracy of BDS-2 satellites using both

regional (Asia-Pacific) and global ground networks. They found that since BDS-2 mainly consists of GEO and Inclined Geosynchronous Orbit (IGSO) satellites, ground stations in this area play a key role in orbit determination. Similarly, Yang et al. (2020) and Kur and Kalarus (2021) investigated changes in orbit accuracy with varying numbers of ground stations for BDS-3 and Galileo respectively.

To address this problem, ISL has been adopted for GPS and BDS, and proposed for Galileo. ISL was introduced in the 1980s as additional observations for GPS (Ananda et al., 1984; Chory et al., 1984; Ananda et al., 1990). Initial results from GPS Block IIR satellites with ISL showed that a 3 m URE can be achieved over 75 days of autonomous navigation (Rajan, 2002). Similar linking systems have also been planned or implemented by other GNSS such as GLONASS, Galileo, and BDS (Fernández, 2011; Urlichich et al., 2011; Ren et al., 2017). The new generation BDS-3 is equipped with Ka-band phased-array antennas which enables inter-satellite ranging and communication (Yang et al., 2017). Researchers analyzing data from BDS-3 proved that ISL can enable autonomous orbit determination while improving orbit accuracy by about 50% (Tang et al., 2018; Yang et al., 2019; Guo et al., 2020). The second-generation Galileo satellites will also be equipped with K-band ISL technology, which are about to launch earliest in 2024 (European-Commission, 2021). Simulation studies show that using ISL enhances measurement geometry resulting in better estimation of orbit modeling parameters while reducing orbit errors (Schlicht et al., 2020; Kur & Kalarus, 2021; Marz et al., 2021).

Numerous studies have been conducted on the orbit determination of GNSS satellites using ground networks and ISL. However, little attention has been given to LEO satellites. Li et al. (2019b) demonstrated that a "4-connected" link topology can result in 3D orbit errors of approximately 0.1 m for a constellation of 60 LEO satellites if no orbit perturbations are considered during simulation. The use of an "all-connected" topology can reduce these errors by half. Michalak et al. (2021) performed a full-scale simulation for the new GNSS Kepler system, which includes additional LEO satellites to improve MEO satellite performance and potentially decrease ground segments, with different applications compared to this study. All satellites in this system are equipped with two-way optical ISLs. With this high-low system, the MEO SISRE can be 160 times better than that of the Galileo system. Wang et al. (2022b) proposed an algorithm that aims to select ground stations for LEO satellites based on increasing visibility and shortening gaps, which differs from the goals of this study. They found that less than 30 global stations can achieve over 98% visibility excluding polar regions for a LEO satellite at an altitude of 1200 km and inclination angle of 50°.

However, there has been no systematic discussion on the influence of station distribution and number on orbit determination results. Additionally, the contribution of ISL to the independent LEO satellite system's orbit accuracy has not been thoroughly studied. This chapter aims to systematically analyze the impact of different ground networks and ISL observations on determining the orbits of a large LEO constellation. Some contents in this chapter are referenced from previously published work (He et al., 2022).

4.4.2 Simulation

To reduce the computation burden, only half of the original sub-constellation proposed in

chapter 3 is used. Specifically, a Walker Delta constellation with parameters 900 km and 73°: 90/9/1 is selected for LEO satellites. The accuracy of orbit determination is also affected by the link topology of ISL. Different topologies such as "4-connected", "all-connected", "ring" and "open ring" have been investigated previously (Li et al., 2019b; Schlicht et al., 2020; Kur & Kalarus, 2021). This chapter adopts the "4-connected" topology which connects each satellite permanently to two neighboring satellites in the same orbital plane and closest satellites in each of the two neighboring orbital planes (Fig. 4-8), similar to Iridium - a well-known LEO communication system (Werner et al., 1995; Gvozdjak, 2000). The impact of different ISL types on orbit accuracy will be discussed in detail in the following chapter 4.5. In this study, four terminals for ISL and one terminal for ground range per satellite are used. Each terminal has a different bias. Each ISL terminal connects to one other satellite per epoch while one ground station can observe several satellites. The minimum and maximum link distance observed in this study are respectively at distances of 2246 km and up to a maximum distance of 5401 km.

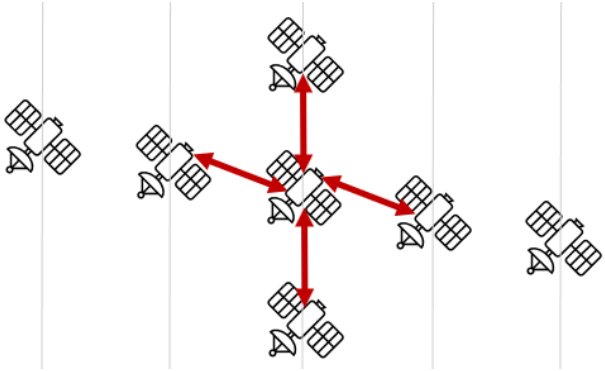

Fig. 4-8 Illustration of "4-connected" ISL topology (He et al., 2022)

Air drag is the most significant non-gravitational perturbation for a LEO satellite (Montenbruck & Gill, 2000, p. 83). This chapter will focus on this primary perturbation while disregarding other disturbances like SRP and albedo. The objective is to examine how the distribution and number of ground tracking stations affect satellite orbits. Table 4-4 provides all the necessary settings for orbit simulation and estimation.

Table 4-4 Simulation and estimation settings (He et al., 2022)

Orbit and data simulation		
Orbit height	900 km	
Walker constellation	73°: 90/9/1	
True force models	Earth gravity field	EIGEN 6S 60×60 (Förste et al., 2011)
	Air drag	DTM-2000 atmosphere model (Bruinsma et al., 2003)
Data time span	7 d (Oct 1 – Oct 7, 2021)	
Sampling interval	1 min	
Elevation cut-off	10°	
Ground range	Noise level	White Gaussian noise of 5 mm (Michalak et al., 2021)
	Constant satellite bias	Random in the range ±5 mm (1 terminal for each satellite) (Marz et al., 2021; Michalak et al., 2021)
ISL	Noise level	White Gaussian noise of 1 mm (Michalak et al., 2021)
	Constant satellite bias	Random in the range ±5 mm per terminal (4 terminals for each satellite) (Michalak et al., 2021)
Estimation		
Arc length	1 d	
Initial state error	Random ±3 mm for position, ±3 μm/s for velocity	
Data weighting	Fixed weight with $\sigma_{\text{range}} = 5$ mm, $\sigma_{\text{ISL}} = 1$ mm	
Force models	Earth gravity field	EIGEN 6S 60×60 (Förste et al., 2011)
	Air drag	Modified Harris-Priester atmosphere model (Montenbruck & Gill, 2000, pp. 89-91)
Parameters	Initial state vector, empirical accelerations per arc, and biases for each LEO satellite and station (as explained at the end of this section)	

As mentioned in section 4.3.1, the ground stations used in this study are selected from two networks: the IGS and NGL GPS networks. Both types of observations are simulated using white Gaussian noise, with constant satellite biases taken into account. It should be noted that the bias for ground range observations differs from that of ISL observations for the same satellite, as they typically do not share the same antenna. Table 4-4 provides further details on how measurements were simulated, with values inspired by other simulation studies. A noise level of 5 mm for ground range measurements are chosen to simulate the typical noise level of microwave links of a few millimeters.

The simulation introduces systematic air drag errors by using a reference atmosphere model that differs from the original simulation model. For further details on the methodology, please refer to Table 4-4.

Empirical accelerations are commonly utilized to correct for errors in force modeling.

Empirical parameters are estimated in the along- and cross-track directions per arc, together with the initial orbit state vector of the satellites (Ge et al., 2020a; Kang et al., 2020). In each direction, one constant parameter and two 1-CPR coefficients (sine and cosine term) are estimated. Additionally, station biases (excluding the first one as fixed) and satellite biases are estimated, too. For antennas pointing towards the ground, a daily constant bias is calculated for each satellite and each station. Whereas for ISL antennas, only one bias value is determined for each pair of linked satellites instead of two biases for each terminal of each satellite, since it is not possible to estimate a single ISL terminal's bias as only their sum is observable.

4.4.3 Influence of ground station distribution

Fig. 4-9 displays eight distinct ground networks that are chosen for this study. To represent local ground networks in different latitudes, three regional networks situated in Europe, China, and Brazil are selected as examples. Additionally, to expand the scope of these regional networks, three quasi-global networks distributed along a latitude circle at high, middle and low latitudes are also selected for comparison purposes. Furthermore, a quasi-global network distributed along a given longitude is included in the selection process. Finally, a global network consisting of six ground stations is used as comparison.

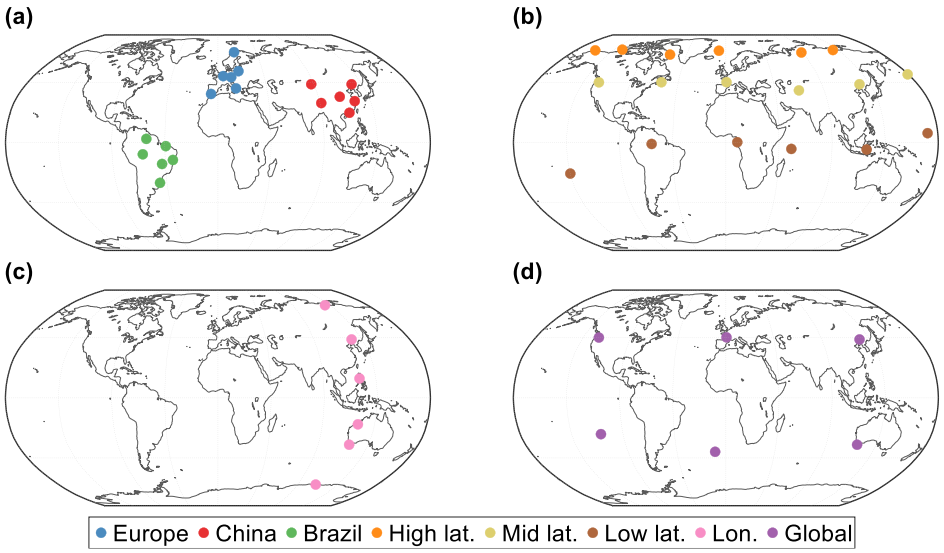

Fig. 4-9 Distribution of different ground networks: (a) regional, (b) quasi-global along latitudes, (c) quasi-global along longitude and (d) global

The study compares individual satellite orbit solutions to simulated true orbits and presents the mean RMS of orbit errors in Table 4-5. For comparison, a new criterion called the best possible orbit, which will be denoted as "BPO" in the following figures, is introduced in this work. The best possible orbit is obtained by adjusting the true orbit based on reference force models and represents the most optimal solution achievable with current modeling errors. Further details about the best possible orbit can be found in Schlicht et al. (2020) and Marz et

al. (2021). Fig. 4-10 gives the 3D mean RMS of orbit errors for each satellite and the mean value for each simulation case without and with ISL observations. This figure reveals both averaged and scattered orbit errors. This figure also demonstrates that ISL observations improve overall orbit accuracy significantly.

Table 4-5 Mean RMS of orbit errors in radial, along-track, cross-track directions and 3D position [cm] (He et al., 2022)

Station network		Radial	Along-track	Cross-track	3D
Europe	without ISL	0.58	1.99	0.92	2.36
	with ISL	0.11	0.54	0.16	0.59
China	without ISL	0.49	1.65	0.66	1.89
	with ISL	0.11	0.56	0.20	0.62
Brazil	without ISL	0.44	1.62	0.67	1.86
	with ISL	0.11	0.56	0.18	0.61
High lat.	without ISL	0.39	1.41	1.60	2.31
	with ISL	0.11	0.51	0.16	0.56
Mid lat.	without ISL	0.17	0.66	0.59	0.95
	with ISL	0.11	0.52	0.08	0.54
Low lat.	without ISL	0.17	0.63	0.63	0.95
	with ISL	0.11	0.52	0.09	0.55
Lon.	without ISL	0.24	0.75	0.24	0.84
	with ISL	0.11	0.52	0.10	0.54
Global	without ISL	0.16	0.62	0.15	0.66
	with ISL	0.11	0.52	0.08	0.54
Best possible		0.11	0.51	0.01	0.52

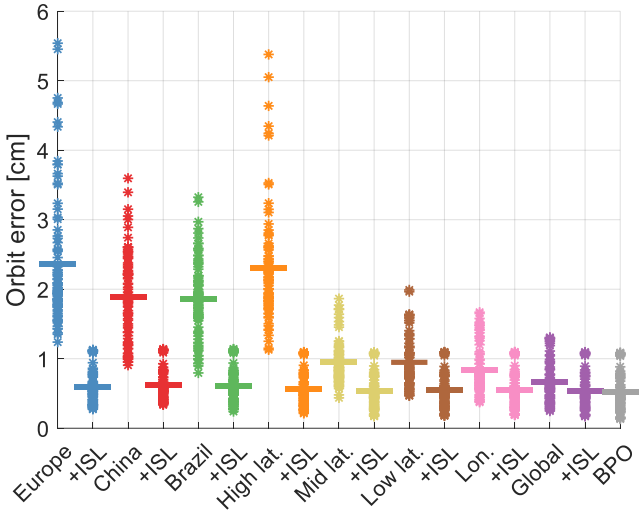

Fig. 4-10 3D mean RMS of orbit errors for each case. For each case, orbit errors of individual satellite are marked as stars and the mean of all satellites is marked as a bar. "+ISL" means that ISL observations are included in the estimation together with observations from the station network of the same color (He et al., 2022)

Table 4-5 shows that the along-track error dominates the orbit error. To demonstrate how station distribution affects the orbit accuracy, the cases with only ground range observations will be discussed first. Fig. 4-10 indicates that regional networks have a 3D mean RMS of orbit errors above 1 cm, while quasi-global networks show a decrease in orbit errors to below 1 cm for middle and low latitude networks. However, the high latitude quasi-global network exhibits much larger errors in all three directions, leading to a significantly higher 3D orbit error compared to other quasi-global networks due to its proximity to the north pole, which makes it behave like a polar regional network (as shown in Fig. 4-9). Therefore, compared with other quasi-global networks, this high latitude quasi-global network behaves like a regional network. On the other hand, Table 4-5 reveals that orbits determined with longitude quasi-global network are as accurate as those from low latitude quasi-global network orbits because they determine the cross-track direction orbits at least by 59% better than latitude quasi-global networks do. When ground stations are globally distributed, optimum accuracy is achieved for orbit determination. In general, with the same number of ground stations, as the stations are more widely dispersed, the orbit errors decrease. Switching from regional to global or even just quasi-global network (except high latitude quasi-global) improves the estimated 3D mean RMS of orbit errors by at least 49% and up to around 65% for the global case.

From another perspective, including ISL observations in the estimation process reduces orbit errors in all cases. The 3D mean RMS of orbit errors for all cases are below 0.7 cm. ISL observations improve the 3D orbit accuracy by about 70% for regional networks, but as a network expands to a broader region, adding ISL observations results in only minor improvements. The reason can be explained with the help of the best possible solution. Orbits determined solely with a global network that does not consider ISL observations are already accurate, differing only by 0.14 cm from the best possible orbit solution. However, due to modeling errors, adding ISL observations decreases orbit errors to the same level as the best possible solution and the orbit errors cannot be further reduced. For the same reason, due to the reduction of orbit errors in both radial and along-track directions to the same level as the best possible solution with ISL, there is minimal variation of orbit errors in these two directions when alterations are made to the network. It can also be observed that adding ISL observations to a regional network significantly reduces orbit errors, bringing them close to the level of the best possible solution. Furthermore, as depicted in Fig. 4-10, the addition of ISL observations when using a regional network results in even slightly better orbits compared to a global network without ISL observations. This is significant because establishing a global network may not always be feasible. Although errors in orbit mainly occur in the along-track direction due to mismodeling, as demonstrated by the best possible solution presented in Table 4-5, ISL still aids in reducing errors in this direction to the same level as that of the best possible solution. Particularly for regional networks, implementing ISL enhances orbit accuracy in the along-track direction by at least 65%. In conclusion, to obtain precise orbits, for a regional station network, it is necessary to implement ISL; while for a global network, orbit determination also benefits from ISL observations.

It is important to note the significance of station distribution geometry. Regional networks have a mean maximum gap with no observations longer than 600 minutes, while the global network only has gaps around 150 minutes. This indicates that global networks can observe

satellites more frequently, whereas regional networks are limited in tracking only a portion of the daily arc due to their geometry limitations. As a result, orbit determination of the regional network is less accurate. To gain further understanding of the solution quality, refer to Table 4-6 which provides the mean formal errors of the initial state vector's position and the average number of daily observations. These cases here involve orbits determined solely through ground station observations. For comparison purposes, note that there are approximately 260000 ISL observations per day on average.

Formal errors in regional networks and high latitude quasi-global network are at least 67% worse than other networks due to the poor geometry. The constellation's inclination of 73° and orbits convergence towards northern and southern latitudes cause satellites in the simulation to pass through polar regions every revolution, resulting in more observations for higher latitude stations. For instance, the high latitude quasi-global network has significantly more observations compared to the other two latitude quasi-global networks. However, despite having more observations, this network produces much worse orbits due to its poor station distribution geometry as shown by Table 4-5 and Fig. 4-10. In summary, a better geometry distribution is more important for orbit determination rather than increasing observation numbers.

Table 4-6 Formal errors of initial 3D orbit position and average number of observations per day, all cases are without ISL observations (He et al., 2022)

Station network	Formal errors [cm]	Average number of observations per day
Europe	1.71	30536
China	1.86	21029
Brazil	2.16	16974
High lat.	1.72	44507
Mid lat.	0.63	24725
Low lat.	0.64	15519
Lon.	0.46	27637
Global	0.32	21556

In addition to analyzing orbit accuracy, this study also examines the estimated bias accuracy. Generally, ground range biases can be estimated with an accuracy of better than 0.6 mm, while the pair of ISL bias errors are below 1.5 mm. The station distribution and number of observations both play a key role in bias estimation (see Fig. 4-11). To investigate the necessity of on-ground satellite bias calibration, this work further compares the orbit accuracy with and without biases. Table 4-7 shows the orbit errors determined with the observations from a global network with and without biases. For cases with simulated biases, joint bias and orbit estimation is performed; for cases without simulated biases, no biases are estimated. Obviously, with bias estimation during orbit determination process, the same level of orbit accuracy as that obtained from observations without biases can be achieved. Therefore, precise pre-launch satellite bias calibration is not necessary for estimating precise orbits, if the biases are estimated

during the orbit determination process.

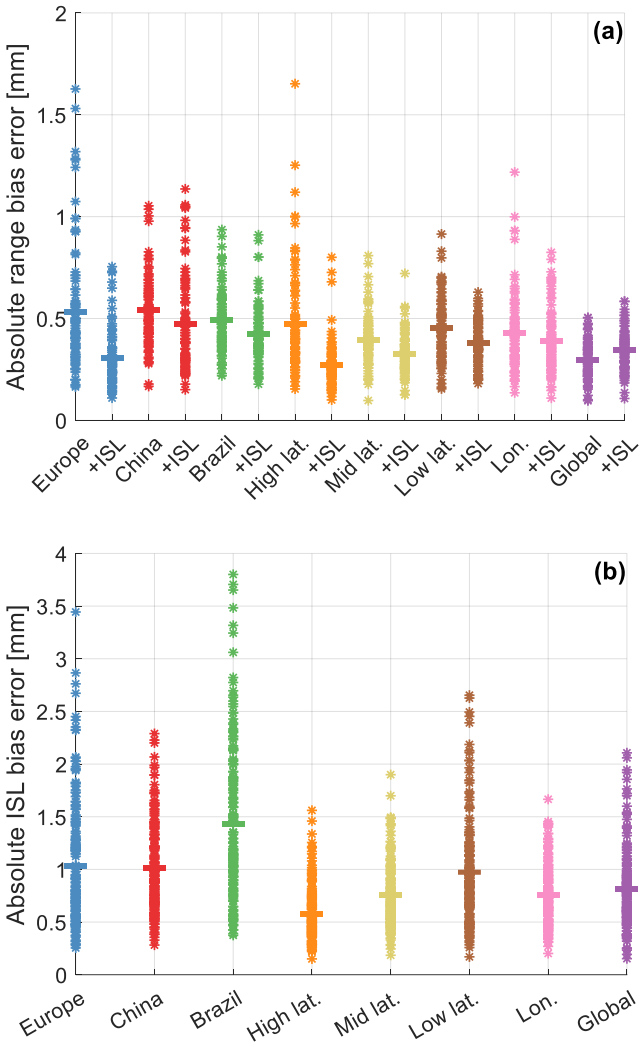

Fig. 4-11 Absolute bias errors for each case: (a) absolute ground range bias errors; (b) absolute ISL bias errors (per pair). For each case, bias errors of individual satellites (for ground range biases) and each pair of satellites (for ISL biases) are marked as stars and the mean of all biases is marked as a bar. "+ISL" means that ISL observations are included in the estimation together with observations from the station network of the same color (He et al., 2022)

Table 4-7 Mean RMS of orbit errors in radial, along-track, cross-track directions and 3D position, global network [cm] (He et al., 2022)

Case		Radial	Along-track	Cross-track	3D
With biases and bias estimation	without ISL	0.16	0.62	0.15	0.66
	with ISL	0.11	0.52	0.08	0.54
No biases and no bias estimation	without ISL	0.17	0.62	0.15	0.67
	with ISL	0.11	0.51	0.07	0.53
Best possible		0.11	0.51	0.01	0.52

4.4.4 Influence of number of ground stations

After discussing the influence of station distribution, this section will now focus on another factor that could affect orbit determination accuracy: the number of ground stations. It is important to determine the optimal number of ground stations for achieving cost-effective performance. Fig. 4-12 displays five different ground networks with varying numbers of stations, ranging from one to sixty.

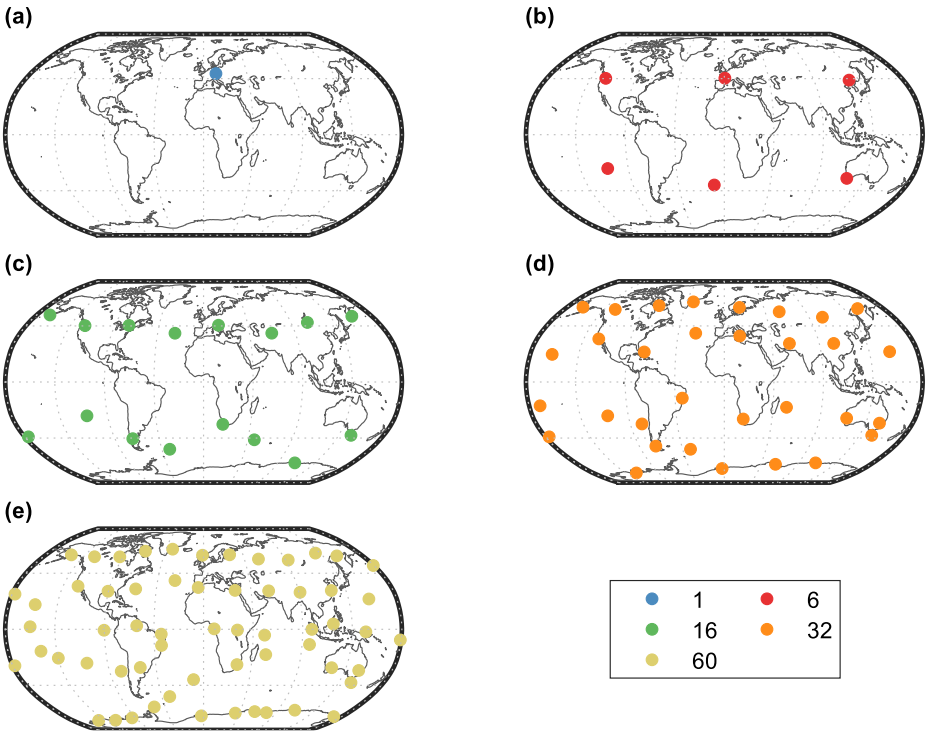

Fig. 4-12 Distribution of different number of ground stations for global networks: (a) 1, (b) 6, (c) 16, (d) 32 and (e) 60

Table 4-8 Mean RMS of orbit errors in radial, along-track, and cross-track directions, and 3D position for a global network [cm] (He et al., 2022)

Number of stations		Radial	Along-track	Cross-track	3D
1	without ISL	6.48	28.99	25.19	40.79
	with ISL	0.11	0.56	0.22	0.62
6	without ISL	0.16	0.62	0.15	0.66
	with ISL	0.11	0.52	0.08	0.54
16	without ISL	0.12	0.52	0.07	0.55
	with ISL	0.11	0.51	0.01	0.53
32	without ISL	0.12	0.52	0.05	0.54
	with ISL	0.11	0.51	0.05	0.53
60	without ISL	0.12	0.51	0.04	0.53
	with ISL	0.11	0.51	0.04	0.53
Best possible		0.11	0.51	0.01	0.52

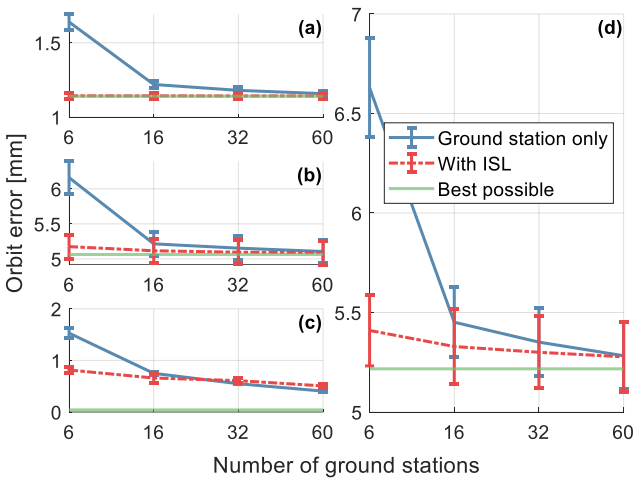

Fig. 4-13 Mean RMS of orbit errors with respect to the number of ground stations in (a) radial, (b) along-track, and (c) cross-track directions and (d) 3D position for global networks. Notify the different scales (He et al., 2022)

Fig. 4-13 illustrates the mean RMS of orbit errors for four networks (excluding the 1-station network) with and without ISL observations, in addition to ground stations. The error bars indicate the standard deviation of these RMS orbit errors over a period of seven days. Table 4-8 provides detailed values. The orbits show improvement as the number of ground stations increases when ISL observations are not present. The 3D mean RMS of orbit errors decreases from approximately 98% (for networks from 1-station to 6-station) to no significant changes (for networks from 32-station to 60-station). Increasing the number of stations becomes less effective in improving orbits when it exceeds sixteen.

The ISL observations have a significant positive impact on the orbits. This is particularly evident in the 1-station case, where radial and along-track orbit errors decrease to levels

comparable to those of the best possible solution. The 3D mean RMS of orbit errors for the 1-station network decreases by 98%, with only a marginal difference of 0.1 cm compared to the best possible solution. In fact, this accuracy level surpasses that achieved by the 6-station network without ISL observations. As more stations are added, even a small network of 6 stations with ISL observations can achieve similar orbit accuracy as larger networks with up to 32 or even 60 stations. These results demonstrate how beneficial ISL observations can be for improving orbit accuracy in small networks.

4.4.5 General comparison of distribution and number of stations

After discussing the effects of station distribution and number of stations individually, this section will now examine a more general scenario: comparing orbit errors between a regional network with a large number of stations and a global network with only a few. To illustrate this comparison, this section selects the European network as an example. Fig. 4-14 shows four different European regional networks, each with varying numbers of stations. For reference, the regional networks maintain the same number of stations as those in the global networks in Fig. 4-12.

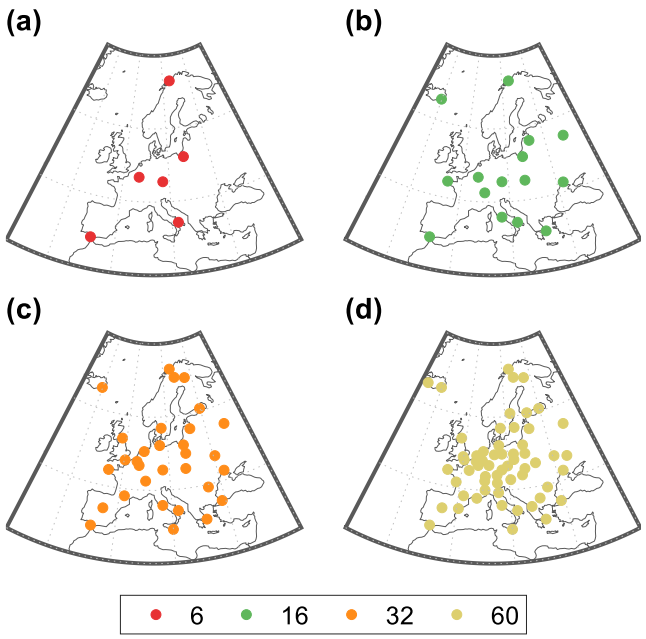

Fig. 4-14 Distribution of European regional networks with different number of ground stations: (a) 6, (b) 16, (c) 32 and (d) 60

Table 4-9 3D mean RMS of orbit errors for the networks with different number of stations [cm] (He et al., 2022)

Station distribution		6	16	32	60	Best possible
Global	without ISL	0.66	0.55	0.54	0.53	0.52
	with ISL	0.54	0.53	0.53	0.53	
Europe	without ISL	2.36	1.73	1.72	1.75	
	with ISL	0.59	0.59	0.59	0.59	

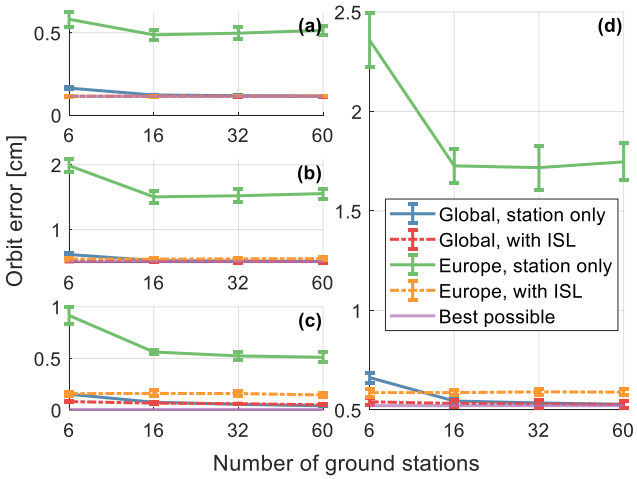

Fig. 4-15 Mean RMS of orbit errors with respect to the number of ground stations for 2 regions in (a) radial, (b) along-track, (c) cross-track directions and (d) 3D position. Notify the different scales (He et al., 2022)

Table 4-9 and Fig. 4-15 display the mean RMS of orbit errors for both European and global regions, with varying numbers of stations. Without ISL observations, the orbit gradually improves as the number of stations in both networks increases; however, this rate diminishes, and there is no significant improvement when the number exceeds 16. This aligns with the discussion in the section 4.4.4. Without the ISL observations, in radial, along-, and cross-track directions, even a European network consisting of 60 stations performs much worse than a global network comprising only 6 stations. The 3D mean RMS of orbit errors is approximately 1.7 times greater for the regional network with 60 stations. This finding confirms that station geometric distribution plays a more critical role, as previously mentioned in section 4.4.3.

By incorporating ISL observations, the orbit errors can be significantly reduced for the regional European network. The 3D mean RMS of orbit errors decreases from centimeter level to less than 0.6 cm. In fact, a regional network with only 6 stations and ISL observations can achieve even lower orbit errors compared to a global network without ISL observations. With ISL, a network of 6 stations is sufficient to determine the orbits, approaching the best possible solution. However, Table 4-9 shows that unlike a global network, adding more stations to a regional network with ISL observations does not further decrease orbit errors beyond a certain point due to geometric limitations in station distribution. As such, there remains an error gap of

approximately 12% compared to the best possible solution.

To summarize, adding more stations to a regional network can decrease orbit errors, but it is not as effective as implementing a global network. On the other hand, establishing ISL between satellites is highly beneficial in reducing orbit errors and can provide results similar to those of a global network solution.

4.4.6 Conclusions

This chapter examines how various ground networks and ISL observations affect the orbit determination of a LEO satellite constellation. The simulations are simplified yet take into account basic errors, including force model errors, instrumental errors, and measurement errors.

The first part of this study examines how the distribution of ground stations affects the accuracy of determined orbits. The study defines three regional networks, four quasi-global networks, and a global network consisting of six ground stations. Results indicate that, as expected, orbit errors decrease as the network becomes more global. Networks with high latitude locations produce larger orbit errors due to poor geometry compared to low or middle latitude networks. The geometry of the ground station distribution is more important than observation quantity for accurate orbit determination. Adding ISL observations improves orbit accuracy in all networks, making it comparable to the best possible solution. It is noteworthy that a regional network with ISL observations can produce smaller orbit errors than a global network without ISL. Bias estimation is also affected by station distribution and observation quantity plays an important role in improving satellite bias accuracy. This chapter concludes that precise calibration of satellite biases on ground is not necessary for accurate orbit estimation; estimating bias parameters together with orbital parameters produces equally accurate results as those without any biases in observations based on simulation results (6 global stations with/without ISL).

In this chapter, experiments are also conducted to examine the relationship between the number of stations and orbit errors. Five global networks with varying numbers of stations (ranging from 1 to a maximum of 60) are selected for analysis. The results indicate that without ISL observations, as more ground stations are used to determine orbits, the rate of improvement decreases. Additionally, there is little benefit in terms of orbit accuracy beyond using 16 stations. However, incorporating ISL observations can significantly reduce orbit errors, particularly for networks with fewer stations. In fact, using ISL observations in a 6-station network can yield nearly equivalent orbit accuracy compared to a 60-station network.

In the final section, four European networks are chosen to represent various station numbers in a regional network. The simulation results demonstrate that simply increasing the number of stations within one region does not significantly improve orbits. Surprisingly, a global network with only 6 stations outperforms a solution with 60 stations solely in Europe. However, by utilizing ISL observations, orbit errors can be reduced to the same level as those obtained from global networks.

4.5 ISL types

4.5.1 Introduction

Modern GNSS satellites are equipped with ISL technique to increase orbit accuracy and autonomy of the navigation system. This technique usually uses laser or microwave links to connect two satellites for communication and ranging. GPS, BDS, and Galileo have experimented, implemented and investigated with ISL to improve orbits as discussed in section 4.4.1. For example, Xie et al. (2020) investigated the orbit and clock accuracy of 18 BDS-3 MEO satellites and one GEO satellite using 43 days of ISL data. The results show that the orbit errors in radial direction are between 2-4 cm for MEO satellites and 8-10 cm for GEO satellites. While the Allan deviation of Ka-band clock is better than L-band clock when averaging interval longer than 5000 s. ISL can effectively help improving orbit determination for LEO mega-constellations with their large number of satellites as proven by Li et al. (2019b) and Michalak et al. (2021), as stated in section 4.4.1.

However, link topology differs between LEO and MEO GNSS satellites due to different orbit characteristics; topologies such as predefined sequence, ring, nearest, any-to-any are adopted for MEO GNSS satellites (Kur et al., 2020a; Schlicht et al., 2020; Xie et al., 2020), while typical LEO constellations like Iridium use the "4-connected" topology as mentioned in section 4.4.2. Moreover, there are also different types among the "4-connected" topology: intra-orbital links and inter-orbital links. The influence of each type on orbit determination is not yet been fully analyzed but will be discussed further in this chapter.

Meanwhile, to optimize the LEO satellite constellation for navigation, researchers studied its geometry and distribution. In some studies, a combined constellation consisting of two or more sub-constellations with different parameters is proposed (He & Hugentobler, 2018; Ge et al., 2020b; Ma et al., 2020). These parameters include orbital heights, inclinations, number of satellites, and number of orbital planes that may vary between sub-constellations. Combining sub-constellations with different heights and inclinations can significantly improve the uniformity of visible satellites and DOP around the globe (He & Hugentobler, 2018), as discussed in chapter 3. However, establishing ISL between these sub-constellations when using a combined constellation with satellites at different orbital heights has received little attention from researchers. This chapter aims to study and compare the influence of different types of inter-layer inter-satellite links (ILISL) on orbit determination.

4.5.2 Link topologies

As previously mentioned, the ISL at the same orbital height can be classified into two types: the intra-orbital link and the inter-orbital link. The intra-orbital links connect consecutive satellites on the same orbital plane, while the inter-orbital links connect two satellites on different orbital planes (Ferreira et al., 2002). Typically, the inter-orbital links are used to connect satellites in neighboring orbital planes. Fig. 4-16 provides an illustration of both intra- and inter-orbital links. Satellites with an intra-orbital link maintain a fixed relative position and

distance; therefore, their transmitters and receivers do not require steering. Conversely, due to the high variability in relative positions of satellites in different orbits, beam steering is necessary for inter-orbit links (Gvozdjak, 2000).

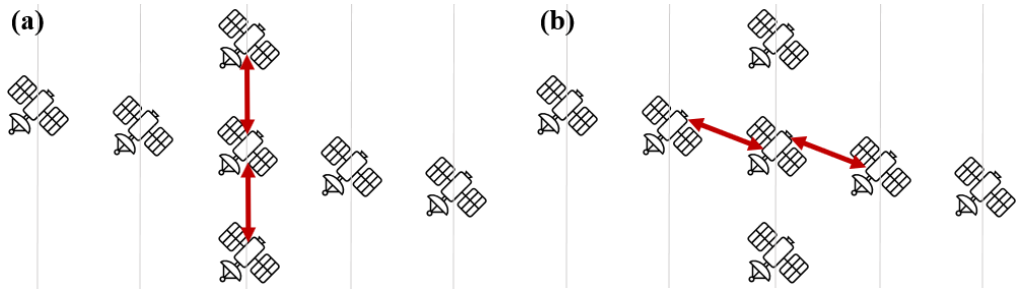

Fig. 4-16 Illustration of (a) intra-orbital link and (b) inter-orbital link

To enable a multi-layer constellation, the construction of ILISL is necessary. As the name suggests, ILISL connects satellites in different sub-constellations with varying orbital heights. Compared to a mono-layer constellation, ILISL can enhance satellite communication network performance significantly. However, it is also the most complex due to its higher dynamics. Limited resources on LEO satellites mean that each one can normally only use one steerable antenna for constructing an ILISL with other satellites. Additionally, as LEO satellites move rapidly and the geometry relationship between satellites changes frequently, ILISLs are formed and disconnected dynamically (Guo, 2009). Reconstructing any ILISL could cause the reconfiguration of the entire network topology along with the signal rerouting and the system resource reassignment (Wu et al., 2006). Therefore, reducing network reconstruction frequency while maintaining better orbit estimation is crucial. Generally speaking, there are three methods for selecting and establishing ILISL among satellites at different orbital heights (Wu et al., 2006; Guo, 2009):

1) Minimum distance method (nearest method). This method involves a satellite establishing ILISL with the nearest available satellite in another altitude. This is achieved by continuously estimating its distance to all viewable and available satellites in another altitude. If another satellite is closer than the current connected satellite, the link will immediately break and switch to the newly nearest one. Although this method ensures the shortest traveling path among satellites, it requires frequent ILISL reconstruction.

2) Maximum service time method (longest method). It involves a satellite establishing ILISL with the satellite in another altitude that offers the maximum service time, namely, the longest visible time. Once established, the ILISL holds until mutual visibility between satellites breaks. Only then will the satellite search for another available satellite in other altitudes that offers maximum service time. This approach minimizes the frequency of ILISL reconstructions but has a longer mean ILISL distance.

3) Weighted method. This method is a tradeoff between the minimum distance and

maximum service time methods where typically a cost function mediates both factors. One typical cost function can be written as:

$$C_{a,b} = w \cdot \frac{T_{a,b}}{T_{a,max}} + (1 - w) \cdot \frac{D_{a,min}}{D_{a,b}} \tag{4-1}$$

where $C_{a,b}$ denotes the cost of the link between satellite a and b at a certain epoch. Satellite a and b are in the different sub-constellations with different altitude, and here it is assumed that satellite a is searching for a possible link with satellites in other altitudes. w is the weight factor that takes value between 0 and 1. $T_{a,b}$ represents the remaining visible time between satellites a and b., whereas $T_{a,max}$ denotes the maximum remaining visible time of satellite a to all available satellites in another sub-constellation. Similarly, $D_{a,b}$ indicates the current distance between satellite a and b, while $D_{a,min}$ denotes the minimal distance between satellite a and all other available satellites in another sub-constellation. Satellite a will calculate the cost using equation (4-1) for all available satellites in other altitudes, and connect to the one with highest score. It constantly estimates the cost for every epoch, and switches the ILISL to a new satellite if it has a higher score than the current connected one. When $w = 0$, this method would effectively be the same as minimum distance method.

Other derived methods include the unified minimum distance method, unified maximum distance method, maximum resource method, and unified maximum resource method (Wu et al., 2006; Guo, 2009). However, these will not be discussed here. Interested readers may refer to the relevant references for more information. This chapter proposes two additional methods based on the three basic methods mentioned earlier:

4) Minimum distance till break method (nearest till break method). This method is similar to the minimum distance method. A satellite will connect to its nearest available satellite in another altitude. However, unlike the minimum distance method, this connection will not break even if there is another closer satellite at a later epoch. The ILISL will only break when the two satellites are no longer visible to each other.

5) Weighted till break method. This method uses the same cost function as equation (4-1). However, instead of continuously monitoring other satellites, a satellite will stay connected with its current linked satellite until the visibility vanishes. Only then will satellite a start looking for a possible connection with other available satellites in another altitude. When $w = 1$, this method would effectively be the same as maximum service time method.

This chapter discusses and compares these five methods in detail.

4.5.3 Intra- and inter-orbital links

This section discusses the impact and influence of intra- and inter-orbital links on orbit determination. While the inter-orbital link is sensitive to both along-track and cross-track movements, the intra-orbital link primarily detects along-track movements. Therefore, it is

important to examine how different ISLs affect orbit determination.

The simulation settings remain the same as in Table 4-4, except for the estimation of empirical parameters at different frequencies. In the along-track direction, one constant and two periodic parameters are estimated every 4 h, while in the cross-track direction, these three parameters are estimated every 8 h.

First, this section examines the geometry distribution of satellites and links. In Fig. 4-17, one can see the nadir view of one LEO satellite to other satellites and formed links for different epochs. This constellation allows a satellite to observe only two neighboring satellites in the same orbital plane: one forward and one backward. Their relative position remains fixed, resulting in constant intra-orbital links. However, satellites in other orbital planes move relatively around this satellite with observations being interrupted by Earth or out of sight or they are not the field of view anymore.

In Fig. 4-18, one can observe the movement of satellites in one of the neighboring orbital planes where they move in an "8" shape pattern. The closer the neighboring satellite is, the larger its "8" shape becomes. For the closest satellites within this constellation, a permanent link can be established without interruption from Earth.

Since two satellites with intra-orbital links do not change their relative positions much, in the following the relationships between the satellites in the neighboring orbital planes will be elaborated.

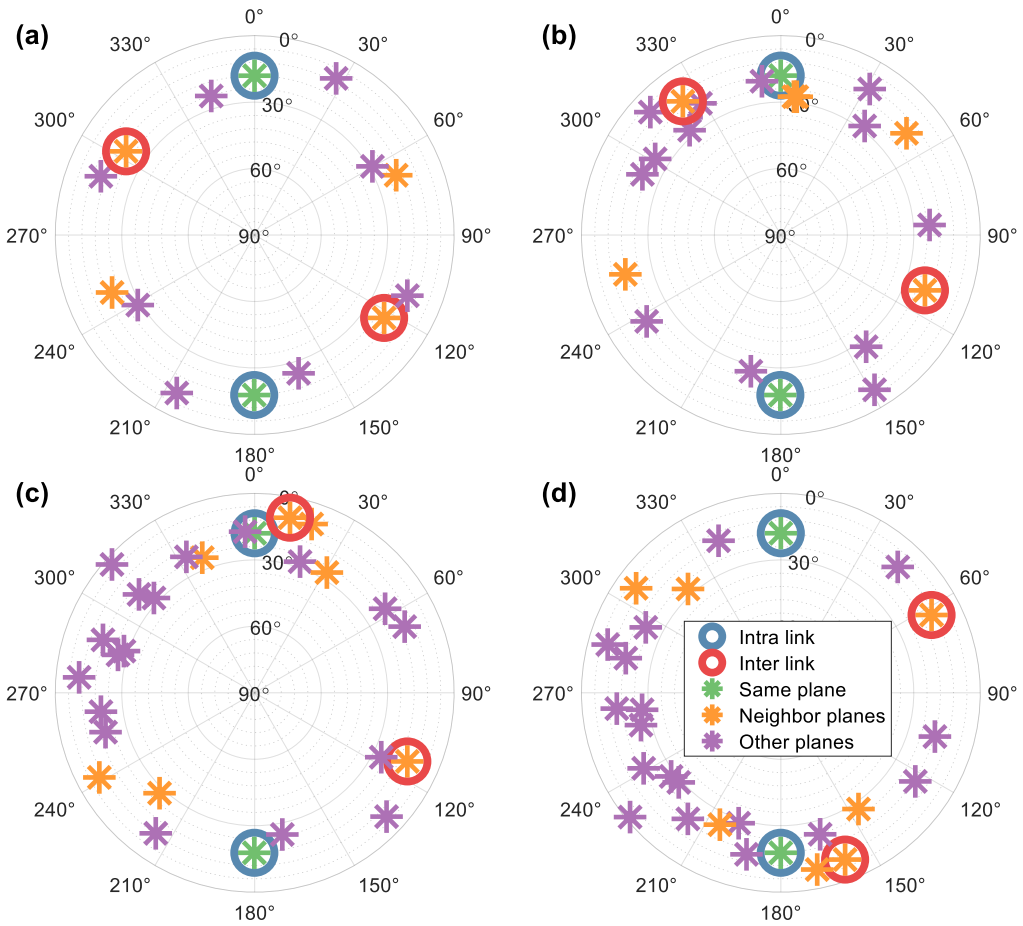

Fig. 4-17 Polar plot of the nadir view of a satellite to other satellites at different epochs: (a) initial position, (b) after 10 min, (c) after 20 min and (d) after 30 min. The angle and radius of the circle represent the relative azimuth and relative elevation angle of the satellites to this satellite, respectively. Different colors of stars represent satellites in different categories of orbital planes. Different colors of circles represent different ISL types

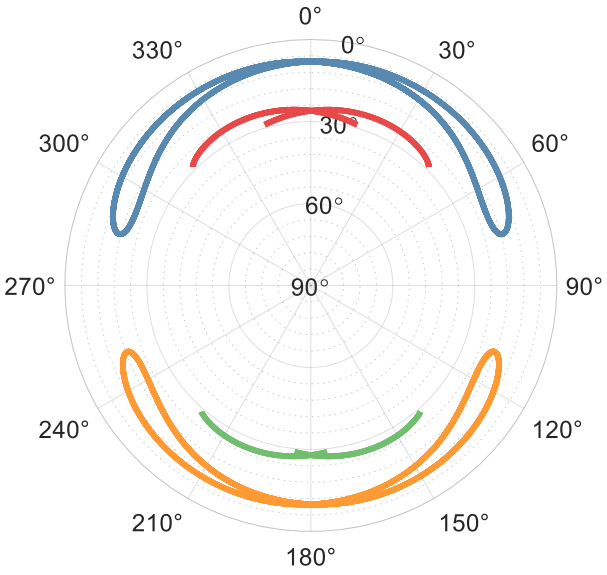

Fig. 4-18 Polar plot of the nadir view of a satellite to the satellites in one of the neighboring orbital planes. Different color indicates different satellites. The lines indicate the movement of the satellites

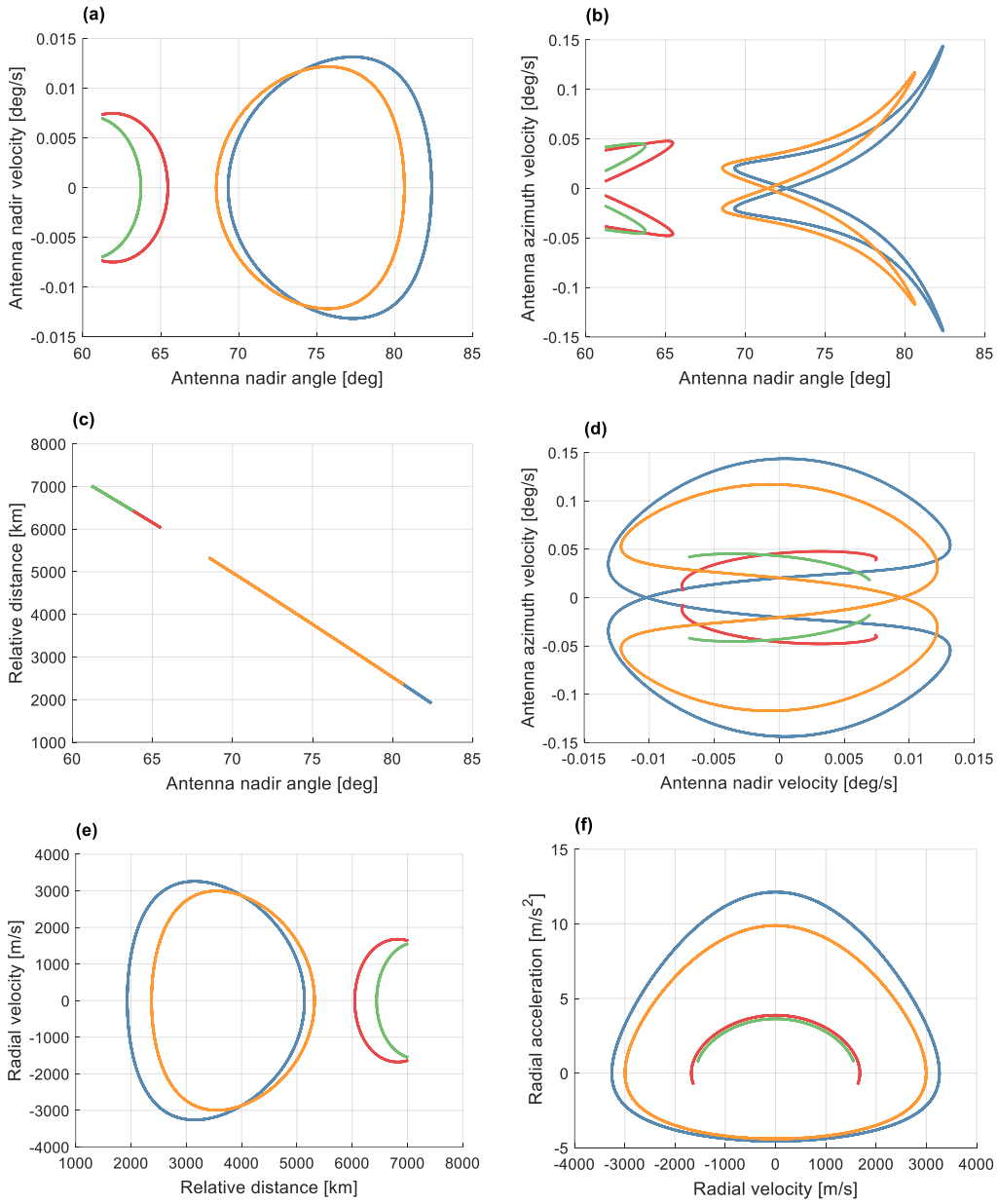

Fig. 4-19 Relationship between 2 parameters from one satellite to satellites in one of the neighboring orbital planes: (a) antenna nadir angle vs. antenna nadir velocity; (b) antenna nadir angle vs. antenna azimuth velocity; (c) antenna nadir angle vs. relative distance; (d) antenna nadir velocity vs. antenna azimuth velocity; (e) relative distance vs. radial velocity and (f) radial velocity vs. radial acceleration. Different color indicates different satellites

Fig. 4-19 displays the relationship between various parameters in the connection of two satellites. In Fig. 4-19 (a), it is evident that as satellites move farther apart, the nadir angle typically falls within a range of 65-70°. For closer satellites, when the nadir angle exceeds or falls below this range, the nadir velocity increases. The maximum nadir velocity occurs at extreme values of the nadir angle. Similarly, Fig. 4-19 (b) shows that larger azimuth velocities correspond to larger nadir angles.

Fig. 4-19 (c) illustrates that as two satellites approach each other, their nadir angle

increases. Additionally, Fig. 4-19 (d) depicts how changes in azimuth and nadir velocities resemble the relative satellite movement in an "8" shape pattern. Using the satellite in blue color as an example, when two satellites come closest, the nadir velocity becomes zero while the azimuth velocity is at its absolute maximum value.

As two satellites move closer together, i.e. their relative distance becomes smaller, one can see from Fig. 4-19 (e) that the radial velocity becomes larger. When the two satellites pass over each other, the sign of radial velocity is reversed. Similarly, as Fig. 4-19 (f) shows, when their relative distance becomes largest, the radial velocity is zero. In other words, they would no longer be moving against each other. At this point, their radial acceleration also reaches its largest value to pull them toward each other.

The figures in Fig. 4-20 follow the same pattern as those in Fig. 4-19, but with additional information. The colormap in each figure displays the frequency of epochs during which corresponding values occurred over a period of time, indicating the most common parameter pairs. Brighter blocks indicate longer periods where parameters remain at specific values. For instance, brighter blocks in Fig. 4-20 (e) suggest that satellites tend to maintain maximum relative distance for extended durations due to their slower relative movement caused by smaller radial velocity - aligning with expectations.

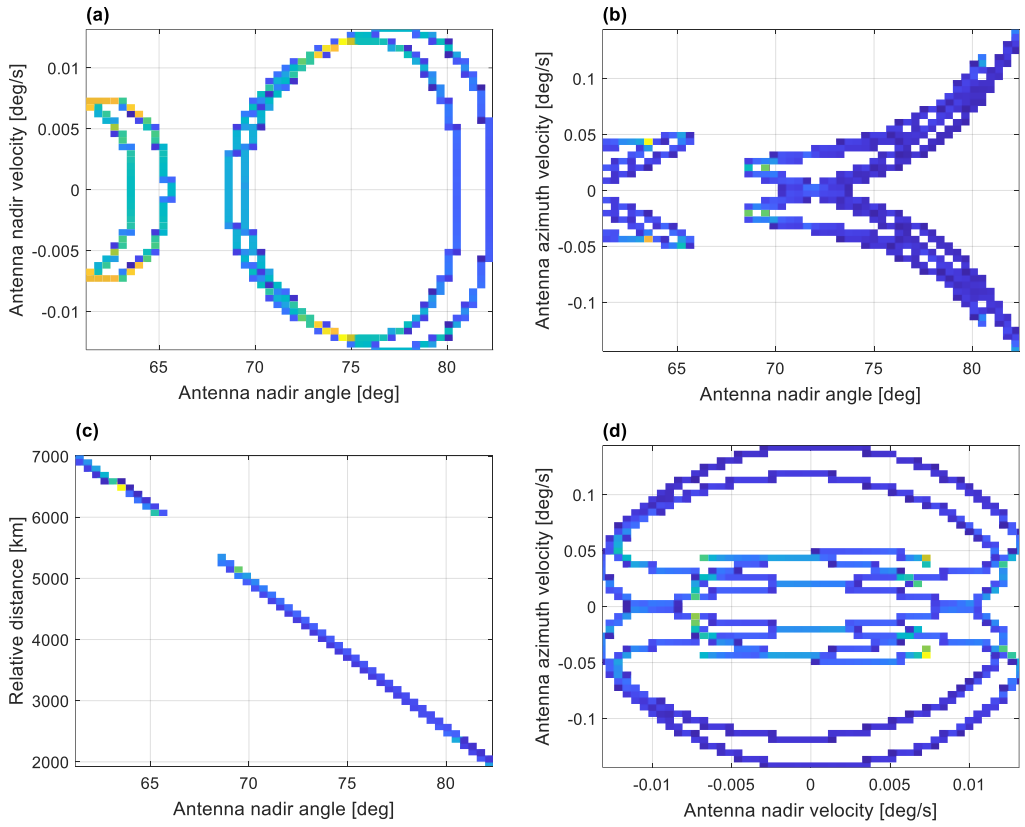

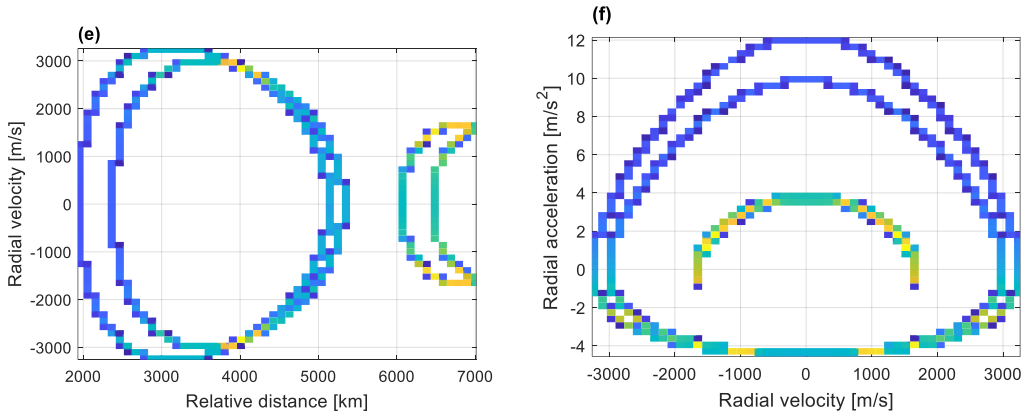

Fig. 4-20 2D histogram of the relationship between 2 parameters from one satellite to satellites in one of the neighboring orbital planes: (a) antenna nadir angle vs. antenna nadir velocity; (b) antenna nadir angle vs. antenna azimuth velocity; (c) antenna nadir angle vs. relative distance; (d) antenna nadir velocity vs. antenna azimuth velocity; (e) relative distance vs. radial velocity and (f) radial velocity vs. radial acceleration. The color represents the frequency that the corresponding values fall into the certain block. The brighter the color of the block is, the higher chance that the parameters get the corresponding values

After discussing the geometry of intra- and inter-orbital links, now this section investigates their contribution to orbit determination. Table 4-10 provides a summary of the benefits of ISL for orbit determination. The ISL is using "4-connected" topology with two intra-orbital links and two inter-orbital links as described in section 4.4.2. Two station cases are selected with 1 and 16 global stations from Fig. 4-12, noting differences in orbit error values compared to Table 4-8 due to different estimation settings for empirical parameters.

In this scenario, more frequent estimation of empirical parameters renders the one-station-only case unsolvable; however, ISL can help determine orbits with much fewer stations like this case while still achieving accurate results. Specifically, 3D orbit errors are 40% smaller than those obtained through a 16-station-only case. Comparing cases with and without ISL for 16 stations further confirms that ISL reduces orbit errors in all three directions but especially along- and cross-track directions.

Table 4-10 Mean RMS of orbit errors in radial, along-track, and cross-track directions, and 3D position for a global network [cm]

Number of stations		Radial	Along-track	Cross-track	3D
1	without ISL	-	-	-	-
	with ISL	0.03	0.09	0.07	0.12
16	without ISL	0.06	0.15	0.11	0.20
	with ISL	0.03	0.06	0.04	0.08

Table 4-11 displays the orbit determination results obtained using different ISL types in a simulation where only one ground station is used to minimize the influence of other

observations and fully explore the potential of different ISL types. The inter-orbital link outperforms the intra-orbital link in all three directions, particularly in the cross-track direction. While the intra-orbital link can detect and model orbital plane shape well since it observes satellites within the same orbital plane, it performs poorly regarding orientation accuracy of orbital planes in space, resulting in lower accuracy for cross-track direction. In contrast, by connecting satellites from different orbital planes with relative movements between them, inter-orbital links obtain observations that change along all three directions leading to more favorable orbit determination outcomes than intra-orbital links. Inter-orbital links can reduce orbit errors from centimeter level to millimeter level. Combining both intra- and inter-orbit links further decreases along- and cross-track direction orbit errors by approximately 25% and 22%, respectively compared to using only inter-orbit links.

Table 4-11 Mean RMS of orbit errors in radial, along-track, and cross-track directions, and 3D position for different ISL types [cm]

ISL types	Radial	Along-track	Cross-track	3D
Intra-orbital links	0.04	0.42	73.33	73.33
Inter-orbital links	0.03	0.12	0.09	0.16
"4-connected"	0.03	0.09	0.07	0.12

4.5.4 Comparison of ILISL strategies

When a mega-constellation consists of multiple layers, establishing ISL between these layers requires the use of ILISL. Section 4.5.2 highlights various strategies for scheduling ILISL, each with its own strengths and weaknesses. This section will discuss the influence of five methods on orbit determination, which are previously introduced in detail.

This simulation uses the multi-layer constellation selected in chapter 3, but only about half of the original constellation is used to reduce computation burden, like in chapter 4.4. Specifically, this section focuses on a multi-layer LEO constellation with an orbital height of 900 km and Walker Delta 73°: 90/9/1, as well as an orbital height of 700 km and Walker Delta 38°: 91/7/1. The other simulation settings remain unchanged from section 4.5.3.

It should be noted that for both the weighted method and "weighted till break" method, a weight factor w in equation (4-1) must first be defined. To investigate the impact of this factor on orbit determination, this section assigns values of w ranging from 0.2 to 0.8.

To better understand the geometry of these methods, refer to Fig. 4-21 which shows the nadir view of one LEO satellite to other satellites in another sub-constellation and the formed links for different epochs. Among all visible satellites, satellite No. 90 is the closest at the initial epoch while satellite No. 102 has the longest visibility from that point on.

For the first 30 minutes, both the "nearest till break" and "weighted till break" methods with weight factors of $w = 0.2$, $w = 0.4$ and $w = 0.6$ share the same link as marked by blue circles in Fig. 4-21. Similarly, the longest method selects the same satellite as weighted

method with $w = 0.8$ and $w = 1.0$ as well as "weighted till break" method with $w = 0.8$; these links are marked by green circles. At the initial epoch, satellite No. 90 is much closer than any other satellites in this layer; therefore except for the longest method and both weighted methods with a weight factor higher than 0.8 which weigh more towards longer contact time, all other methods select satellite No. 90 to establish a link. After a few epochs when satellites move around, the nearest method along with the weighted method having smaller weight factors continuously monitor the motion of all other satellites and frequently breaking and reconnecting links with others, whereas the "nearest till break" method and "weighted till break" method stick to the original selection i.e., satellite No. 90.

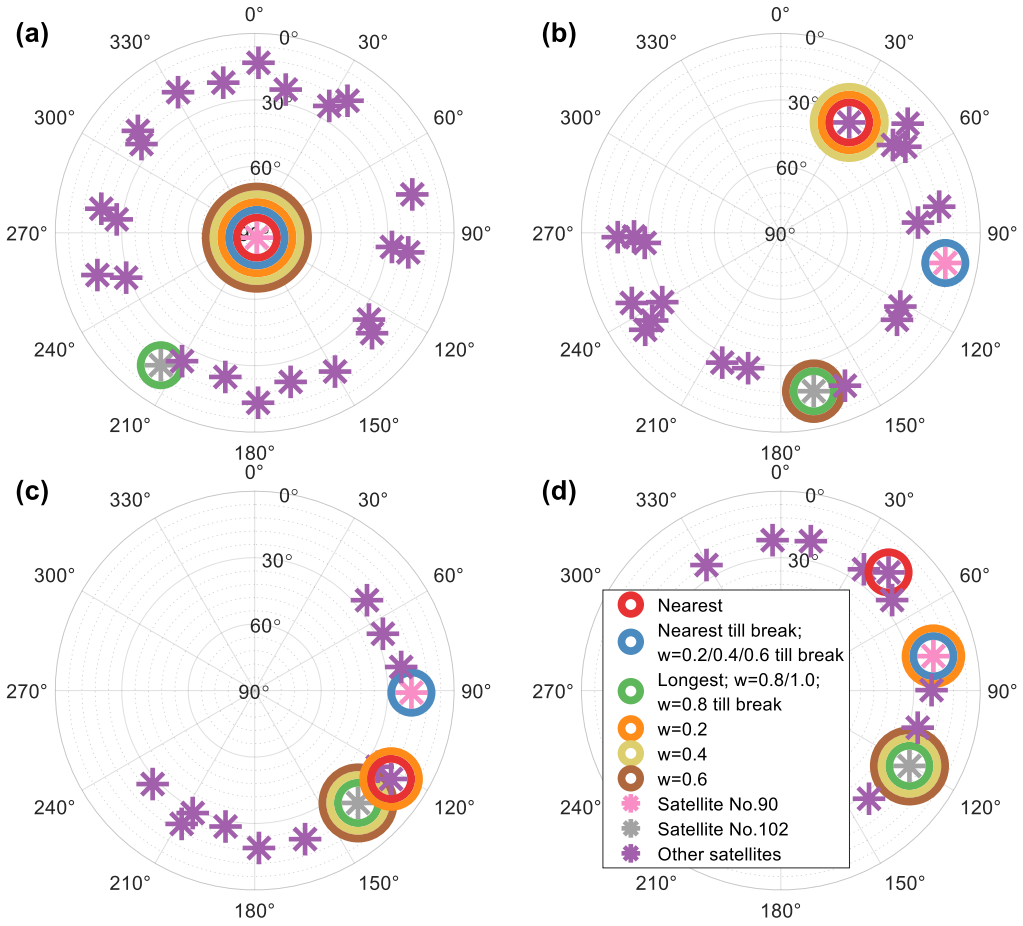

Fig. 4-21 Polar plot of the nadir view of a satellite to other satellites in another layer at different epochs: (a) initial position, (b) after 10 min, (c) after 20 min and (d) after 30 min. The angle and radius of the circle represent the relative azimuth and relative elevation angle of the satellites to this satellite, respectively. Different colors of stars represent satellites in different categories. Different colors of circles represent different ILISL types

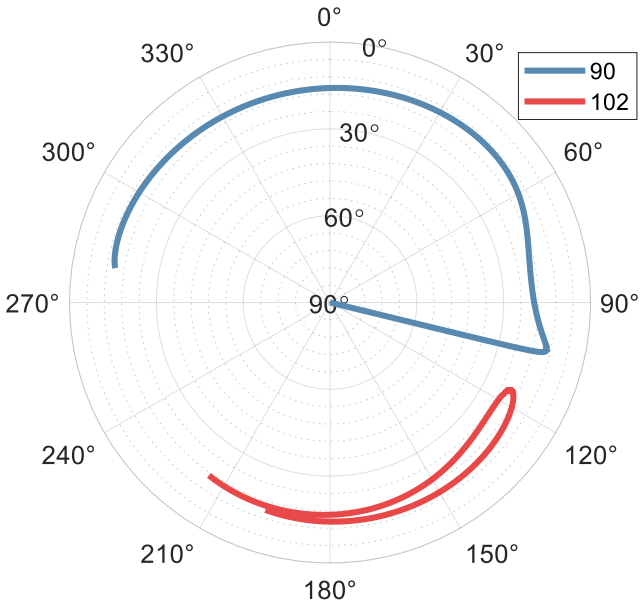

Fig. 4-22 Polar plot of the nadir view of a satellite to the satellites in another layer. Different color indicates different satellites. The lines indicate the movement of the satellites in 1 h

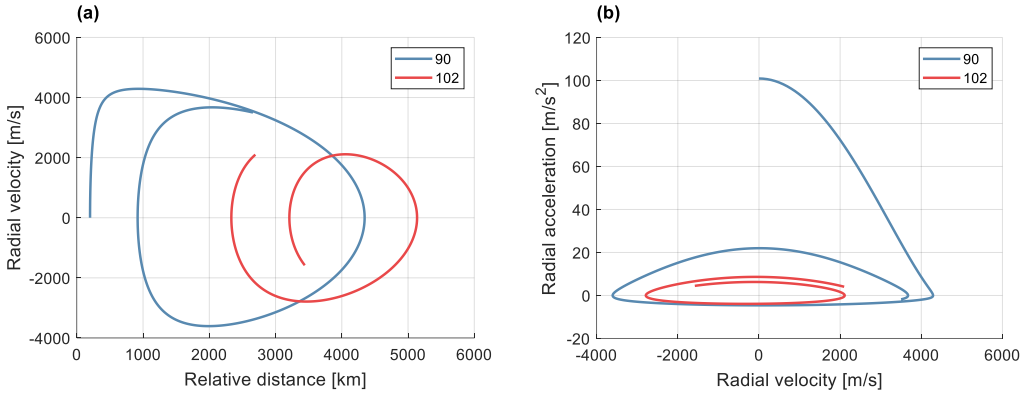

Fig. 4-23 Relationship between 2 parameters from one satellite to satellites in another layer: (a) relative distance vs. radial velocity and (b) radial velocity vs. radial acceleration. Different color indicates the movement of different satellites in 1 h

Fig. 4-22 displays the motion of satellite No. 90 and No. 102 relative to this satellite. Their different altitudes result in varying rotating velocities around the Earth. Consequently, this causes an irregular trace pattern on the nadir view compared to satellites in the same plane as shown in Fig. 4-18. It might be interesting to also mention that the revolution period for the satellites at the higher altitude is about 1.7 h, while this value is about 1.6 h for satellites at the lower altitude. This means that it will take a long time to repeat the period. In Fig. 4-23, one can observe a similar relationship between different parameters regarding the connection between two satellites as seen in Fig. 4-19; specifically, when two satellites move closer together, their radial velocity increases, while it decreases to zero and radial acceleration reaches its maximum value when they are at their furthest distance apart from each other.

However, due to differences in speed of motion among these satellites, this pattern is not fixed like that shown in Fig. 4-19. Specifically, for the closest satellite No. 90, it gradually moves further away. The relative distance gradually increases from approximately 200 km to around 918 km when the radial velocity changes the sign again. Conversely, satellite No.102 has the longest contact time and gradually moves closer to this satellite; when the radial velocity reverses the sign again, their relative distance decreases from about 3208 km to roughly 2332 km providing them with more connecting time compared to other satellites.

Table 4-12 gives the average number of ILISL observations per day, indicating that higher weight factors generally result in more observations. Nevertheless, the difference is minimal, with the largest discrepancy being less than 1500 observations - equivalent to only 1% of total ILISL observations.

Table 4-12 also presents the orbit errors obtained using different ILISL strategies. Compared to the case without ILISL, the 3D orbit errors decrease by approximately 46% to 73%. The radial and along-track directions show a more significant reduction in orbit errors of over 57% and 52%, respectively.

Fig. 4-24 provides a clearer comparison of the ILISL strategies, with the blue line representing the "instant break" strategy or weighted method discussed in section 4.5.2, where links break when there is another satellite with a higher weighting score than the current one. When $w = 0$, this strategy is the same as the minimum distance method (nearest method). Note that this strategy is not equivalent to the maximum service time method (longest method) when $w = 1$, because if another satellite comes into view with possible longer connection time, it will replace the old one even if the old one is still visible. This does not accord with the definition of the longest method. The red line represents the "connect till break" strategy or the "weighted till break" approach. This strategy is equivalent to the "nearest till break" method for $w = 0$ and becomes the longest method for $w = 1$.

It is evident that for orbit determination, regardless of the weight factor value, the "instant break" strategy outperforms the "connect till break" strategy. More specifically, different weight factors do not significantly affect the orbit accuracy under the "connect till break" strategy. The orbit errors stay around 0.4 cm. However, generally speaking, smaller weight factors lead to better results under the "instant break" strategy. The orbit errors increase almost linearly as the weight factor exceeds 0.4. A weight factor increase of 0.2 results in a 3D orbit error increase of approximately 0.05 cm. The "instant break" strategy with $w = 0.2$ yields minimal 3D orbit errors.

Table 4-12 Average number of ILISL observations and mean RMS of orbit errors in radial, along-track, and cross-track directions, and 3D position for different ILISL types

ILISL types	Average number of ILISL observations per day	Orbit errors [cm]			
		Radial	Along-track	Cross-track	3D
None	-	0.23	0.63	0.28	0.74
Nearest	125359	0.07	0.15	0.11	0.21
Nearest till break	125435	0.10	0.30	0.23	0.40
Longest	125795	0.10	0.30	0.23	0.40
$w = 0.2$	125155	0.07	0.15	0.10	0.20
$w = 0.4$	125754	0.07	0.16	0.11	0.21
$w = 0.6$	126006	0.08	0.20	0.13	0.26
$w = 0.8$	126469	0.09	0.24	0.18	0.32
$w = 1.0$	126641	0.10	0.28	0.20	0.36
$w = 0.2$ till break	125456	0.10	0.30	0.23	0.40
$w = 0.4$ till break	125518	0.10	0.30	0.24	0.40
$w = 0.6$ till break	125583	0.10	0.30	0.23	0.40
$w = 0.8$ till break	125788	0.10	0.30	0.23	0.40
Best possible	-	0.07	0.13	0.01	0.14

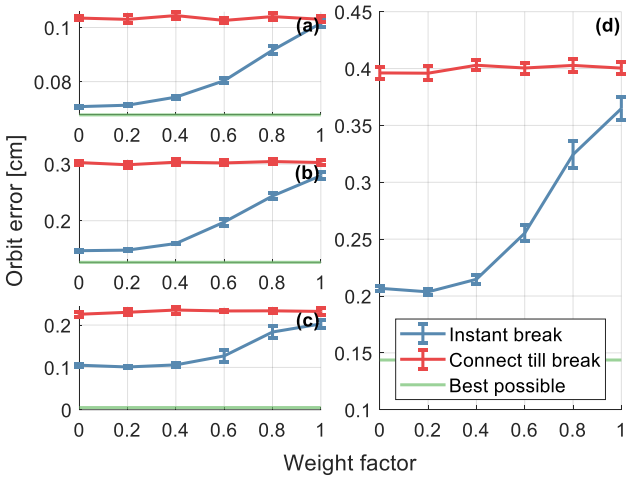

Fig. 4-24 Mean RMS of orbit errors with respect to the weight factor in (a) radial, (b) along-track, (c) cross-track directions and (d) 3D position. Notify the different scales

4.5.5 Conclusions

This chapter examines how various types of ISLs affect the orbit determination of LEO satellite constellations. Specifically, it provides a detailed definition of ILISL, a unique type of ISL that connects satellites at different orbital heights.

The first part of the study examines two types of links for satellites at the same altitude.

The geometry of these links reveals that intra-orbital links can be established permanently and does not move since there is no relative motion between satellites in the same orbital plane. On the other hand, inter-orbital links can also be formed permanently, but neighboring planes' satellites move in an "8" shape. Additionally, this study investigates various parameters such as nadir angle, nadir velocity, azimuth velocity, relative distance, radial velocity and radial acceleration to understand their relationship with each other. The orbit determination results show that additional ISL observations help solve unsolvable cases due to few stations and observations with sufficient orbit accuracy. Because the intra-orbital link has limited sensitivity about the motion in the cross-track direction, its determined orbits are much worse than those from the inter-orbital link solutions. Therefore, if there is a limited number of links available for orbit determination purposes, using the inter-orbital link would be more favorable as it reduces 3D orbit errors to mm-level compared to over 70 cm 3D orbit errors from the intra-orbital link solutions.

A LEO mega-constellation typically consists of multiple sub-constellations. To connect the entire constellation and supplement orbit determination observations from a new perspective, ILISL is an effective method. Unlike intra- and inter-orbital links, ILISL cannot be held permanently due to varying satellite speeds at different orbital heights. Therefore, continuous monitoring and link adjustments are necessary for ILISL. This raises questions about the optimal strategy for link connections. This study evaluates three classical methods and two variant methods to validate their effect on orbit determination. Various weight factor values are also tested for the weighted method and "weighted till break" method.

The changes in each strategy over time are observed through nadir views from a satellite to those at lower altitudes. Meanwhile, the geometry of the closest satellite and longest contact satellite is also discussed. The relationship between different parameters of two satellites indicates similar but drifting shapes compared to those from inter-orbital links. Orbit determination results demonstrate that ILISL improves orbit accuracy by more than 46%, particularly in the radial and along-track directions. Among all methods tested, applying the "instant break" strategy results in smaller orbit errors while adopting the "connect till break" strategy leads to relatively larger errors that remain consistent regardless of weight factor changes. On the other hand, with a higher weight factor, orbits estimated by the "instant break" strategy worsens. The minimal orbit errors occur when using an "instant break" strategy with a weight factor of 0.2.

4.6 Data weighting

4.6.1 Introduction

The development of new technologies, such as ISL, has led to the involvement of multiple types of observations in satellite orbit determination. However, combining these data requires careful attention due to their varying characteristics and accuracies. Incorrect weighting can negatively impact the accuracy of determined orbits. To address this issue, VCE is commonly used to determine the weight of combined data (Koch & Kusche, 2002). VCE has been widely applied

in geodesy for gravity field modeling (Klees et al., 2008; Jean et al., 2018) and GNSS multi-frequency data processing (Tiberius & Kenselaar, 2003; Li, 2016; Chang et al., 2018).

Several studies have demonstrated the benefits of using VCE algorithms when combining ground range observations with ISL observations (Kur et al., 2020b; Zhang et al., 2021). In a subsequent study by Kur and Liwosz (2022), they evaluated Galileo satellite orbit determination with additional ISL observations and concluded that VCE helps minimize orbit errors by up to 20% without affecting clock accuracy. The Förstner and Helmert VCE methods perform similarly regarding orbit estimation. Additionally, this study also discusses the advantages of using VCE for bias estimation.

The methodology and VCE methods used in this chapter are previously introduced in chapter 2.5. In the following sections, the VCE of equation (2-31) is referred to as the rigorous algorithm, while equation (2-33) is called the simplified algorithm. This chapter's simulation study examines how well VCE performs in determining LEO satellite orbits. Specifically, this chapter investigates the need for data weighting with multiple types of observations, compares different algorithms' efficiency and accuracy, and analyzes how modeling errors affect VCE results.

To ensure consistency, the orbit simulation settings remain unchanged from Table 4-4. In summary, a Walker Delta constellation consisting of 90 satellites is chosen. The measurement generation uses a "4-connected" link topology and six global stations as shown in Fig. 4-12. One deviation from previous studies is that this chapter uses a higher noise level of 5 cm for ground range measurements to fully analyze the impact of VCE, which has also been used in other studies (Michalak et al., 2021). The noise level for ISL measurements keeps the same as previous studies in this work, namely 1 mm.

To avoid the influence of model errors, the same atmosphere model as the original one is used for estimation in sections 4.6.2 and 4.6.3. The impact of systematic errors is discussed in section 4.6.4. Additionally, only six initial state parameters and biases are estimated in sections 4.6.2 and 4.6.3. The impact of empirical parameters will also mention in section 4.6.4. For more detailed information on the estimation settings, please refer to Table 4-13.

Table 4-13 Estimation settings

Arc length	1 d	
Initial state error	Random ±3 mm for position, ±3 μm/s for velocity	
Data weighting	According to the scenarios	
Force models	Earth gravity field	EIGEN 6S 60×60 (Förste et al., 2011)
	Air drag	DTM-2000 atmosphere model (Bruinsma et al., 2003)
Parameters	Initial state vector, and biases for LEO satellites and stations	

4.6.2 Comparison of data weighting algorithm

First, this section examines the impact of data weighting on the orbit accuracy and evaluates the efficacy of simplified and rigorous VCEs. Table 4-14 presents the RMS values for orbit errors and data weighting obtained using different weighting algorithms, averaged over a period of seven days. The estimated satellite orbits are compared to true orbits to calculate these errors.

Table 4-14 Mean value of RMS of orbit errors and data weighting. The weighting in the last column means the true or computed weighting for the two measurement types

Data weighting algorithm	RMS of orbit errors [cm]				Weighting σ_{range}: σ_{ISL} [mm]
	Radial	Along-track	Cross-track	3D	
Fixed 1:1	0.019	0.376	0.323	0.533	1:1
Fixed 20:1	0.001	0.123	0.135	0.199	20:1
Fixed 30:1	0.001	0.102	0.119	0.170	30:1
Fixed 50:1	0.001	0.097	0.114	0.162	50:1
Simplified VCE	0.001	0.097	0.114	0.162	49.90:1.00
Rigorous VCE	0.001	0.097	0.114	0.162	50.00:1.00

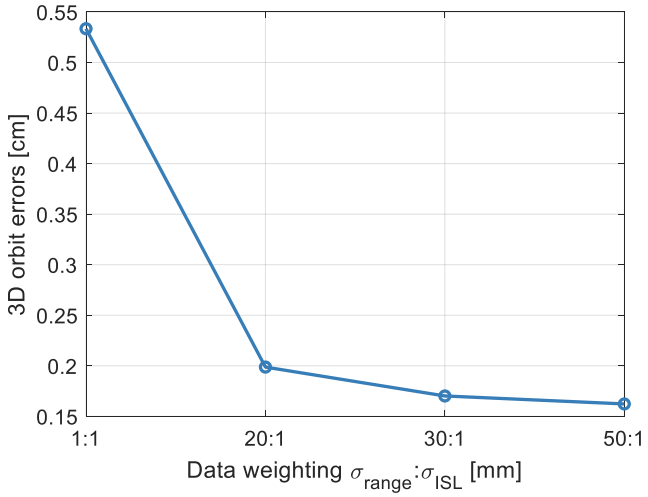

Fig. 4-25 Mean value of RMS of 3D orbit errors with respect to different weighting

When both types of observations are not weighted correctly, it can lead to inaccurate estimated orbits. For instance, in Table 4-14, the first row assigns an equal fixed weight to ground range and ISL measurements. This is incorrect because these measurements have different accuracies. In comparison to the correct weighting (the fourth row of Table 4-14), orbit errors increase by 95%, 74%, 65%, and 70% in radial, along-track, cross-track directions, and 3D position respectively. Fig. 4-25 provides an overview of the RMS of 3D orbit errors with respect to different data weighting. It shows that as the data weighting approaches the correct value, orbit errors decrease.

The final two rows of Table 4-14 demonstrate the effectiveness of VCE. Both VCE algorithms accurately determine the weighting of two types of observations, maintaining orbit accuracy at the same level as correctly fixed weighting. While the rigorous VCE algorithm determines a weighting closer to the real noise level of each measurement type, this slight difference does not impact satellite orbit determination accuracy.

4.6.3 Efficiency of two VCE algorithms

Having proven the effectiveness of the VCE algorithms, now this section focuses on the comparison between these two algorithms. To determine how different constellation sizes affect the computation burden of VCE calculations, three more scenarios are chosen by varying the number of satellites in the constellation from 90 to 30, 60, and 120. It should be noted that a link cannot theoretically be established for a constellation with only 30 satellites due to the large argument of latitude between neighboring satellites in the same orbital plane. However, a "4-connected" link topology is still adopted for consistency across all constellations. This section aims to compare the computational efficiency of two algorithms, which means that the number observations (or the number of satellites) matters. The impact of link topology on the conclusion is minimal. Table 4-15 summarizes the RMS of 3D orbit errors and VCE computation time for each scenario. The simulations are conducted using the software running on a Linux cluster with 24 cores @2.6 GHz and 58 GB RAM.

Table 4-15 Mean value of RMS of orbit errors and VCE computation time

Number of satellites	Simplified VCE		Rigorous VCE	
	RMS of 3D orbit errors [cm]	VCE computation time [ms]	RMS of 3D orbit errors [cm]	VCE computation time [ms]
30	0.39	2.64	0.39	329.22
60	0.16	4.58	0.16	2997.59
90	0.16	6.48	0.16	10121.73
120	0.10	9.73	0.10	27207.77

Table 4-15 shows that the simplified VCE algorithm significantly reduces computation time compared to the rigorous VCE algorithm, without degrading orbit errors. Even with 120 satellites, the simplified algorithm takes less than 10 ms to compute, while it takes over 300 ms for the rigorous algorithm to compute only 30 satellites and more than 27 s for 120 satellites. As more satellites are added to the constellation, the computation time of the simplified algorithm increases by only about 73%,145%, and 269% respectively, whereas for the rigorous algorithm it increases by about 8 times, 30 times and 82 times respectively. This can be explained from equation (2-31) and (2-32). An increase in satellite numbers leads to an increase in estimated parameters which results in a larger normal matrix $\boldsymbol{N}$ requiring much more time for computing its inverse $\boldsymbol{N}^{-1}$ and the trace term $tr(\boldsymbol{N}_i\boldsymbol{N}^{-1})$ of equation (2-32). However, since the number of observations of each type is much greater than the number of estimated parameters, omitting this trace term does not significantly affect computation time for the

simplified algorithm as opposed to the rigorous one.

For a constellation of 30 satellites, the simplified algorithm is about 124 times faster. If the constellation contains more satellites, this ratio increases as the third power of the number of satellites, as shown in Fig. 4-26. This is because calculating the inverse of a matrix and matrix-matrix multiplication has a computational complexity of $O(n^3)$. Here n is the number of unknown parameters. With more satellites, the curve becomes even more distant from the curve of the cubic function because the computation time of other operations also increases. In the future, with thousands of LEO satellites in space, the advantages of this simplified algorithm would be much more appealing.

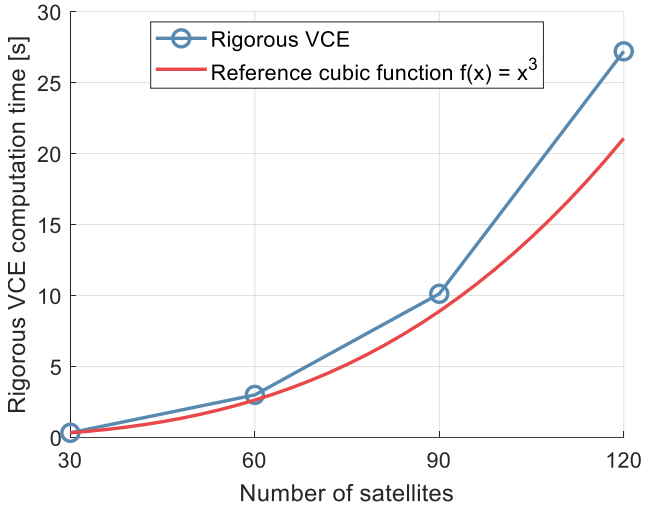

Fig. 4-26 Rigorous VCE computation time with respect to the number of satellites

4.6.4 Impact of modeling errors on VCE

In previous discussions, the impact of modeling errors is not taken into account. However, force model errors are present in most real-world applications. This raises the question of how modeling errors would affect data weighting and whether VCE is still applicable. The following section will provide a detailed discussion on this matter.

Table 4-16 presents three tested scenarios, while other settings remain unchanged from the ones mentioned earlier. Scenario 1 is the original scenario used in previous studies. Scenarios 2 and 3 intentionally use a different reference atmospheric model than the true model to simulate force model errors. In scenario 3, in addition to the initial state vector and biases, empirical acceleration parameters are estimated every 4 h in the along-track direction and every 8 h in the cross-track direction, similar to chapter 4.5. The outcomes of these tests are displayed in Table 4-17.

Table 4-16 Overview of different scenarios

	Scenario 1	Scenario 2	Scenario 3
True air drag model	DTM-2000 atmosphere model (Bruinsma et al., 2003)		
Reference air drag model	DTM-2000 atmosphere model (Bruinsma et al., 2003)	Modified Harris-Priester atmosphere model (Montenbruck & Gill, 2000, pp. 89-91)	
Estimated parameters	Initial state vector, and biases for satellites and stations		Initial state vector, empirical accelerations, and biases for satellites and stations

Table 4-17 Mean value of RMS of orbit errors and data weighting. The weighting in the last column means the true or computed weighting for the two measurement types

Scenario	Data weighting algorithm	RMS of orbit errors [cm]				Weighting σ_{range}: σ_{ISL} [mm]
		Radial	Along-track	Cross-track	3D	
1	Fixed 50:1	0.001	0.097	0.114	0.162	50:1
	Rigorous VCE	0.001	0.097	0.114	0.162	50.00:1.00
2	Fixed 50:1	10.161	161.719	33.823	166.108	50:1
	Rigorous VCE	10.161	157.186	2.343	157.538	2.19:1.00
3	Fixed 50:1	0.026	0.187	0.171	0.269	50:1
	Rigorous VCE	0.026	0.186	0.170	0.267	50.00:1.05

Table 4-17 shows that orbit errors are smallest when there are no modeling errors, which is expected. In scenario 3, where empirical parameters are estimated, the orbit errors are significantly reduced compared to those in scenario 2. The 3D orbit errors in scenario 3 remain only about 65% larger than those in scenario 1 and below one centimeter. Conversely, the orbit errors in scenario 2 are much larger and exceed one meter.

Upon comparing the results obtained with different data weighting, it was observed that the estimated variance components from VCE deviate from the true measurement accuracy in the presence of modeling errors. The degree of this deviation increases as modeling errors become larger. However, additional empirical parameters can help to reduce orbit errors and bring estimated variance components closer to their true values, as seen in scenario 3.

It is worth noting that although weighting determined with VCE does not demonstrate the true measurement accuracy in the presence of modeling errors, it still helps to reduce satellite orbit errors. For instance, in scenario 2, cross-track direction orbit errors reduced from over 33 cm to less than 3 cm. Compared to solutions where observation weights are fixed at true noise levels, using VCE algorithm reduces 3D orbit errors by approximately 5% and 1% for scenarios 2 and 3 respectively.

4.6.5 Conclusions

This chapter discusses the use of VCE in LEO satellite constellations consisting of dozens to hundreds of satellites. The first section validates the effectiveness of VCE in orbit determination. Without proper weighting assigned to different measurement types, orbit errors could increase by more than 2 times. However, with VCE, accurate weights can be determined for each measurement type resulting in no loss of orbit accuracy compared to using the true weighting.

In the second part of this study, the efficiency of two VCE algorithms are compared. The results demonstrate that both algorithms can estimate orbits with equal accuracy. However, the simplified algorithm is significantly more efficient than its rigorous counterpart. Specifically, when there are 30 satellites in the constellation, the simplified VCE algorithm is already 124 times faster than the rigorous one. This ratio increases to over 2795 as the number of satellites grows to 120. Given that thousands of LEO satellites will soon be launched into space, this study suggests that using this simplified algorithm would be much more efficient without sacrificing orbit accuracy.

Finally, this chapter examines the effect of modeling errors on VCE. The findings indicate that estimated variance components cannot accurately reflect measurement precision in the presence of such errors. As the magnitude of these errors increases, the value deviates further from the true noise level. Additionally, compared to solutions with observation weights fixed at the true noise level, VCE reduces orbit errors.

4.7 Full scale analysis

4.7.1 Introduction

As discussed in chapters 1.2 and 1.3, current research is primarily focused on either GNSS or a few LEO satellites, or an enhanced GNSS with additional LEO satellites. However, the orbit determination of an independent LEO mega-constellation has not received much attention yet.

In chapter 3, a LEO satellite constellation for positioning purposes is designed. Previous sections in chapter 4 explores various factors that impact the accuracy of orbit determination. By utilizing these techniques, it is now possible to perform the orbit determination of an independent LEO satellite constellation in a more complex simulation environment that is closer to reality.

This chapter's simulation will utilize the techniques discussed in chapter 3. Additionally, this simulation will take into account other factors such as tropospheric delay of ground range measurements and noise levels. For a comprehensive overview of the simulation and estimation settings, please refer to Table 4-18.

Table 4-18 Simulation and estimation settings

Orbit and data simulation		
Orbit height	900 km + 700 km	
Walker constellation	73°: 90/9/1 + 38°: 91/7/1	
True force models	Earth gravity field	EIGEN 6S 60×60 (Förste et al., 2011)
	Third body attractions	Sun and Moon (Montenbruck & Gill, 2000, pp. 69-77)
	Solid tides	IERS Conventions 2010 (IERS, 2010)
	Ocean tides	IERS Conventions 2010 (IERS, 2010)
	Relativity	Post-Newtonian correction (Montenbruck & Gill, 2000, pp. 110-112)
	Air drag	DTM-2000 atmosphere model with drag coefficient 2.2 (Bruinsma et al., 2003)
	Solar radiation pressure and albedo	Box-wing model with absorption coefficient 0.79, reflection coefficient 0.21 (Knocke et al., 1988; Montenbruck & Gill, 2000, pp. 77-83)
Data time span	14 d (Oct 1 – Oct 7 and Dec 1 – Dec 7, 2021)	
Sampling interval	1 min	
Elevation cut-off	10°	
Ground range	Noise level	White Gaussian noise of 1 m
	Tropospheric delay	VMF1 (Boehm et al., 2006b)
	Constant satellite bias	Random in the range ±5 mm (Marz et al., 2021; Michalak et al., 2021)
ISL	Noise level	White Gaussian noise of 5 cm
	Constant satellite bias	Random in the range ±5 mm per terminal (5 terminals for each satellite) (Michalak et al., 2021)
Estimation		
Arc length	1 d	
Initial state error	Random ±3 mm for position, ±3 μm/s for velocity	
Data weighting	Fixed weight with $\sigma_{\mathrm{range}} = 1$ m, $\sigma_{\mathrm{ISL}} = 5$ cm	
Force models	Earth gravity field	EIGEN 6S 60×60 (Förste et al., 2011)
	Third body attractions	Sun and Moon (Montenbruck & Gill, 2000, pp. 69-77)
	Solid tides	IERS Conventions 2010 (IERS, 2010)
	Ocean tides	IERS Conventions 2010 (IERS, 2010)
	Relativity	Post-Newtonian correction (Montenbruck & Gill, 2000, pp. 110-112)
	Air drag	Modified Harris-Priester atmosphere model with drag coefficient 1.87 (Montenbruck & Gill, 2000, pp. 89-91)

Table 4-18 (continued)

Estimation		
Force models	Solar radiation pressure and albedo	Box-wing model with absorption coefficient 0.88, reflection coefficient 0.12 (Knocke et al., 1988; Montenbruck & Gill, 2000, pp. 77-83)
Parameters	Initial state vector, empirical accelerations, tropospheric total zenith delay per station, and biases for each LEO satellite and station (as explained in the following paragraphs)	

As shown in Table 4-18, a multi-layer LEO constellation with a total of 181 satellites is selected, which is consistent with the constellation in section 4.5.4. It is the same constellation proposed in chapter 3, but with only a half of the number of satellites to reduce computation time. The force models remain unchanged from chapter 4.3, while the data time span has been extended to 14 days for improving result reliability. Noise levels have also been increased to typical values of pseudorange and microwave links: ground range measurements at 1 m and ISL range measurements at 5 cm. VMF1 is used as the tropospheric model due to its use of real weather data and relative accuracy, whereas ionospheric effects are not mentioned since ionosphere-free linear combination is typically utilized (as discussed in section 2.6.3). Bias simulation remains identical to that in chapter 4, while six global ground stations are selected for this study (as shown in Fig. 4-12). A total of 5 ISL terminals are utilized, with 4 being designated for the ISL with satellites at the same orbit height. These include two intra-orbital links and two inter-orbital links as illustrated in Fig. 4-8 and discussed in section 4.4.2. The remaining terminal is allocated for ILISL purposes, utilizing a link strategy known as the "instant break" with a weight factor of $w = 0.2$, which is explained in section 4.5.4.

The reason for using fixed data weighting instead of VCE in this part is twofold. Firstly, VCE is not yet widely used in orbit determination and the simulations here aim to follow traditional methods. Secondly, as discussed in section 4.6.4, if the modeling is accurate enough, VCE will not significantly affect orbit accuracy. The influence of different weighting methods will be further discussed in section 4.7.2.

In addition to the initial state vector, piece-wise constant empirical accelerations are estimated every 4 h in the along-track direction and every 8 h in the cross-track direction (referred to as "A4 C8" case in section 4.3.2) since it best fits the scenario of this study. Tropospheric total zenith delay is estimated every 2 h per station using GMF as a tropospheric model. Station and satellite biases are estimated following the same method described in section 4.4.2 where station biases and antenna biases connected to the ground are estimated per device, while only one bias value is estimated per pair of two linked satellites for antennas used for ISL purposes.

4.7.2 Results

Table 4-19 displays the results of orbit determination for the proposed independent LEO mega-constellation. The table includes the best possible orbit solution and a case with only ground

range measurements, without ISL, for comparison purposes.

Table 4-19 Mean RMS of orbit errors in radial, along-track, and cross-track directions, and 3D position for the independent system [cm]

Case	Radial	Along-track	Cross-track	3D
No ISL	44.55	128.86	54.10	149.87
With ISL	0.34	1.59	1.63	2.38
Best possible	0.26	0.17	0.06	0.32

Table 4-19 shows that a LEO satellite constellation without ISL may have 3D orbit errors of approximately 1.5 m if the ground stations are scarce. However, by implementing the techniques discussed in this work, these errors can be significantly reduced to just 2.38 cm, which is an optimal outcome given the simulation settings. In fact, with further improvements, it may even be possible to achieve accuracy as high as 0.32 cm using our current orbit modeling approach.

From another perspective, the best possible solution can even reach an accuracy of 0.32 cm, demonstrating the effectiveness of the current orbit modeling. This result suggests that there is room for improvement in cases where ISL is present, particularly in the along-track and cross-track directions where errors are 8 and 26 times larger than the best possible solution respectively; whereas the radial direction has only about a 30% larger error compared to the best possible solution.

To further validate the accuracy of current orbit determination modeling and assess the impact of data weighting, additional simulation comparisons are conducted. The differences between each scenario are listed in Table 4-20, while all other settings remain unchanged from those presented in Table 4-18.

Table 4-20 Empirical parameter and data weighting settings for different scenarios

	Empirical parameter settings	Data weighting
Scenario 1	4 h interval in along-track direction, 8 h interval in cross-track direction	Fixed weight
Scenario 2	30 min interval with 0.1 nm/s^2 constraints in all directions	Fixed weight
Scenario 3	30 min interval with 0.1 nm/s^2 constraints in all directions	Simplified VCE
Scenario 4	10 min interval with 10 nm/s^2 constraints in radial direction, 40 nm/s^2 in along-track direction and 20 nm/s^2 in cross-track direction	Simplified VCE

For comparison, Scenario 1 in Table 4-20 represents the original case with ISL observations. Scenarios 2 and 3 use the same empirical parameter settings but employ different weighting algorithms. The reason for selecting these two types of piece-wise constant

accelerations in scenarios 2/3 and scenario 4, instead of the better choice mentioned in section 4.3.3, is due to a large number of estimated parameters that would significantly increase computation burden and time if a 5 or 6 min interval are chosen. The current configuration with 10 min already imposes a heavy load on computational resources; therefore, choosing a 5 min interval for piece-wise acceleration is neither possible nor necessary. Additionally, since some researchers have used these two selections (see Table 4-1), they will be employed for comparison purposes in this part. The results can be seen in Table 4-21.

Table 4-21 Mean RMS of orbit errors in radial, along-track, and cross-track directions, and 3D position for different scenarios [cm]

Case	Radial	Along-track	Cross-track	3D
Scenario 1	0.34	1.59	1.63	2.38
Scenario 2	10.83	45.55	26.27	54.91
Scenario 3	10.83	45.55	26.27	54.91
Scenario 4	0.48	4.00	4.09	5.97

Table 4-21 reveals that scenario 1 indeed outperforms other scenarios, yielding the best results. Specifically, the 3D orbit errors of scenario 1 are 60% lower than those of scenario 4. This finding suggests that improving orbit accuracy does not necessarily require estimating more empirical parameters, which aligns with the conclusions drawn in section 4.3.

Moreover, comparing scenarios 2 and 3 indicates that different weighting methods do not affect orbit accuracy significantly unless the orbit modeling deviates substantially from true models.

4.7.3 Conclusions

This chapter provides a more realistic simulation setting, which not only confirms the feasibility of an independent LEO system but also demonstrates the effectiveness of the techniques and strategies presented in this work. By utilizing ground range observations from only six global stations and ISL observations, it is possible to determine the orbit of a LEO satellite constellation with an error margin of just a few centimeters.

5 Comparison with GNSS-assisted system

5.1 Introduction

Chapter 4.7 examines the performance of an independent LEO satellite constellation. Currently, onboard GNSS receivers are commonly used for orbit determination of LEO satellites. Meanwhile, as in many of the studies mentioned in chapter 1.2, although the rapid growth of LEO satellites has attracted much attention, including in the field of positioning, most researchers focus on the benefits of these additional LEO satellites to the current GNSS. Systems like LeGNSS (Li et al., 2019a; Ge et al., 2021; Zhang et al., 2023), LEO augmented multi-GNSS (Li et al., 2018; Li et al., 2021b) and Kepler (Michalak et al., 2021) are all involving GNSS in their systems. While the cost of equipping a satellite with a GNSS receiver is not prohibitively high due to the maturity of the market, using GNSS observations may introduce other errors into the system, such as modeling errors within GNSS products. Therefore, one may wonder if there is any benefit to equip a GNSS receiver and have these additional observations. All in all, it is necessary and interesting to compare an independent LEO system with one that uses GNSS observations.

This chapter aims to compare the orbit determination of an independent LEO system with a GNSS-assisted system. Following the simulation settings in chapter 4.7, the GNSS observations used in this comparison are simulated according to Table 5-1. Only GNSS pseudorange measurements are considered in this chapter. Please note that the noise level of these measurements remains consistent with the typical value of 1 m mentioned in chapter 4.7, but differs from the values discussed in chapters 4.3 to 4.6.

Table 5-1 Simulation and estimation settings of GNSS observations

Data simulation		
GNSS range	Satellite	GPS, IGS orbit product
	Noise level	White Gaussian noise of 1 m
	Constant satellite bias	Random in the range ±5 mm
	Clock error	IGS clock product minus of CODE clock product
Estimation		
GPS orbit	CODE orbit product	
Parameters	Besides the parameters listed in Table 4-18, clock and bias for GNSS receiver	

The GNSS pseudorange observations are produced using the GPS orbit from the IGS orbit product. However, in order to replicate real-world GPS orbit errors during the estimation, the GPS orbit will be obtained from the CODE orbit product. The observation noise level is set at

1 m, which matches Table 4-18's value for ground range measurements. Similarly, clock errors in GNSS pseudorange observations are simulated by utilizing the difference between IGS and CODE clock products. It should be noted that although different organizations may have different reference clocks, this difference can be disregarded since receiver clocks are estimated during determination process.

In addition to estimated parameters mentioned in Table 4-18, clocks and biases for GNSS receiver are also included. Clocks are pre-eliminated epoch-wise throughout the process while one constant value per terminal will be estimated for biases.

5.2 Influence of different noise levels

Before comparing the results of the GNSS-assisted system with an independent system, this section will first investigate the impact of different noise levels of the measurements on orbit determination. Specifically, it will examine how varying ratios between measurement types affect orbit accuracy. This analysis is necessary because although this work selects measurements with the pseduorange accuracy for ground range and GNSS observations as well as the microwave accuracy for ISL, there are other measurement types available with differing levels of precision. For example, phase measurements may have a noise level of a few millimeters (Marz et al., 2021; Michalak et al., 2021), while ISL using optical links can also achieve millimeter-level accuracy (Schlicht et al., 2020; Marz et al., 2021). As technology advances, new measurement types or improved measurements with smaller noise levels may emerge. Therefore, studying how results change in different environments is necessary to expand the conclusions drawn from this work to a broader area.

This section tests 8 scenarios that involve the combination of different measurement types, which are listed in Table 5-2. Two global station network sizes are selected: a small one with only 6 stations and a normal one with 32 stations. Both networks are chosen from Fig. 4-12.

Table 5-2 Measurement types included in different scenarios

Notation	Ground range measurements	GNSS range measurements	ISL range measurements
Ground 6 : ISL	Yes, with 6 stations	-	Yes
Ground 32 : ISL	Yes, with 32 stations	-	Yes
GNSS : ISL	-	Yes	Yes
Ground 6 only	Yes, with 6 stations	-	-
Ground 32 only	Yes, with 32 stations	-	-
GNSS only	-	Yes	-
GNSS + ground 6 : ISL	Yes, with 6 stations	Yes	Yes
ISL only	-	-	Yes

Fig. 5-1 shows how the formal error of each scenario changes with the noise ratio, which

represents the noise levels of other measurement types in a given scenario relative to the noise level of the ISL measurement. In this section, the noise level of the ISL is assumed to be 0.1 cm. This value is deliberately chosen because, on the one hand, ISL measurements are typically more accurate than other types of measurements mentioned above. A smaller value for ISL allows for a larger range of noise levels in other measurement types to consider, resulting in a noise ratio greater than 1 that is easier to illustrate. On the other hand, the actual accuracy of the ISL observation is not important here since only the ratio among these types matters. Additionally, the exact values of the formal error are also not relevant as this work is solely interested in comparing different combinations and their relationship with the noise ratio. It is possible to adjust the value of ISL and still obtain a ratio covered by Fig. 5-1.

To better compare and illustrate cases with only one type of measurement, the noise level is divided by 0.1 cm to obtain a noise ratio. For instance, in the case where both ground range and ISL measurements are taken, the noise level for range measurement can be set between 0.1 cm and 5 m resulting in a noise ratio ranging from 1:1 to 5000:1. This range should cover most situations. Similarly, for cases with only ground range measurements assumed to have a noise level within the same limits (0.1 cm – 5 m), their ratios to 0.1 cm also fall within this same range (from 1:1 to 5000:1).

It is worth noting that GNSS observations and ground observations utilized in this study are assumed to have comparable noise levels. To avoid complicating the scenarios under consideration, it is assumed that they share the same level of noise for the "GNSS + ground 6 : ISL" case.

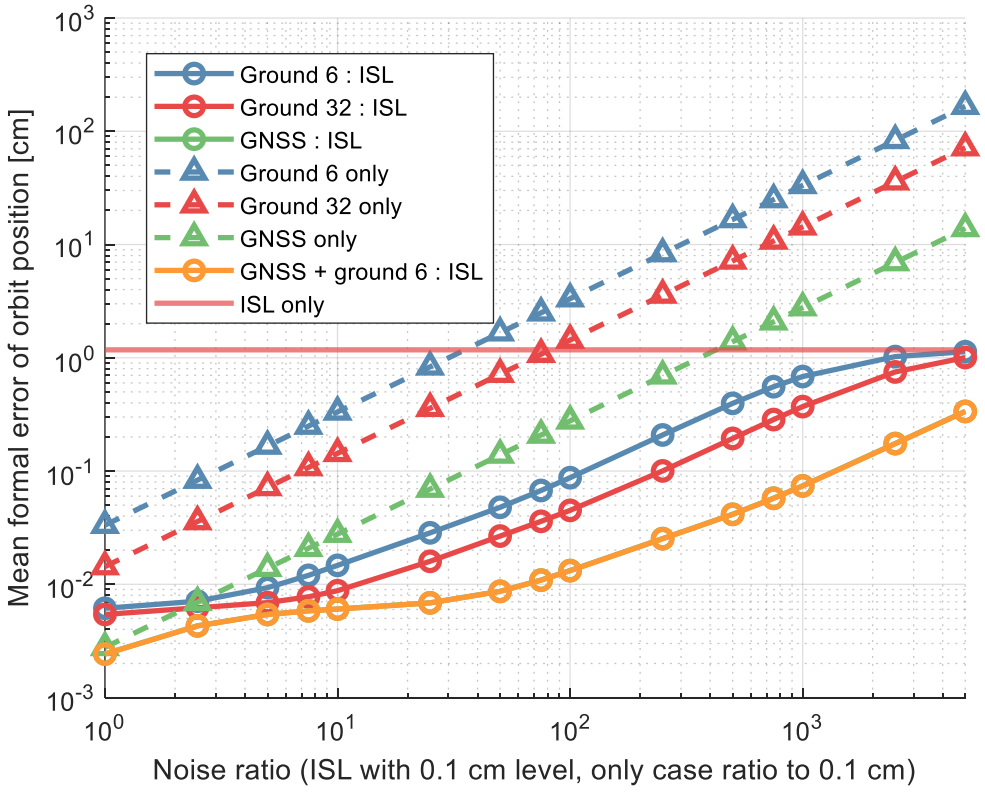

Fig. 5-1 Mean formal error of orbit position for different measurement scenarios. Case "GNSS : ISL" is not visible because it overlaps with the case "GNSS + ground 6 : ISL"

The figure demonstrates that as the noise ratio increases, all types of formal errors also increase. The formal errors in cases with only one type of measurements grow exponentially with the noise level. In particular, the "ISL only" case is represented by a line parallel to the abscissa because its noise level remains constant at 0.1 cm. This line serves to illustrate the upper limit of cases involving ISL measurement and will be further elaborated on later.

In cases where ISL observations are not available, the "GNSS only" case outperforms cases using ground stations alone. With over 30 GPS satellites currently in orbit, located in MEO and able to observe LEO satellites more frequently than ground stations, they can provide a greater number of observations with better geometry. Table 5-3 shows the number of observations for each type in this simulation. Therefore, if the accuracy of ground/GNSS range measurement is sufficient (noise ratio < 2.5:1), the "GNSS only" case performs even better than the case using both ground and ISL measurements. However, when the noise ratio of ground/GNSS range measurement to ISL exceeds 2.5:1, ISL observations become beneficial and improve performance compared to using just GNSS measurements.

If the noise ratio continues to grow, i.e. the ground/GNSS observations get worse, the accuracy of determined orbits will decrease. However, this degradation will not be linear and will stop near the upper limit of the "ISL only" case mentioned earlier. This is because if ground/GNSS observations are too poor, their contribution to the estimation process will be significantly reduced. In such cases, ISL measurements dominate and determine orbit accuracy. Therefore, the "ISL only" case sets an upper boundary for cases with ISL measurements.

However, the "ISL only" case is not able to accurately determine orbits due to its insensitivity towards constellation rotation. As a result, the upper boundary from this case is significantly higher than other "only" cases, as depicted in the figure. Additionally, if ground/GNSS observations are highly precise (e.g., noise ratio of 1:1), any advantage gained from additional ISL observations cannot be discerned since they are treated equally during estimation. In this case, the primary benefit of adding ISL observations is an increase in the number of observations used in the process. Consequently, as shown in Fig. 5-1, the one with the higher number of observations gets a smaller formal error.

Table 5-3 Average number of observations per day for each measurement type

Measurement type	Average number of observations per day
Ground 6	6693
Ground 32	35110
GNSS	740651
ISL	82089

Finally, it is worth noting that in Fig. 5-1, the green solid line representing the "GNSS : ISL" case is not visible. This is due to the fact that both ground measurements and GNSS observations share the same noise level. Additionally, since there are significantly more GNSS observations than observations in the "Ground 6" case, the contribution from the six ground stations is negligible when combined with GNSS data for "GNSS + ground 6 : ISL".

Consequently, results for "GNSS : ISL" case coincide with those of the "GNSS + ground 6 : ISL" case which performs best among all cases as expected.

5.3 Results

According to the analysis in chapter 5.2, two cases assisted with GPS observations are investigated for the comparison: "GNSS only" case and "GNSS + ISL" case. The former determines LEO satellite orbits solely with GNSS observations, while the latter performs estimation with both GNSS and ISL observations. The simulation and estimation settings follow the configuration introduced in Table 4-18 and Table 5-1, respectively. Table 5-4 presents the results, which are also compared to those of an independent LEO satellite constellation as well as the best possible solution in Fig. 5-2.

Table 5-4 Mean RMS of orbit errors in radial, along-track, and cross-track directions, and 3D position for the GNSS-assisted system [cm]

Case	Radial	Along-track	Cross-track	3D
GNSS only	1.79	4.51	3.22	5.87
GNSS + ISL	0.35	0.61	0.57	0.93

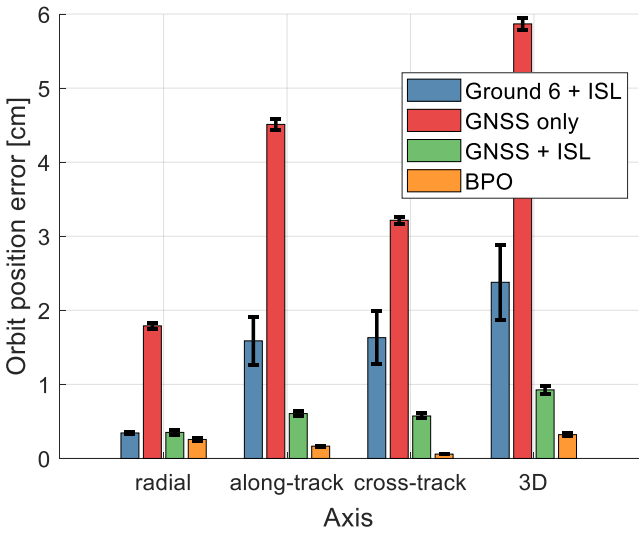

Fig. 5-2 Comparison of mean RMS of orbit errors in each direction and 3D position for different cases. The error bar on each histogram indicates the STD of orbit errors over 14 days

Table 5-4 shows that the orbits of LEO satellites can be accurately determined through GNSS observations due to their large number. The "GNSS only" case resulted in a 3D orbit error of approximately 6 cm, which is significantly smaller than the "Ground 6 only" case with an error of 150 cm. However, when compared to the independent system introduced in this work, there are still significant errors present - radial errors are larger by 81%, along-track by

65%, cross track by 49% and overall by 59%. This is illustrated in Fig. 5-2.

Meanwhile, if the LEO mega-system combines both GNSS receiver and ISL technique, it can further improve orbits to sub-centimeter level by utilizing a massive number of GNSS observations and high accuracy of ISL observations. This combination reduces 3D orbit errors by 84% compared to the "GNSS only" case. It is even 61% better than the independent system discussed in chapter 4.7. Fig. 5-2 shows that this improvement mainly occurs in the along-track and cross-track directions with a reduction of orbit errors by 62% and 65%, respectively.

5.4 Conclusions

The onboard GNSS receiver is often used to determine the orbits of LEO satellites. This chapter compares the orbit determination results of the independent LEO satellite system with this traditional method.

This chapter firstly discusses the impact of varying noise level ratios on orbit accuracy. When no ISL observations are present, the "GNSS only" case outperforms the "Ground only" cases due to a larger number of GNSS observations. However, in most situations, when ground/GNSS range measurements are less accurate (with a ratio to ISL measurement greater than 2.5:1), the "Ground + ISL" case performs better than the "GNSS only" case. Unlike scenarios without ISL observations, formal error in cases with ISL observations does not continuously increase as observation accuracy degrades; instead, the formal error of the "ISL only" case sets an upper limit for all scenarios. Among all these different combinations of measurement types, the best performance is achieved by the "GNSS + ISL" and "GNSS + ground 6 + ISL" cases.

The results of orbit determination using the GNSS-assisted system demonstrate the feasibility and advantages of an independent LEO satellite system. Compared to relying solely on observations from onboard GNSS receivers, the independent system improves the orbit determination by 59%. Additionally, the analysis suggests that even better orbit accuracy is achievable through a combination of extensive GNSS observations and precise ISL measurements. This approach could further reduce orbit errors to sub-centimeter levels.

6 Summary and outlook

6.1 Summary and conclusions

6.1.1 Summary and answers to motivation questions

The space exploration of human started with LEO satellites. With the development of technology, the low Earth orbit has not only not been replaced, but also has played an increasingly important role. Especially in the past decade, commercial companies such as SpaceX have begun launching thousands of LEO satellites to provide communication and internet services. These hundreds and thousands of LEO satellites also have enormous potential in other areas, including for positioning. Researchers have studied the possibility to enhance the current GNSS with additional LEO satellites. However, few attention has been paid to the LEO mega-constellation as an independent system. Meanwhile, orbit determination is the key foundation for many further applications. This work starts from the basic constellation design and gradually analyzes various aspects that affect the orbit determination results, discusses the orbit determination accuracy of an independent LEO satellite constellation in a real environment, and compares it with traditional GNSS-assisted orbit determination.

Before starting the analysis, this work elaborates on the key theoretical knowledge applied in the simulation and analysis of this work. Following the fundamentals of orbit determination, this work delves into various aspects of the design and orbit determination of the independent LEO satellite constellation, particularly focusing on some key issues and discussions raised in chapter 1.3.

A systematic approach is necessary to arrange the orbits of hundreds and thousands of LEO satellites in order to meet application requirements. This task falls under constellation design, which offers various approaches for designing satellite constellations tailored to different applications. This work focuses on the following specific tasks to design the constellation.

1. Selection criteria and requirements for the constellation.

In order to design an independent satellite constellation that can function as a positioning system, it is necessary for at least four satellites (or three if a two-way link is used) to be visible from any location on Earth at any given time, as per the GNSS principle. Ideally, the visibility of these satellites should be as evenly as possible in order to achieve better homogenous geometry worldwide. Therefore, the number of visible satellites and percentage of satellite visibility along latitude are used as selection criteria. The DOP is a geometric factor that indicates how measurement errors impact estimation accuracy and is therefore also used to assess the constellation's geometry.

2. Selection of constellation type.

The Walker constellation is one of the most widely used design methods. Among them, the Walker Delta method is commonly used in GNSS design, while the Walker Star method is adopted by some communication satellite constellations like Iridium. This work elaborates on their respective advantages and disadvantages, and selects the Walker Delta as the benchmark for constellation design in this work. To achieve a more uniform distribution of the visibility around the world, this work proposes a multi-layer constellation design that combines satellites with different inclinations and orbit heights. Satellites at a higher inclination have better visibility in higher latitudes and can cover polar areas, while those at a lower inclination increase visibility near the equator. Further simulations demonstrate this idea.

3. Selection of constellation parameters and evaluation of the performance.

First, the parameters for the inclinations and orbit heights of the combined constellation are selected. The STD of the percentage of the satellite visibility along latitude is used to find a solution with more globally uniform distribution. A two or three-layered constellation is analyzed and discussed, with results showing that this work's constellation consists of two layers. Using an enumeration method, their orbital heights, inclinations, and the number of satellites ratio between the two layers are determined. The best homogenous visibility is achieved through a combination of 700 km + 38° and 900 km + 73° with an equal number of satellites in each layer.

Next, an enumeration search algorithm is proposed to determine proper values for the total number of satellites t and the number of orbital planes p, defined by the Walker constellations. After comparison, it was found that a combination consisting of 189 satellites in each sub-constellation with 9 high orbital planes and 7 low orbital planes ensures more than six visible satellites around the world. The relative phasing coefficients f of both sub-constellations are then determined to achieve better DOP values while considering uniform distribution; $f = 1$ was selected for further study.

4. Evaluation of the selected constellation.

The number of visible satellites and the PDOP distribution of the finally selected multi-layer constellation, orbital height of 900 km with Walker Delta 73°: 189/9/1 and orbital height of 700 km with Walker Delta 38°: 189/7/1, are illustrated. At least 6 satellites are visible worldwide. In most regions, more than 9 satellites can be reached. In the mid-latitude area, where the majority of the population lives, over 12 visible satellites are available. PDOP values below 3 are observed in non-polar areas when using traditional one-way observations. However, if two-way links can be established, the PDOP can drop to less than 2, even in polar regions.

This work then addresses the questions and concerns raised regarding orbit determination for the independent LEO constellation, based on its design. There are various factors that can impact the accuracy of an orbit, including physical structures like ground station distribution and ISL topology, as well as estimation processes such as data weighting and empirical accelerations.

1. Software development.

The author has developed a specialized software to simulate and estimate LEO mega-constellations. The software utilizes an open-source mathematical and space dynamics library, with the author implementing core features. It can run in both GUI and terminal modes, and its settings are easily configurable, making it capable of fulfilling all requirements for this work.

2. Influence of the empirical accelerations.

The estimation of empirical parameters is a widely used technique to enhance orbit modeling and improve orbit accuracy. This study examines how various settings and constraints for empirical parameters affect the determination of orbits for a LEO satellite constellation. The study's findings indicate that neither excessively long nor short intervals are optimal for orbit determination when using empirical accelerations with longer than 1 h interval. The effectiveness of different estimation intervals varies depending on the direction being analyzed. When intervals are less than 30 minutes, shorter intervals generally result in smaller orbit errors. Additionally, tightening constraints in a given direction also reduces orbit errors in that direction. However, overly tight constraints can lead to much larger orbit errors. For the purpose of this research, it is recommended to estimate empirical parameters with a 4 h interval in the along-track direction and an 8 h interval in the cross-track direction.

3. Influence of the ground station network. Specifically, the impact of the number and distribution of the stations on orbit accuracy.

This study delves into how different ground station distributions and numbers affect orbit determination, while also exploring the benefits of additional ISL observations. The study first selects three regional networks, four quasi-global networks, and a global network to analyze their results. Findings indicate that a more global network leads to smaller orbit errors; the geometry of the ground station distribution is more crucial than observation quantity for precise orbit determination. A high latitude network with poor geometry produces larger errors compared to low or middle latitude networks. By adding ISL observations, regional networks can achieve smaller orbit errors than global networks without ISL. Furthermore, this research demonstrates that it is unnecessary to precisely calibrate satellite biases on-ground when estimating precise orbits. To investigate the relationship between the number of stations and orbit errors, five global networks are selected with varying station counts ranging from 1 to a maximum of 60. The findings indicate that beyond 16 global stations, there is minimal improvement in orbit accuracy. Conversely, ISL observations can significantly reduce orbit errors for networks with fewer stations. Specifically, a network comprising six stations equipped with ISL observations can achieve comparable accuracy levels to those attained by a larger network consisting of 60 stations. Four European networks are chosen for cross-validation to represent various numbers of stations in a regional network. The findings highlight the significance of network geometry. Specifically, it was discovered that the orbit determined by 60 stations in Europe is inferior to that obtained from a global network comprising only 6 stations. However, if additional ISL observations are accessible, orbit errors can be reduced to levels comparable with those achieved by global networks.

4. Influence of the ISL topology, especially the ILISL links.

Building upon previous research that demonstrated the benefits of ISL, this work explores

the impact of various types of ISL on orbit determination for the LEO satellite constellation. Specifically, ILISL plays a critical role in connecting the multi-layer constellation as a cohesive unit. The work introduces three typical ILISL link topologies and proposes two additional variants. The investigation begins by comparing the intra-orbital and inter-orbital links. The geometry analysis reveals that the intra-orbital link remains stationary and can be established permanently, while for the inter-orbital link, although a permanent link can also be formed, satellites in the neighboring planes move in an "8" pattern. Orbit determination results indicate that the estimated orbit for the intra-orbital link is significantly worse than that of the inter-orbital link due to its lower sensitivity to the cross-track motion. If the number of links is limited, the inter-orbital link is more favorable for orbit determination compared to the intra-orbital link which has near meter level accuracy. Under similar circumstances, using the inter-orbital link can reduce orbit errors to millimeter-level precision. Unlike intra- and inter-orbital links, ILISL cannot maintain a permanent connection due to the varying motion of satellites at different orbital heights. The use of ILISL can improve orbit determination by at least 46%. Among all methods, those with an "instant break" strategy result in smaller orbit errors. However, increasing the weight factor gradually worsens orbits determined by this strategy while the "connect till break" strategy produces orbits with roughly the same large errors regardless of changes in the weight factor. The minimal orbit errors occur when using an "instant break" strategy with a weight factor of 0.2.

5. Importance of data weighting, including the algorithm for handling huge numbers of observations. The influence of modeling errors is also investigated.

With additional ISL observations, there is more than one type of measurement in the orbit determination. Accurate data weighting is crucial for achieving precise results, and one method for determining the weight of the combined data is through VCE. However, given the computational burden posed by thousands of LEO satellites in a mega-constellation, this work proposes a simplified version of VCE that is derived from the rigorous approach. Firstly, the VCE algorithms and the significance of data weighting are discussed. Incorrect weighting can result in orbit errors that are more than twice as large. However, VCE can accurately determine the appropriate weights for each measurement type without prior knowledge of their characteristics. The orbits calculated using VCE are equally precise to those obtained with the true weighting. The simplified VCE algorithm is significantly faster than the rigorous algorithm, with a speed advantage of 124 times when only 30 satellites are compared. This ratio increases exponentially as the number of satellites grows. Despite this significant difference in speed, there is no impact on the accuracy of orbit determination results which remain highly precise. Given that thousands of LEO satellites will soon be launched into space, the simplified algorithm offers much greater efficiency compared to its rigorous counterpart. Additionally, this study examines the effect of modeling errors on VCE. The findings indicate that estimated variance components cannot accurately reflect measurement precision when there are modeling errors present. As the magnitude of these errors increases, the value deviates further from the true noise level. However, in cases where significant modeling errors exist, VCE can still aid in reducing orbit errors.

6. Orbit determination of the selected independent constellation in a realistic simulation.

This study creates a simulation that closely resembles real-world conditions. The purpose is to evaluate the performance of an independent LEO mega-system with the techniques studied in this work. By utilizing ground range observations from only six global stations and ISL observations, including ILISL, the orbit determination of a LEO satellite constellation can achieve an error margin of just a few centimeters. These results demonstrate the feasibility of this system.

7. Comparison with GNSS-assisted system, as well as the influence of different noise levels.

Since GNSS observations are commonly utilized for orbit determination of LEO satellites, this study also evaluates the outcomes in comparison to this conventional approach. The impact of different noise level ratios on orbit accuracy is firstly discussed. With much more observations available, using only GNSS measurements yields better results than relying solely on ground-based measurements. In most cases where the ratio of ground/GNSS measurement noise to ISL measurement noise exceeds 2.5:1, using both ground and ISL measurements can result in smaller formal errors than using only GNSS data, even with fewer total observations. Additionally, the formal error associated with using only ISL measurements sets an upper limit for all scenarios involving ISL; this means that orbit errors will not continue to increase as the accuracy of ground/GNSS observations degrades. The results of orbit determination using the GNSS-assisted system demonstrate the superiority of the proposed independent LEO satellite system. The independent system is capable of determining orbits with 59% better accuracy than relying solely on GNSS observations. Nevertheless, incorporating a GNSS receiver can further enhance this independent system's performance. By utilizing additional extensive GNSS observations, it is possible to further reduce orbit errors to sub-centimeter levels.

6.1.2 Overall conclusions

After summarizing and answering all the questions raised in chapter 1.3, some overarching conclusions can now be drawn.

With a large number of LEO satellites already in space and significant potential across various scientific fields, an independent LEO satellite constellation is poised to garner increased attention in the future. In order to achieve effective communication and positioning, it is important to ensure that the visibility of satellites from the ground is as consistent as possible around the world. Additionally, a minimum of 4 satellites should be visible simultaneously. This study proposes a multi-layer Walker Delta constellation, which offers improved coverage in polar areas from satellites with higher inclination angles and enhanced visibility near the equator from satellites with lower inclination angles. By analyzing satellite visibility and using the enumeration method, it is determined that an orbital height of 900 km with Walker Delta 73°: 189/9/1 and an orbital height of 700 km with Walker Delta 38°: 189/7/1 are the optimal choice for this work. This configuration ensures that at least six satellites can be observed simultaneously from any location worldwide. Additionally, in non-polar regions, the PDOP values remain below 3. If two-way links are possible, PDOP can decrease to less than 2 even in polar regions.

Precise orbit determination is crucial for numerous applications. This study thoroughly examines different aspects related to determining the orbits of an independent constellation of LEO satellites. Using self-developed software, this study simulates a realistic scenario to evaluate the performance of this independent system. The results demonstrate that by utilizing observations from just six global ground stations and ISL, the orbit accuracy of this system can achieve centimeter-level precision. Moreover, this work provides a detailed discussion on various factors that can impact orbit accuracy. Proper estimation of empirical accelerations has the potential to improve orbit accuracy. The study concludes that different coordinate components exhibit varying levels of sensitivity with respect to the estimation interval of empirical parameters. In general, reducing orbit errors is more achievable by employing shorter intervals and stricter constraints within certain limits. The distribution and quantity of ground stations can impact the accuracy of estimated orbits. This study concludes that the arrangement of ground stations is more important than the station number or amount of observations for precise orbit determination. Furthermore, this research shows that it is not necessary to calibrate satellite biases with high precision on the ground when estimating accurate orbits. If additional ISL observations are available, even a regional network or a small number of stations can achieve orbit errors similar to those obtained with a global network. Building upon the previous study, this research further explores how different types of ISL affect the accuracy of orbits. The results from orbit determination show that the estimated orbit for the intra-orbital links is notably worse compared to the inter-orbital links due to their limited sensitivity to the cross-track motion. Meanwhile, employing ILISL can significantly enhance orbit accuracy. Specifically, when it comes to determining orbits, the "instant break" strategy proves more advantageous than the "connect till break" approach. The minimal orbit errors occur when using an "instant break" strategy with a weight factor of 0.2. When there are multiple types of observations available, it is crucial to use an appropriate weighting algorithm. This study introduces a simplified VCE algorithm that efficiently calculates the weights for different observation types. Even with only 30 satellites, this simplified algorithm is already 124 times faster than the traditional rigorous method, while still providing accurate estimation of weights and orbits. As the number of satellites increases, this speed advantage grows exponentially. Additionally, this research demonstrates that VCE can help reduce orbit errors even in situations where significant modeling errors are present.

Lastly, this study compares the performance of this independent system with a traditional GNSS-assisted system. By analyzing the formal error of orbit position under different levels of measurement noise, it is found that in most cases where the ratio of ground/GNSS measurement noise to ISL measurement noise exceeds 2.5:1, utilizing both ground and ISL measurements leads to smaller formal errors compared to using only GNSS data. The results of orbit determination demonstrate that the proposed independent system outperforms the traditional GNSS-assisted system, with orbit errors being 59% smaller. Furthermore, if GNSS receivers are incorporated into this independent system, the accuracy of orbit determination can be further enhanced to sub-centimeter level.

6.2 Outlook

Although this work thoroughly studied the orbit determination of an independent LEO satellite mega-constellation, covering everything from fundamental constellation design to key techniques for orbit determination and a full comparison with traditional GNSS-assisted systems, there are still some aspects that require further investigation.

This work primarily focuses on determining the orbit of a LEO constellation consisting of 181 satellites due to limitations in computing resources and time. It would be intriguing to compare these results with those obtained from the full constellation, which comprises 378 satellites. If feasible, it would be worthwhile to conduct further research on the outcomes obtained from an even greater number of satellites and explore any potential correlations between satellite quantity and results.

This work simplifies the discussion of ILISL topology, which is a complex topic that requires consideration of various aspects. However, since it is not the primary focus of this work, only three classical strategies and their variants are studied. Further research can explore additional strategies and factors that affect satellite link topology such as onboard resource limitations, selection of initiating satellites in constellations, and time/effort costs during link switches. These topics can be explored in specialized works dedicated to them.

The software "LeoCon" is still in development and additional features are yet to be implemented. There are opportunities for improvement to provide a more comprehensive solution, such as exploring the performance of orbit determination with the phase measurement in addition to the range measurement. Additionally, it is important to consider how clock errors on LEO satellites can impact orbit accuracy in environments where two-way links cannot be established.

Furthermore, this work has demonstrated the feasibility of achieving accurate orbit determination results for an independent LEO satellite constellation. It would be intriguing to assess the positioning accuracy of this system and compare it with GNSS.

Bibliography

Allende-Alba G, Montenbruck O (2016) Robust and precise baseline determination of distributed spacecraft in LEO. Advances in Space Research, 57(1): 46-63. https://doi.org/10.1016/j.asr.2015.09.034

Amazon (2019) Application of Kuiper Systems LLC for Authority to Launch and Operate a Non-Geostationary Satellite Orbit System in Ka-band Frequencies. Federal Communications Commission (FCC). Document ID: SAT-LOA-20190704-00057

Ananda MP, Berstein H, Bruce RW (1984) Autonomous Navigation of the Global Positioning System Satellite. AIAA Guidance and Control Conference, Seattle, WA, pp. 321-327

Ananda MP, Bernstein H, Cunningham KE, Feess WA, Stroud EG (1990) Global Positioning System (GPS) autonomous navigation. IEEE Symposium on Position Location and Navigation. A Decade of Excellence in the Navigation Sciences, pp. 497-508. https://doi.org/10.1109/plans.1990.66220

Arianespace (2022) Arianespace to launch eight new Galileo satellites. Arianespace. https://www.arianespace.com/press-release/arianespace-to-launch-eight-new-galileo-satellites/. Accessed 19 September 2022

Asvial M, Tafazolli R, Evans B (2002) Non-GEO Satellite Constellation Design with Satellite Diversity Using Genetic Algorithm. 20th AIAA International Communication Satellite Systems Conference and Exhibit. https://doi.org/10.2514/6.2002-2018

Avendaño ME, Davis JJ, Mortari D (2013) The 2-D lattice theory of Flower Constellations. Celestial Mechanics and Dynamical Astronomy, 116(4): 325-337. https://doi.org/10.1007/s10569-013-9493-8

Bashforth F, Adams JC (1883) An Attempt to Test the Theories of Capillary Action by Comparing the Theoretical and Measured Forms of Drops of Fluid, with an Explanation of the Method of Integration Employed in Constructing the Tables which Give the Theoretical Forms of Such Drops. Cambridge University Press, Cambridge. ISBN: 978-1163935088

Bekhti M, Bendimerad FT, Deschamps A, Lion G, Métris G, Meziane-Tani I (2016) Optimization of small satellite constellation design for continuous mutual regional coverage with multi-objective genetic algorithm. International Journal of Computational Intelligence Systems, 9(4). https://doi.org/10.1080/18756891.2016.1204112

Berry MM, Healy LM (2020) Implementation of Gauss-Jackson Integration for Orbit Propagation. The Journal of the Astronautical Sciences, 52(3): 331-357. https://doi.org/10.1007/bf03546367

Beutler G (2005a) Methods of Celestial Mechanics, Vol. 2. Springer. ISBN: 978-3-540-40750-8

Beutler G (2005b) Methods of Celestial Mechanics, Vol. 1. Springer. ISBN: 3-540-40749-9

Beutler G, Jäggi A, Hugentobler U, Mervart L (2006) Efficient satellite orbit modelling using pseudo-stochastic parameters. Journal of Geodesy, 80(7): 353-372. https://doi.org/10.1007/s00190-006-0072-6

Bock H, Jäggi A, Meyer U, Visser P, van den Ijssel J, van Helleputte T, Heinze M, Hugentobler U (2011) GPS-derived orbits for the GOCE satellite. Journal of Geodesy, 85(11): 807-818. https://doi.org/10.1007/s00190-011-0484-9

Boehm J, Niell A, Tregoning P, Schuh H (2006a) Global Mapping Function (GMF): A new empirical

mapping function based on numerical weather model data. Geophysical Research Letters, 33(7). https://doi.org/10.1029/2005gl025546

Boehm J, Werl B, Schuh H (2006b) Troposphere mapping functions for GPS and very long baseline interferometry from European Centre for Medium-Range Weather Forecasts operational analysis data. Journal of Geophysical Research: Solid Earth, 111(B2). https://doi.org/10.1029/2005jb003629

Bruinsma S, Thuillier G, Barlier F (2003) The DTM-2000 empirical thermosphere model with new data assimilation and constraints at lower boundary: accuracy and properties. Journal of Atmospheric and Solar-Terrestrial Physics, 65(9): 1053-1070. https://doi.org/10.1016/s1364-6826(03)00137-8

Butcher JC (2016) Numerical Methods for Ordinary Differential Equations. John Wiley & Sons, Ltd. ISBN: 9781119121503

Capez GM, Henn S, Fraire JA, Garello R (2022) Sparse Satellite Constellation Design for Global and Regional Direct-to-Satellite IoT Services. IEEE Transactions on Aerospace and Electronic Systems, 58(5): 3786-3801. https://doi.org/10.1109/taes.2022.3185970

Chan SP (2002) The birth and demise of an idea: Teledesic's 'Internet in the sky'. The Seattle Times. https://archive.seattletimes.com/archive/?date=20021007&slug=teledesic070. Accessed 19 September 2022

Chang G, Xu T, Yao Y, Wang Q (2018) Adaptive Kalman filter based on variance component estimation for the prediction of ionospheric delay in aiding the cycle slip repair of GNSS triple-frequency signals. Journal of Geodesy, 92(11): 1241-1253. https://doi.org/10.1007/s00190-018-1116-4

Chory M, Hoffman D, Major C, Spector V (1984) Autonomous navigation - Where we are in 1984. 17th Fluid Dynamics, Plasma Dynamics, and Lasers Conference. https://doi.org/10.2514/6.1984-1826

Clark S (2019) Successful launch continues deployment of SpaceX's Starlink network. Spaceflight Now. https://spaceflightnow.com/2019/11/11/successful-launch-continues-deployment-of-spacexs-starlink-network/. Accessed 19 September 2022

Clark S (2022) OneWeb set to resume launches on Indian rocket. Spaceflight Now. https://spaceflightnow.com/2022/10/21/oneweb-set-to-resume-launches-on-indian-rocket/. Accessed 28 October 2022

CMS (2022) The orbital elements of China Space Station. China Manned Space (CMS). http://en.cmse.gov.cn/news/202107/t20210722_48418.html. Accessed 19 September 2022

Colombo OL (1989) The dynamics of global positioning system orbits and the determination of precise ephemerides. Journal of Geophysical Research, 94(B7). https://doi.org/10.1029/JB094iB07p09167

Cowell PH, Crommelin ACD (1909) Appendix to Greenwich Observations.

Davis JJ, Avendaño ME, Mortari D (2013) The 3-D lattice theory of Flower Constellations. Celestial Mechanics and Dynamical Astronomy, 116(4): 339-356. https://doi.org/10.1007/s10569-013-9494-7

Deng Z, Ge W, Yin L, Dai S (2023) Optimization design of two-layer Walker constellation for LEO navigation augmentation using a dynamic multi-objective differential evolutionary algorithm based on elite guidance. GPS Solutions, 27. https://doi.org/10.1007/s10291-022-01366-5

Draim JE (1985) Three- and four-satellite continuous-coverage constellations. Journal of Guidance, Control, and Dynamics, 8(6): 725-730. https://doi.org/10.2514/3.20047

Draim JE (1991) Continuous global N-tuple coverage with (2N + 2) satellites. Journal of Guidance, Control, and Dynamics, 14(1): 17-23. https://doi.org/10.2514/3.20599

Duan B, Hugentobler U (2019) Precise orbit determination of Sentinel satellites using zero-difference ambiguity resolution approach. Living planet symposium, Milan, Italy

Duan B, Hugentobler U, Selmke I, Marz S, Killian M, Rott M (2022) BeiDou Satellite Radiation Force Models for Precise Orbit Determination and Geodetic Applications. IEEE Transactions on Aerospace and Electronic Systems, 58*(*4): 2823-2836. https://doi.org/10.1109/taes.2021.3140018

Ely TA, Crossley WA, Williams EA (1999) Satellite Constellation Design for Zonal Coverage Using Genetic Algorithms. The Journal of the Astronautical Sciences, 47*(*3-4): 207-228. https://doi.org/10.1007/bf03546200

eoPortal (2017) JPSS-1/NOAA-20. European Space Agency (ESA). https://www.eoportal.org/satellite-missions/noaa-20. Accessed 19 September 2022

eoPortal (2021) Iridium NEXT. European Space Agency (ESA). https://www.eoportal.org/satellite-missions/iridium-next. Accessed 19 September 2022

eoPortal (2022) OneWeb. European Space Agency (ESA). https://www.eoportal.org/satellite-missions/oneweb. Accessed 19 September 2022

ESA (2022a) GOCE Overview. European Space Agency (ESA). https://earth.esa.int/eogateway/missions/goce/description. Accessed 19 September 2022

ESA (2022b) ISS: International Space Station. European Space Agency (ESA). https://www.esa.int/Science_Exploration/Human_and_Robotic_Exploration/International_Space_Station/ISS_International_Space_Station. Accessed 19 September 2022

ESA (2022c) MetOp Overview. European Space Agency (ESA). https://earth.esa.int/eogateway/missions/metop/description. Accessed 19 September 2022

ESA (2022d) Swarm Overview. European Space Agency (ESA). https://earth.esa.int/eogateway/missions/swarm/description. Accessed 19 September 2022

European-Commission (2021) Commission awards €1.47 bn in contracts to launch the 2nd Generation of Galileo Satellites. European Commission Defence Industry and Space. https://defence-industry-space.ec.europa.eu/commission-awards-eu147-bn-contracts-launch-2nd-generation-galileo-satellites-2021-01-20_en. Accessed Aug 9 2022

FAA (2022) What are LEO, GEO, GSO, and GTO? https://www.faa.gov/space/additional_information/faq#s1. Accessed 13 September 2022

FCC (2021) FCC Authorizes Boeing Broadband Satellite Constellation. Federal Communications Commission (FCC). Document ID: FCC 21-115

Feder BJ (2003) Globalstar, Bankrupt Satellite Company, to Be Sold for $55 Million. The New York Times. https://www.nytimes.com/2003/01/16/business/globalstar-bankrupt-satellite-company-to-be-sold-for-55-million.html. Accessed 19 September 2022

Feng L, Ruan R, Zeng A (2020) A Method of Combined Orbit Determination of Multi-source Data with Modified Helmert Variance Component Estimation. In: China Satellite Navigation Conference (CSNC) 2020 Proceedings: Volume II, pp. 47-57. https://doi.org/10.1007/978-981-15-3711-0_5

Fernández FA (2011) Inter-satellite ranging and inter-satellite communication links for enhancing GNSS satellite broadcast navigation data. Advances in Space Research, 47*(*5): 786-801. https://doi.org/10.1016/j.asr.2010.10.002

Ferreira A, Galtier J, Penna P (2002) Topological Design, Routing, and Handover in Satellite Networks. In: Handbook of Wireless Networks and Mobile Computing, pp. 473-493. https://doi.org/10.1002/0471224561.ch22

Förste C, Bruinsma S, Shako R, Marty J-C, Flechtner F, Abrykosov O, Dahle C, Lemoine J-M, Neumayer K-H, Biancale R, Team E (2011) EIGEN-6 – A new combined global gravity field model including GOCE data from the collaboration of GFZ Potsdam and GRGS Toulouse. EGU General Assembly

2011, Vienna, Austria

Ge H, Li B, Ge M, Nie L, Schuh H (2020a) Improving Low Earth Orbit (LEO) Prediction with Accelerometer Data. Remote Sensing, 12*(*10). https://doi.org/10.3390/rs12101599

Ge H, Li B, Nie L, Ge M, Schuh H (2020b) LEO constellation optimization for LEO enhanced global navigation satellite system (LeGNSS). Advances in Space Research, 66*(*3): 520-532. https://doi.org/10.1016/j.asr.2020.04.031

Ge H, Li B, Jia S, Nie L, Wu T, Yang Z, Shang J, Zheng Y, Ge M (2021) LEO Enhanced Global Navigation Satellite System (LeGNSS): progress, opportunities, and challenges. Geo-spatial Information Science: 1-13. https://doi.org/10.1080/10095020.2021.1978277

Globalstar (2022) Globalstar Announces Successful Launch of Spare Satellite. Globalstar. https://investors.globalstar.com/news-releases/news-release-details/globalstar-announces-successful-launch-spare-satellite. Accessed 19 September 2022

Graham W (2018) SpaceX launches Falcon 9 with PAZ, Starlink demo and new fairing. NASASpaceflight. https://www.nasaspaceflight.com/2018/02/spacex-falcon-9-paz-launch-starlink-demo-new-fairing/. Accessed 19 September 2022

Guan M, Xu T, Gao F, Nie W, Yang H (2020) Optimal Walker Constellation Design of LEO-Based Global Navigation and Augmentation System. Remote Sensing, 12*(*11). https://doi.org/10.3390/rs12111845

Guo J-C (2009) Convergence of Internet and Space Technology. In: Space Technologies for the Benefit of Human Society and Earth, pp. 201-231. https://doi.org/10.1007/978-1-4020-9573-3_9

Guo L, Wang F, Gong X, Sang J, Liu W, Zhang W (2020) Initial results of distributed autonomous orbit determination for Beidou BDS-3 satellites based on inter-satellite link measurements. GPS Solutions, 24*(*3). https://doi.org/10.1007/s10291-020-00985-0

Guo X, Geng J, Chen X, Zhao Q (2019) Enhanced orbit determination for formation-flying satellites through integrated single- and double-difference GPS ambiguity resolution. GPS Solutions, 24*(*1). https://doi.org/10.1007/s10291-019-0932-1

Guo X, Zhang Y, Zhou H, Zhao Y, Zhao Q (2022) Enhanced orbit determination for formation-flying satellites based on M-estimation. Advances in Space Research. https://doi.org/10.1016/j.asr.2022.05.043

Gvozdjak P (2000) Modeling communications in Low-Earth-Orbit satellite networks. Dissertation, Simon Fraser University

Hackel S, Montenbruck O, Steigenberger P, Balss U, Gisinger C, Eineder M (2016) Model improvements and validation of TerraSAR-X precise orbit determination. Journal of Geodesy, 91*(*5): 547-562. https://doi.org/10.1007/s00190-016-0982-x

Hairer E, Wanner G, Nørsett SP (1993) Solving Ordinary Differential Equations I. Springer, Berlin, Heidelberg. ISBN: 978-3-540-56670-0

He X, Hugentobler U (2018) Design of Mega-Constellations of LEO Satellites for Positioning. In: China Satellite Navigation Conference (CSNC) 2018 Proceedings, pp. 663-673. https://doi.org/10.1007/978-981-13-0005-9_54

He X, Hugentobler U, Schlicht A, Nie Y, Duan B (2022) Precise orbit determination for a large LEO constellation with inter-satellite links and the measurements from different ground networks: a simulation study. Satellite Navigation, 3*(*1). https://doi.org/10.1186/s43020-022-00083-1

Hegarty CJ, Chatre E (2008) Evolution of the Global Navigation SatelliteSystem (GNSS). Proceedings of the IEEE, 96*(*12): 1902-1917. https://doi.org/10.1109/jproc.2008.2006090

Henry C (2018) Kepler Communications opens launch bids for Gen-1 LEO constellation. SpaceNews. https://spacenews.com/kepler-communications-opens-launch-bids-for-gen-1-leo-constellation/. Accessed 19 September 2022

Herring T (1992) Modeling Atmospheric Delays in the Analysis of Space Geodetic Data. In: De Munck JC, Spoelstra TA (eds), Proceedirws of Refraction of Transatmospheric simals in Geodesy (36). Geodetic Commission Publications on Geodesy, Netherlands, pp. 157-164

Hoskins AB, Medal HR, Rashidi E (2017) Satellite constellation design for forest fire monitoring via a stochastic programing approach. Naval Research Logistics (NRL), 64(8): 642-661. https://doi.org/10.1002/nav.21781

Howell E (2020) China launches final Beidou satellite to complete GPS-like navigation system. Space.com. https://www.space.com/china-launches-final-beidou-navigation-satellite.html. Accessed 19 September 2022

IADC (2007) IADC Space Debris Mitigation Guidelines. Inter-Agency Space Debris Coordination Committee (IADC). Document ID: IADC-02-01

IERS (2010) IERS Conventions (2010). Verlag des Bundesamts für Kartographie und Geodäsie, Frankfurt am Main. ISBN: 3-89888-989-6

Iridium (2019) Iridium NEXT: In Review. Iridium. https://www.iridium.com/blog/iridium-next-review/. Accessed 19 September 2022

Jackson J (1924) Note on the Numerical Integration of d2x/dt2 = f(x, t). Monthly Notes of Royal Astronomy Society, 84: 602-606

Jäggi A (2007) Pseudo-stochastic orbit modelling of Low Earth Satellites using the Global Positioning System. Schweizerische Geodätische Kommission / Swiss Geodetic Commission. ISBN: 9783908440178

Jäggi A, Hugentobler U, Bock H, Beutler G (2007) Precise orbit determination for GRACE using undifferenced or doubly differenced GPS data. Advances in Space Research, 39(10): 1612-1619. https://doi.org/10.1016/j.asr.2007.03.012

Jean Y, Meyer U, Jäggi A (2018) Combination of GRACE monthly gravity field solutions from different processing strategies. Journal of Geodesy, 92(11): 1313-1328. https://doi.org/10.1007/s00190-018-1123-5

Kalman RE (1960) A New Approach to Linear Filtering and Prediction Theory. J. Basic Eng., 82: 33-45

Kang Z, Nagel P, Pastor R (2003) Precise orbit determination for GRACE. Advances in Space Research, 31(8): 1875-1881. https://doi.org/10.1016/s0273-1177(03)00159-5

Kang Z, Tapley B, Bettadpur S, Ries J, Nagel P, Pastor R (2006) Precise orbit determination for the GRACE mission using only GPS data. Journal of Geodesy, 80(6): 322-331. https://doi.org/10.1007/s00190-006-0073-5

Kang Z, Bettadpur S, Nagel P, Save H, Poole S, Pie N (2020) GRACE-FO precise orbit determination and gravity recovery. Journal of Geodesy, 94(9). https://doi.org/10.1007/s00190-020-01414-3

Kassas ZM (2020) Navigation from Low-Earth Orbit. In: Position, Navigation, and Timing Technologies in the 21st Century, pp. 1381-1412. https://doi.org/10.1002/9781119458555.ch43b

Kepler (2020) Application for Market Access Authority for a Non-Geostationary Satellite Orbit System in Ka- and Ku-band Frequencies. Federal Communications Commission (FCC). Document ID: SAT-LOA-20200526-00059

Kepler (2021) Kepler Announces Aether Contract Secured with ESA. Kepler. https://kepler.space/2021/10/18/kepler-announces-aether-contract-secured-with-esa/. Accessed 19

September 2022

Kimura K, Inagaki K, Karasawa Y (1995) Satellite constellation of low-earth-orbit (LEO) satellite global communication network using optical intersatellite links. Free-Space Laser Communication Technologies VII. https://doi.org/10.1117/12.207426

Klees R, Tenzer R, Prutkin I, Wittwer T (2008) A data-driven approach to local gravity field modelling using spherical radial basis functions. Journal of Geodesy, 82(8): 457-471. https://doi.org/10.1007/s00190-007-0196-3

Knocke P, Ries J, Tapley B (1988) Earth radiation pressure effects on satellites. Astrodynamics Conference. https://doi.org/10.2514/6.1988-4292

Koch KR, Kusche J (2002) Regularization of geopotential determination from satellite data by variance components. Journal of Geodesy, 76(5): 259-268. https://doi.org/10.1007/s00190-002-0245-x

Krebs GD (2023a) Globalstar M073 - 103 (Globalstar-2). Gunter's Space Page. https://space.skyrocket.de/doc_sdat/globalstar-2.htm. Accessed 3 April 2023

Krebs GD (2023b) Iridium-NEXT. Gunter's Space Page. https://space.skyrocket.de/doc_sdat/iridium-next.htm. Accessed 3 April 2023

Krebs GD (2023c) Kepler 4, ..., 19. Gunter's Space Page. https://space.skyrocket.de/doc_sdat/kepler-4.htm. Accessed 3 April 2023

Kur T, Liwosz T, Kalarus M (2020a) The application of inter-satellite links connectivity schemes in various satellite navigation systems for orbit and clock corrections determination: simulation study. Acta Geodaetica et Geophysica, 56(1): 1-28. https://doi.org/10.1007/s40328-020-00322-4

Kur T, Liwosz T, Kalarus M (2020b) Study on the Variance Component Estimation in relative weighting of the Inter-Satellite Links and GNSS observations for orbit determination. EGU General Assembly 2020, Online. https://doi.org/10.5194/egusphere-egu2020-7229

Kur T, Kalarus M (2021) Simulation of Inter-Satellite Link schemes for use in precise orbit determination and clock estimation. Advances in Space Research. https://doi.org/10.1016/j.asr.2021.05.011

Kur T, Liwosz T (2022) Simulation of the Use of Variance Component Estimation in Relative Weighting of Inter-Satellite Links and GNSS Measurements. Remote Sensing, 14(24). https://doi.org/10.3390/rs14246387

Lang T (1996) Low Earth orbit satellite constellations for continuous coverage of the mid-latitudes. Astrodynamics Conference. https://doi.org/10.2514/6.1996-3638

Lang TJ, Adams WS (1998) A Comparison of Satellite Constellations for Continuous Global Coverage. In: Mission Design & Implementation of Satellite Constellations, pp. 51-62. https://doi.org/10.1007/978-94-011-5088-0_5

Li B (2016) Stochastic modeling of triple-frequency BeiDou signals: estimation, assessment and impact analysis. Journal of Geodesy, 90(7): 593-610. https://doi.org/10.1007/s00190-016-0896-7

Li B, Ge H, Ge M, Nie L, Shen Y, Schuh H (2019a) LEO enhanced Global Navigation Satellite System (LeGNSS) for real-time precise positioning services. Advances in Space Research, 63(1): 73-93. https://doi.org/10.1016/j.asr.2018.08.017

Li M, Li W, Shi C, Jiang K, Guo X, Dai X, Meng X, Yang Z, Yang G, Liao M (2017) Precise orbit determination of the Fengyun-3C satellite using onboard GPS and BDS observations. Journal of Geodesy, 91(11): 1313-1327. https://doi.org/10.1007/s00190-017-1027-9

Li M, Xu T, Ge H, Guan M, Yang H, Fang Z, Gao F (2021a) LEO-Constellation-Augmented BDS Precise Orbit Determination Considering Spaceborne Observational Errors. Remote Sensing, 13(16). https://doi.org/10.3390/rs13163189

Li M, Xu T, Guan M, Gao F, Jiang N (2021b) LEO-constellation-augmented multi-GNSS real-time PPP for rapid re-convergence in harsh environments. GPS Solutions, 26(1). https://doi.org/10.1007/s10291-021-01217-9

Li X, Ma F, Li X, Lv H, Bian L, Jiang Z, Zhang X (2018) LEO constellation-augmented multi-GNSS for rapid PPP convergence. Journal of Geodesy, 93(5): 749-764. https://doi.org/10.1007/s00190-018-1195-2

Li X, Jiang Z, Ma F, Lv H, Yuan Y, Li X (2019b) LEO Precise Orbit Determination with Inter-Satellite Links. Remote Sensing, 11(18). https://doi.org/10.3390/rs11182117

Li X, Zhang W, Zhang K, Zhang Q, Li X, Jiang Z, Ren X, Yuan Y (2021c) GPS satellite differential code bias estimation with current eleven low earth orbit satellites. Journal of Geodesy, 95(7). https://doi.org/10.1007/s00190-021-01536-2

Li X, Qin Y, Zhang K, Wu J, Zhang W, Zhang Q, Zhang H (2022a) Precise orbit determination for LEO satellites: single-receiver ambiguity resolution using GREAT products. Geo-spatial Information Science: 1-11. https://doi.org/10.1080/10095020.2021.2022966

Li X, Wu J, Li X, Liu G, Zhang Q, Zhang K, Zhang W (2022b) Calibrating GNSS phase biases with onboard observations of low earth orbit satellites. Journal of Geodesy, 96(2). https://doi.org/10.1007/s00190-022-01600-5

Liu S, Li P, Cui G, Wang W (2017) Design of satellite constellation with inter-satellite links for global communication using genetic algorithm. 2017 20th International Symposium on Wireless Personal Multimedia Communications (WPMC), pp. 367-373. https://doi.org/10.1109/wpmc.2017.8301840

Long F (2014) Satellite Network Constellation Design. In: Satellite Network Robust QoS-aware Routing, pp. 21-40. https://doi.org/10.1007/978-3-642-54353-1_2

Luders RD (1961) Satellite Networks for Continuous Zonal Coverage. ARS Journal, 31(2): 179-184. https://doi.org/10.2514/8.5422

Lueders R, Ginsberg L (1974) Continuous zonal coverage - A generalized analysis. Mechanics and Control of Flight Conference. https://doi.org/10.2514/6.1974-842

Ma F, Zhang X, Li X, Cheng J, Guo F, Hu J, Pan L (2020) Hybrid constellation design using a genetic algorithm for a LEO-based navigation augmentation system. GPS Solutions, 24(2). https://doi.org/10.1007/s10291-020-00977-0

Mao X, Visser PNAM, van den Ijssel J (2019) Absolute and relative orbit determination for the CHAMP/GRACE constellation. Advances in Space Research, 63(12): 3816-3834. https://doi.org/10.1016/j.asr.2019.02.030

Mao X, Arnold D, Girardin V, Villiger A, Jäggi A (2021) Dynamic GPS-based LEO orbit determination with 1 cm precision using the Bernese GNSS Software. Advances in Space Research, 67(2): 788-805. https://doi.org/10.1016/j.asr.2020.10.012

Marz S, Schlicht A, Hugentobler U (2021) Galileo precise orbit determination with optical two-way links (OTWL): a continuous wave laser ranging and time transfer concept. Journal of Geodesy, 95(7). https://doi.org/10.1007/s00190-021-01534-4

Massatt P, Zeitzew M (1998) The GPS Constellation Design - Current and Projected. In: Proceedings of the 1998 National Technical Meeting of The Institute of Navigation. Long Beach, CA, pp. 435-445

Mathewson S (2020) SpaceX opens Starlink satellite internet to public beta testers: report. Space.com. https://www.space.com/spacex-invites-starlink-internet-beta-testing. Accessed 19 September 2022

McDowell JC (2023a) OneWeb Statistics. Jonathan's Space Pages. https://planet4589.org/space/con/ow/stats.html. Accessed 3 April 2023

McDowell JC (2023b) Starlink Statistics. Jonathan's Space Pages. https://planet4589.org/space/con/star/stats.html. Accessed 3 April 2023

Michalak G, Glaser S, Neumayer KH, König R (2021) Precise orbit and Earth parameter determination supported by LEO satellites, inter-satellite links and synchronized clocks of a future GNSS. Advances in Space Research. https://doi.org/10.1016/j.asr.2021.03.008

Montenbruck O, Gill E (2000) Satellite Orbits. Springer, Berlin, Heidelberg. ISBN: 978-3-540-67280-7

Montenbruck O, Hackel S, Jäggi A (2017) Precise orbit determination of the Sentinel-3A altimetry satellite using ambiguity-fixed GPS carrier phase observations. Journal of Geodesy, 92*(*7): 711-726. https://doi.org/10.1007/s00190-017-1090-2

Montenbruck O, Hackel S, van den Ijssel J, Arnold D (2018) Reduced dynamic and kinematic precise orbit determination for the Swarm mission from 4 years of GPS tracking. GPS Solutions, 22*(*3). https://doi.org/10.1007/s10291-018-0746-6

Mortari D, Wilkins MP, Bruccoleri C (2004) The Flower Constellations. The Journal of the Astronautical Sciences, 52*(*1-2): 107-127. https://doi.org/10.1007/bf03546424

Mozo-García Á, Herráiz-Monseco E, Martín-Peiró AB, Romay-Merino MM (2001) Galileo Constellation Design. GPS Solutions, 4*(*4): 9-15. https://doi.org/10.1007/pl00012870

Nag S, Rios JL, Gerhardt D, Pham C (2016) CubeSat constellation design for air traffic monitoring. Acta Astronautica, 128: 180-193. https://doi.org/10.1016/j.actaastro.2016.07.010

NASA (2022a) About - Facts | Hubble FAQs. National Aeronautics and Space Administration (NASA). https://www.nasa.gov/content/about-facts-hubble-faqs. Accessed 19 September 2022

NASA (2022b) Trajectory: GRACE 1 2002-012A. National Aeronautics and Space Administration (NASA). https://nssdc.gsfc.nasa.gov/nmc/spacecraft/displayTrajectory.action?id=2002-012A. Accessed 19 September 2022

NASA (2022c) Trajectory: Sputnik-1 1957-001B. National Aeronautics and Space Administration (NASA). https://nssdc.gsfc.nasa.gov/nmc/spacecraft/displayTrajectory.action?id=1957-001B. Accessed 16 September 2022

Navipedia (2014) BeiDou Space Segment. European Space Agency (ESA). https://gssc.esa.int/navipedia/index.php/BeiDou_Space_Segment. Accessed 19 September 2022

Navipedia (2018) GLONASS General Introduction. European Space Agency (ESA). https://gssc.esa.int/navipedia/index.php/GLONASS_General_Introduction. Accessed 19 September 2022

Navipedia (2021) GPS General Introduction. European Space Agency (ESA). https://gssc.esa.int/navipedia/index.php/GPS_General_Introduction. Accessed 19 September 2022

Nichols T (2013) Globalstar's Second Generation Satellites in Full Service. Via Satellite. https://www.satellitetoday.com/telecom/2013/08/28/globalstars-second-generation-satellites-in-full-service/. Accessed 19 September 2022

NOAA (2005) GPS & Selective Availability Q&A. National Oceanic and Atmospheric Administration (NOAA). https://web.archive.org/web/20050921115614/http://ngs.woc.noaa.gov/FGCS/info/sans_SA/docs/GPS_SA_Event_QAs.pdf. Accessed 19 September 2022

Orekit (2021) About Orekit. CS GROUP. https://www.orekit.org/. Accessed 19 September 2022

Pellerin C (2006) United States Updates Global Positioning System Technology. U.S. Department of State. https://web.archive.org/web/20131009161500/http://iipdigital.usembassy.gov/st/english/article/20

06/02/20060203125928lcnirellep0.5061609.html. Accessed 19 September 2022

Píriz R, Martín-Peiró B, Romay-Merino M (2005) The Galileo Constellation Design: A Systematic Approach. In: Proceedings of the 18th International Technical Meeting of the Satellite Division of The Institute of Navigation (ION GNSS 2005), Long Beach, CA, pp. 1296-1306

Press L (2020) A New Chinese Broadband Satellite Constellation. CircleID. https://circleid.com/posts/20201002-a-new-chinese-broadband-satellite-constellation. Accessed 19 September 2022

Press WH, Teukolsky SA (1992) Adaptive Stepsize Runge-Kutta Integration. Computers in Physics, 6*(*2). https://doi.org/10.1063/1.4823060

Qu Z, Zhang G, Cao H, Xie J (2017) LEO Satellite Constellation for Internet of Things. IEEE Access, 5: 18391-18401. https://doi.org/10.1109/access.2017.2735988

Rajan JA (2002) Highlights of GPS II-R autonomous navigation. Proceedings of the 58th Annual Meeting of The Institute of Navigation and CIGTF 21st Guidance Test Symposium (2002), pp. 354-363

Raptis AD, Cash JR (1985) A variable step method for the numerical integration of the one-dimensional Schrödinger equation. Computer Physics Communications, 36*(*2): 113-119. https://doi.org/10.1016/0010-4655(85)90117-1

re3data.org (2021) Vienna Mapping Functions Open Access Data. VMF Data Server, Registry of Research Data Repositories. https://doi.org/10.17616/R3RD2H

Reid TGR, Neish AM, Walter T, Enge PK (2018) Broadband LEO Constellations for Navigation. Navigation, 65*(*2): 205-220. https://doi.org/10.1002/navi.234

Reid TGR, Walter T, Enge PK, Lawrence D, Cobb HS, Gutt G, O'Conner M, Whelan D (2020) Navigation from Low Earth Orbit. In: Position, Navigation, and Timing Technologies in the 21st Century, pp. 1359-1379. https://doi.org/10.1002/9781119458555.ch43a

Ren X, Yang Y, Zhu J, Xu T (2017) Orbit determination of the Next-Generation Beidou satellites with Intersatellite link measurements and a priori orbit constraints. Advances in Space Research, 60*(*10): 2155-2165. https://doi.org/10.1016/j.asr.2017.08.024

Ren X, Zhang X, Schmidt M, Zhao Z, Chen J, Zhang J, Li X (2020) Performance of GNSS Global Ionospheric Modeling Augmented by LEO Constellation. Earth and Space Science, 7*(*1). https://doi.org/10.1029/2019ea000898

Ren X, Zhang J, Chen J, Zhang X (2021) Global Ionospheric Modeling Using Multi-GNSS and Upcoming LEO Constellations: Two Methods and Comparison. IEEE Transactions on Geoscience and Remote Sensing: 1-15. https://doi.org/10.1109/tgrs.2021.3050413

ResearchAndMarkets (2022) Location-Based Services (LBS) Market Report 2022: A $96.85 Billion Market by 2027. Business Wire. https://www.businesswire.com/news/home/20220916005254/en/Location-Based-Services-LBS-Market-Report-2022-A-96.85-Billion-Market-by-2027---Global-Industry-Trends-Opportunities-and-Forecasts---ResearchAndMarkets.com. Accessed 19 September 2022

Rodriguez-Solano CJ, Hugentobler U, Steigenberger P (2012) Adjustable box-wing model for solar radiation pressure impacting GPS satellites. Advances in Space Research, 49*(*7): 1113-1128. https://doi.org/10.1016/j.asr.2012.01.016

Schlicht A, Marz S, Stetter M, Hugentobler U, Schäfer W (2020) Galileo POD using optical inter-satellite links: A simulation study. Advances in Space Research, 66*(*7): 1558-1570. https://doi.org/10.1016/j.asr.2020.06.028

Selding PBd (2016) Telesat prepares shareholder payday, outlines 117-satellite constellation. SpaceNews. https://spacenews.com/telesat-prepares-shareholder-payday-outlines-117-satellite-constellation/. Accessed 19 September 2022

SpaceX (2016) Application for Fixed Satellite Service: SpaceX Non-Geostationary Satellite System. Federal Communications Commission (FCC). Document ID: SAT-LOA-20161115-00118

SpaceX (2017) Application for Fixed Satellite Service: SpaceX V-Band Non-Geostationary Satellite System. Federal Communications Commission (FCC). Document ID: SAT-LOA-20170301-00027

SpaceX (2020) Application for Modification of Authorization for the SpaceX NGSO Satellite System. Federal Communications Commission (FCC). Document ID: SAT-MOD-20200417-00037

SpaceX (2022) Starlink is available in Malta – now serving 40 countries around the world! → http://starlink.com/map. Twitter. https://twitter.com/SpaceX/status/1568675521168347137

Tang C, Hu X, Zhou S, Liu L, Pan J, Chen L, Guo R, Zhu L, Hu G, Li X, He F, Chang Z (2018) Initial results of centralized autonomous orbit determination of the new-generation BDS satellites with inter-satellite link measurements. Journal of Geodesy, 92*(*10): 1155-1169. https://doi.org/10.1007/s00190-018-1113-7

Tapley BD, Schutz BES, Born GH (2004) Statistical Orbit Determination. ISBN: 9780126836301

Telesat (2020) Application for Modification of Market Access Authorization. Federal Communications Commission (FCC). Document ID: SAT-MPL-20200526-00053

Tiberius C, Kenselaar F (2003) Variance Component Estimation and Precise GPS Positioning: Case Study. Journal of Surveying Engineering, 129*(*1): 11-18. https://doi.org/10.1061/(asce)0733-9453(2003)129:1(11)

Ullock MH, Schoen AH (1963) Optimum Polar Satellite Networks for Continuous Earth Coverage. AIAA Journal, 1*(*1): 69-72. https://doi.org/10.2514/3.1471

Urlichich Y, Subbotin V, Stupak G, Dvorkin V, Povalyaev A, Karutin S (2011) GLONASS modernization. Proceedings of the 24th International Technical Meeting of the Satellite Division of The Institute of Navigation (ION GNSS 2011), pp. 3125-3128

USNO (2011) USNO NAVSTAR Global Positioning System. U.S. Naval Observatory (USNO). https://web.archive.org/web/20110126200746/http://tycho.usno.navy.mil/gpsinfo.html. Accessed 19 September 2022

van den Ijssel J, Encarnação J, Doornbos E, Visser P (2015) Precise science orbits for the Swarm satellite constellation. Advances in Space Research, 56*(*6): 1042-1055. https://doi.org/10.1016/j.asr.2015.06.002

Vetter JR (2007) Fifty Years of Orbit Determination: Development of Modern Astrodynamics Methods. Johns Hopkins APL Technical Digest, 27*(*3): 239-252

Walker JG (1970) Circular Orbit Patterns Providing Continuous Whole Earth Coverage. Royal Aircraft Establishment. Document ID: 70211

Walker JG (1977) Continuous Whole-Earth Coverage by Circular-Orbit Satellite Patterns. Royal Aircraft Establishment. Document ID: 77044

Walker JG (1982) Coverage Predictions and Selection Criteria for Satellite Constellations. Royal Aircraft Establishment. Document ID: 82116

Wang K, Liu J, Su H, El-Mowafy A, Yang X (2022a) Real-Time LEO Satellite Orbits Based on Batch Least-Squares Orbit Determination with Short-Term Orbit Prediction. Remote Sensing, 15*(*1). https://doi.org/10.3390/rs15010133

Wang K, Yang X, El-Mowafy A (2022b) Visibility of LEO Satellites under Different Ground Network

Distributions. Proceedings of the 35th International Technical Meeting of the Satellite Division of The Institute of Navigation (ION GNSS+ 2022), pp. 2478-2491. https://doi.org/10.33012/2022.18391

Weinbach U (2013) Feasibility and impact of receiver clock modeling in precise GPS data analysis. Verlag der Bayerischen Akademie der Wissenschaften. ISBN: 978-3-7696-5104-1

Werner M, Jahn A, Lutz E, Bottcher A (1995) Analysis of system parameters for LEO/ICO-satellite communication networks. IEEE Journal on Selected Areas in Communications, 13(2): 371-381. https://doi.org/10.1109/49.345881

Winkler R (2015) Greg Wyler's OneWeb Satellite-Internet Company Secures Funding. The Wall Street Journal. https://www.wsj.com/articles/greg-wylers-oneweb-satellite-internet-company-secures-funding-1421278832. Accessed 19 September 2022

Wu SC, Yunck TP, Thornton CL (1991) Reduced-dynamic technique for precise orbit determination of low earth satellites. Journal of Guidance, Control, and Dynamics, 14(1): 24-30. https://doi.org/10.2514/3.20600

Wu T, Hu J, Wu S (2006) Convergent-reconstruction-based Inter-Layer Inter-Satellite Links Establishment Strategies for Two-tier LEO/MEO Satellite Networks. 2006 International Workshop on Satellite and Space Communications, pp. 259-263. https://doi.org/10.1109/iwssc.2006.256038

Wu T, Wu S (2008) Research on the design of orthogonal circular orbit satellite constellation. Syst Eng Electron, 30(10): 1966-1972

Xie X, Geng T, Zhao Q, Lv Y, Cai H, Liu J (2020) Orbit and clock analysis of BDS-3 satellites using inter-satellite link observations. Journal of Geodesy, 94(7). https://doi.org/10.1007/s00190-020-01394-4

Xiong S, Ma F, Ren X, Chen J, Zhang X (2021) LEO Constellation-Augmented Multi-GNSS for 3D Water Vapor Tomography. Remote Sensing, 13(16). https://doi.org/10.3390/rs13163056

Yang D, Yang J, Li G, Zhou Y, Tang C (2017) Globalization highlight: orbit determination using BeiDou inter-satellite ranging measurements. GPS Solutions, 21(3): 1395-1404. https://doi.org/10.1007/s10291-017-0626-5

Yang JC, de Groh KK (2010) Materials Issues in the Space Environment. MRS Bulletin(35): 12-19. https://doi.org/10.1017/S0883769400100004

Yang M, Dong X, Hu M (2016) Design and simulation for hybrid LEO communication and navigation constellation. 2016 IEEE Chinese Guidance, Navigation and Control Conference (CGNCC), pp. 1665-1669. https://doi.org/10.1109/cgncc.2016.7829041

Yang Y-x, Xu T-h, Song L-j (2005) Robust Estimation of Variance Components with Application in Global Positioning System Network Adjustment. Journal of Surveying Engineering, 131(4): 107-112. https://doi.org/10.1061/(asce)0733-9453(2005)131:4(107)

Yang Y, Gao W, Guo S, Mao Y, Yang Y (2019) Introduction to BeiDou-3 navigation satellite system. Navigation, 66(1): 7-18. https://doi.org/10.1002/navi.291

Yang Y, Yang Y, Guo R, Tang C, Zhang Z (2020) The Influence of Station Distribution on the BeiDou-3 Inter-satellite Link Enhanced Orbit Determination. In: China Satellite Navigation Conference (CSNC) 2020 Proceedings: Volume II, pp. 58-70. https://doi.org/10.1007/978-981-15-3711-0_6

Yuan L, Hoque M, Jin S (2021) A new method to estimate GPS satellite and receiver differential code biases using a network of LEO satellites. GPS Solutions, 25(2). https://doi.org/10.1007/s10291-021-01109-y

Yunck TP, Wu SC, Wu JT, Thornton CL (1990) Precise tracking of remote sensing satellites with the

Global Positioning System. IEEE Transactions on Geoscience and Remote Sensing, 28(1): 108-116. https://doi.org/10.1109/36.45753

Zardashti R, Emami S (2021) Spatial Geometry Design of a Low Earth Orbit Constellation for Iranian Regional Navigation Satellite System. Journal of Aerospace Technology and Management, 13. https://doi.org/10.1590/jatm.v13.1215

Zhang P, Ding W, Qu X, Yuan Y (2023) Simulation Analysis of LEO Constellation Augmented GNSS (LeGNSS) Zenith Troposphere Delay and Gradients Estimation. IEEE Transactions on Geoscience and Remote Sensing. https://doi.org/10.1109/tgrs.2023.3241956

Zhang R, Zhang Q, Huang G, Wang L, Qu W (2015) Impact of tracking station distribution structure on BeiDou satellite orbit determination. Advances in Space Research, 56(10): 2177-2187. https://doi.org/10.1016/j.asr.2015.07.045

Zhang R, Tu R, Zhang P, Fan L, Han J, Lu X (2021) Orbit determination of BDS-3 satellite based on regional ground tracking station and inter-satellite link observations. Advances in Space Research, 67(12): 4011-4024. https://doi.org/10.1016/j.asr.2021.02.027

Zhang T-J, Shen H-X, Li Z, Qie H, Cao J, Li H-N, Yang Y-K (2018) Restricted constellation design for regional navigation augmentation. Acta Astronautica, 150: 231-239. https://doi.org/10.1016/j.actaastro.2018.04.044

Zhang Y, Li Z, Li R, Wang Z, Yuan H, Song J (2020) Orbital design of LEO navigation constellations and assessment of their augmentation to BDS. Advances in Space Research, 66(8): 1911-1923. https://doi.org/10.1016/j.asr.2020.07.021